NOVEL INTRAVASCULAR ULTRASOUND TRANSDUCERS

SU MIN

PhD

The Hong Kong Polytechnic University

2024

The Hong Kong Polytechnic University

Department of Biomedical Engineering

Novel Intravascular Ultrasound Transducers

SU Min

A thesis submitted in partial fulfillment of the requirements for the degree of Doctor of Philosophy

August 2023

CERTIFICATE OF ORIGINALITY

I hereby declare that this thesis is my own work and that, to the best of my knowledge and belief, it reproduces no material previously published or written, nor material that has been accepted for the award of any other degree or diploma, except where due acknowledgement has been made in the text.

_____(Signed)

SU Min_____(Name of student)

ABSTRACT

Cardiovascular disease (CVD) is accountable for majority of the global mortality and is primarily attributable to atherosclerotic plaques (APs). Intravascular ultrasound (IVUS) is currently among the most crucial imaging technologies for AP diagnosis. However, poor spatial resolution is the main drawback of conventional IVUS. To address this limitation, we proposed two novel ultrasound transducers were developed to enhance the lateral resolution of IVUS imaging. In one study, a Fresnel zone plate (FZP) layer was prepared and introduced on the IVUS transducer surface. This FZP layer enhances the transducer's focusing effect, thereby improving the lateral imaging resolution. The structure of the transducer is designed based on theoretical calculations. The acoustic beam and other important parameters of the transducer are optimized using COMSOL software. The transducer has an ultrasonic element (dimension: 0.778×0.9 mm^2). FZP and planar IVUS transducers were fabricated and compared in the study. The FZP transducer demonstrates a center frequency (Fc) of 52.5 MHz and a −6 dB relative bandwidth (BW) of 42%. The planar transducer, on the other hand, has a center frequency of 51.3 MHz and a −6 dB relative bandwidth of 58%. To evaluate the imaging performance of the fabricated transducers, imaging experiments with the house made wire phantom and swine artery sample were conducted. The FZP and planar transducers achieved axial imaging resolutions of 47 and 44 μm and lateral

imaging resolutions of 184 and 314 μm, respectively. The study results indicate that the inclusion of the FZP layer enhances the lateral imaging resolution of the transducer for IVUS applications.

The other study presents a novel approach for enhancing the spatial resolution of IVUS imaging by proposing a geometrically focused IVUS transducer that uses PIN-PSN-PT piezoelectric ceramic with a larger aperture compared with conventional geometrically focused transducers. The selected PIN-PSN-PT ceramic has a favorable dielectric constant, allowing a suitable electrical impedance (50 Ω) at a larger element aperture of 0.6 × 0.6 mm. Acoustic beams and spatial resolutions were simulated using Field II program. Geometrically focused and planar transducers were manufactured accordingly. The focused and planar transducers had a center frequency of 42 and 41 MHz and a −6 dB relative bandwidth of 71% and 68%, respectively. The designed transducers were characterized by conducting imaging experiments of wire phantom and ex-vivo porcine artery. The focused transducer exhibited superior spatial resolution, with values of 45 μm axially and 208 μm laterally, to the planar transducer with resolutions of 48 μm axially and 282 μm laterally, respectively. These results indicate the potential of the focused transducer, utilizing PIN-PSN-PT ceramic, to enhance the lateral resolution in IVUS imaging applications.

Non-uniform rotational distortion (NURD) encountered in mechanically rotating

catheters hampers accurate image acquisition. We here proposed a dual-element IVUS catheter to address this concern. In the catheter, two elements with similar frequencies and other properties are assembled in a back-to-back configuration. In the presence of NURD during imaging, the abnormal image portion obtained from one element can be modified by the corresponding regular ultrasound image acquired by another element in the catheter. This allows the reconstruction of an image without NURD. In addition, the catheter can obtained two images in a single rotation, effectively doubling the imaging frame rate compared to a single-element configuration. Wire phantom imaging was performed for evaluating the imaging resolution of these two elements. Additionally, the feasibility and overall imaging performance of the proposed protocol were verified using a tissue phantom and by performing porcine artery vascular imaging. The results indicate that the novel strategy has substantial potential for application in clinical settings.

Keywords: Intravascular ultrasound, Fresnel zone plate, Imaging resolution, Nonuniform rotational distortion, Dual-element catheter

LIST OF PUBLICATIONS

Journal articles:

1. **M. Su**[#], X. Xia[#], B. Liu[#], Z. Zhang, R. Liu, F. Cai, W. Qiu, and L. Sun, "High frequency focal transducer with a Fresnel zone plate for intravascular ultrasound," *Applied Physics Letters,* vol. 119, no. 14, pp. 143702, 2021.

2. B. Liu, **M. Su**, Z. Zhang, R. Liu, L. Sun, H. Zheng, and W. Qiu, "A Novel Dual-Element Catheter for Improving Non-Uniform Rotational Distortion in Intravascular Ultrasound," *IEEE Transactions on Biomedical Engineering*, vol. 70, no. 6, pp. 1768-1774, 2023.

3. B. Liu[#], **M. Su**[#], Z. Zhang, L. Sun, and W. Qiu, "A Novel Coded Excitation Imaging Platform for Ultra-High Frequency (>100MHz) Ultrasound," *IEEE Transactions on Ultrasonics, Ferroelectrics, and Frequency Control,* submitted.

4. C. Qiu[#], **M. Su**[#], S. Yang, B. Liu, N. Jia, Z. Xu, H. Zheng, L. Sun, F. Li, and W. Qiu, "Textured-Piezoelectric-Ceramic-Based Focused Intravascular Ultrasonic Transducer with Both High Spatial Resolution and Wide Imaging Depth Range," *IEEE Transactions on Medical Imaging,* submitted.

5. Q. Xian, Z. Qiu, S. Murugappan, S. Kala, K. F. Wong, D. Li, G. Li, Y. Jiang, Y. Wu,

M. Su, X. Hou, J. Zhu, J. Guo, W. Qiu, and L. Sun, "Modulation of deep neural circuits with sonogenetics," *Proceedings of the National Academy of Sciences*, vol. 120, no. 22, pp. e2220575120, 2023.

Conference Proceedings:

1. **M. Su**, C. Qiu, B. Liu, F. Li, H. Zheng, W. Qiu and L. SUN, "A Focused High Sensitivity Transducer for Intravascular Ultrasound Application," *2023 IEEE International Ultrasonics Symposium*, Montreal, Canada, September, 2023, accepted.

2. **M. Su**, F. Li, Z. Zhang, H. Zheng, W. Qiu and L. SUN, "Lens-Shared Dual Frequency Linear Array for Intracranial Pressure Estimation," *2023 IEEE International Ultrasonics Symposium*, Montreal, Canada, September, 2023, accepted.

ACKNOWLEDGEMENTS

The people who have provided assistance during my PhD studies are the ones I want to be grateful for. Their unwavering support, guidance, and encouragement have been invaluable throughout this transformative journey.

First and foremost, I would like to extend my heartfelt thanks to my supervisor, Professor Lei Sun, for his kindness, enlightening guidance, and profound knowledge. His patient mentorship in scientific research, coupled with his genuine care and concern for me, has made an indelible impact on my life. His rigorous scientific approach has cultivated my research attitude, and his insightful analysis often inspires me deeply. He has also imparted his wealth of life experience, offering me invaluable wisdom. In addition, I would like to thank Dr. Puxiang Lai and Dr. Kwok Ho Lam for generously allowing me to share their office and research lab.

Furthermore, I am deeply grateful to Dr. Weibao Qiu from the Shenzhen Institute of Advanced Technology. His perceptive feedback, constructive criticism, and constant motivation have propelled me towards achieving excellence in transducer technology. He has provided me with essential equipment, materials, and other resources for my transducer research. His selfless assistance and guidance have significantly enhanced my scientific research capabilities.

I consider myself incredibly fortunate to have the unwavering support and understanding of my beloved wife, Ms. Jing Guo. Throughout my PhD journey, she has been my steadfast companion, studying alongside me and progressing together. Her patience, love, and unwavering encouragement have served as the bedrock of my strength during the challenges of academia. I also want to thank my little son, Jiner Su, whose adorable nature and infectious smile bring me unparalleled comfort. To me, he is like a beacon of light in the darkest of nights.

I would like to thank Prof. Yongping Zheng, Prof. Ming Zhang, Prof. Mo Yang, Dr. Xiaoling Hu, Dr. Puxiang Lai, Dr. Chunyi Wen, Dr. Sharon Ruan, and Dr. Duo Wong for their invaluable assessments of my proposal, coursework, confirmation report and dissertation. Their valuable comments and identification of areas for encouragement in my work and presentations have been instrumental in improving my research.

Furthermore, I want to extend my sincere appreciation to the teachers and staff at SIAT, including Prof. Hairong Zheng, Dr. Fei Li, Dr. Zhiqiang Zhang, Dr. Feiyan Cai, and Mr. Yongchuan Li. Their assistance, cooperation, and provision of resources have been indispensable in facilitating my research endeavors.

I want to thank my classmates and colleagues for their unwavering support and camaraderie, particularly Mr. Baoqiang Liu, Mr. Chaorui Qiu, Mr. Xiangxiang Xia, Mr.

Weichang Wu, Mr. Yiliang Chen, Mr. Xuandi Hou, Ms. Quanxiang Xian, Ms. Ting Lei, Mr. Yizhou Jiang, Ms. Xiaohui Huang, and Mr. Yu Qiang. Their insightful discussions, constructive feedback, and collaborative spirit have fostered an intellectually stimulating academic environment, thereby enriching the quality of my work. I'm grateful for the enriching experiences and fruitful collaborations we have shared.

TABLE OF CONTENTS

LIST OF ABBREVIATIONS

2D	Two-dimensional
3D	Three-dimensional
ACS	Acute coronary syndrome
ADC	Analogue-to-digital converter
ADE	Automated differential echogenicity
AP	Atherosclerotic plaques
AS	Atherosclerosis
BFV	Blood flow velocity
BT	BaTiO3
BW	Bandwidth
CAG	Coronary angiography
CHD	Coronary heart disease
CNR	Contrast to noise ratio
CRP	C-reactive protein
CT	Computed tomography
CVD	Cardiovascular disease
DF	Dual frequency
EBCT	Electron beam computed tomography
EPA	Eicosapentaenoic acid
Fc	Center frequency
FE-SEM	Field-emission scanning electron microscopy
FFT	Fast Fourier Transform
FWHM	Full width at half maximum
FPGA	Field programmable gate array
FZP	Fresnel zone plate
IL	Insertion loss
IMT	Intima-media thickness
LDL	Low-density lipoprotein
$LiNbO_3$	Lead-free single crystal lithium niobate
LNA	Low noise amplifier
LPF	Low-pass filter
LVDS	Low-voltage differential signaling

HFU	High-frequency ultrasound
ID	Inter diameter
ISPTP	Spatial peak time peak intensity
IVPA	Intravascular photoacoustic
IVUS	Intravascular ultrasound
KLM	Krimboltz, Leedom, and Mattaei
MRA	Magnetic resonance angiography
NIRS	Near-infrared reflectance spectroscopy
NURD	Non-uniform rotational distortion
OCT	Optical coherence tomography
OD	Out diameter
PAT	Photoacoustic tomography
PC	Personal computer
PCB	Printed circuit board
P-E	Polarization-electric
PIN-PMN-PT	Lead indium niobate-lead magnesium niobate-lead titanate
PIN-PSN-PT	Lead indium niobate-lead scandium niobate-lead titanate
PR	Phase-reversal
PRF	Pulse repeat frequency
PWV	Pulse wave velocity
PZT	Lead Zirconate Titanate
RF	Radiofrequency
RLP	Remnant-like particle
SNR	Signal to noise ratio
SPI	Serial Peripheral Interface
TCFA	Thin cap fibro atheroma
TRSW	The transmit/receive switch
UHF	Ultra-high frequency
VP	Vulnerable plaques
WHO	World Health Organization
XRD	X-ray diffraction

LIST OF FIGURES

LIST OF TABLES

Chapter 1 Introduction

1.1 Background

1.1.1 Cardiovascular Disease (CVD)

CVDs, a collection of medical conditions, include coronary heart disease (CHD), hypertension, arrhythmia, and heart valve disease [1]. These disorders frequently impact the function of the heart and other organs, which often causes poor blood circulation, insufficient blood flow, and inadequate delivery of nutrients and oxygen to the blood. As stated by the World Health Organization (WHO), in 2019, CVD caused 17.9 million deaths worldwide, representing nearly 32% of global deaths[2]. CVD is responsible for the bulk of global mortality. This disease is not only considered a problem in Western countries but also the developing world[3]. According to Fig. 1.1, China's CVD death rates in both urban and rural areas are consistently presenting an increasing trend[4]. Approximately 2.4 million persons in China died from atherosclerotic CVD (including ischemic stroke and ischemic heart disease) in 2016, accounting for 61% of all coronary artery disease (CAD)-related deaths[5]. Cardiovascular disorders, including CHD, myocardial infarction, cerebral infarction, and others, are highly prevalent among middle-aged and older individuals.

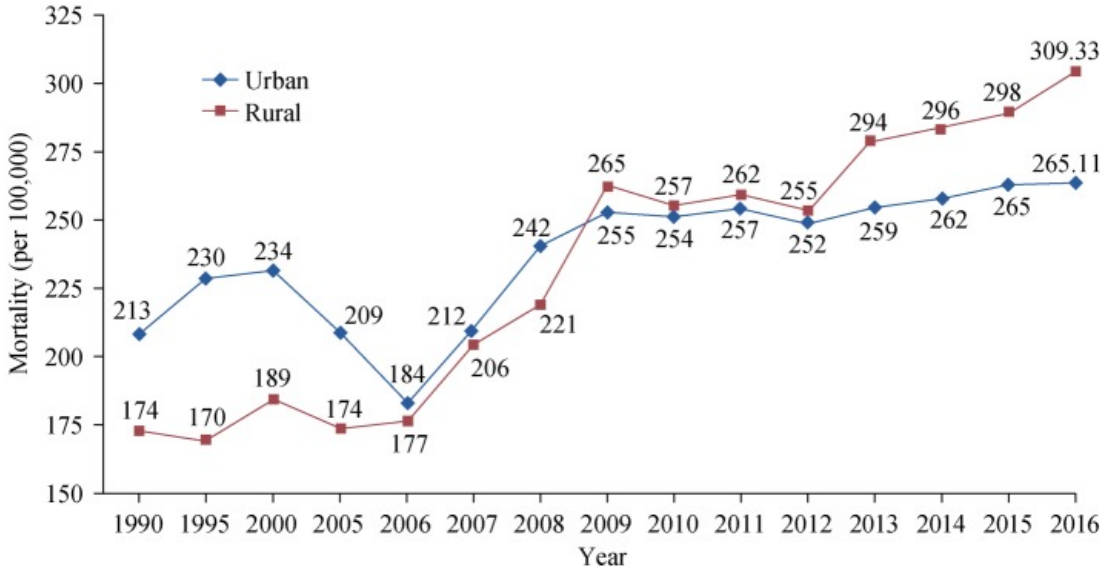

Fig. 1.1. Mortality of CVD in China from 1990 to 2016 [4].

1.1.2 Atherosclerosis (AS) and Atherosclerotic Plaque (AP)

AS is a systemic disease associated with lipid metabolism disorders. It involves the accumulation of lipids, specifically cholesterol and fatty substances, within the intima of arteries. The subepidermal lipids, particularly low-density lipoprotein (LDL), gradually deposited within blood vessels resulting in vascular wall thickening, contributing to AS development and varying degrees of plaque formation[6].

AS progression is gradual during the initial decades. However, with chronic inflammation, APs begin to accumulate in medium- and large-sized arteries[7]. With plaque buildup, the luminal area of the arteries gradually decreases, resulting in a reduction in blood flow. This reduction can further lead to myocardial hypoxia and ischemia[8]. Fig. 1.2 illustrates the process of AS development[9].

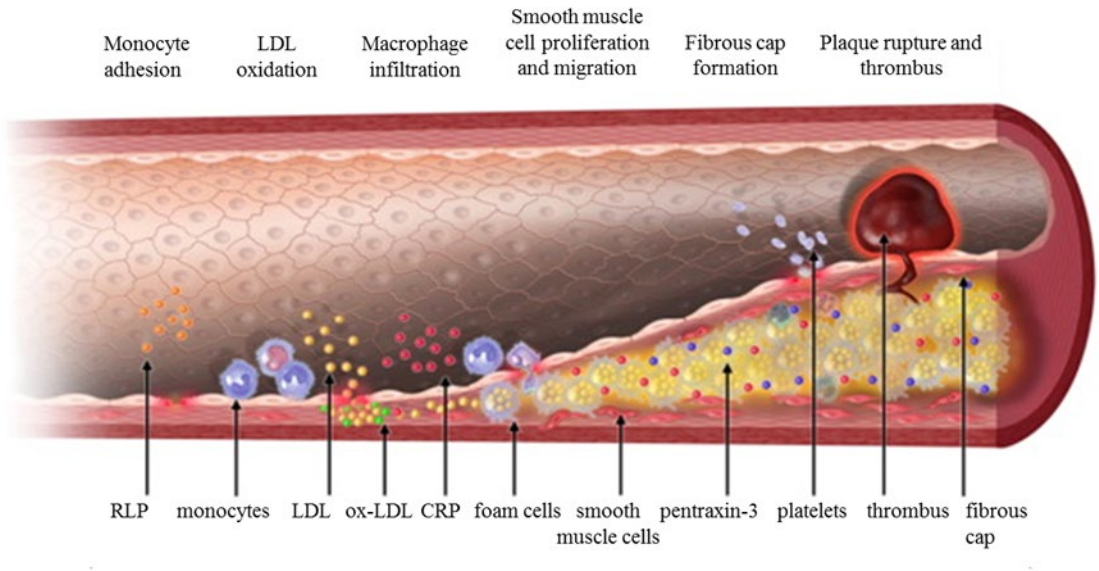

Fig. 1.2. An illustration depicting the process of AS [9].

The consequences of AP occurrence significantly vary depending on whether the plaque ruptures or remains stable. Plaque rupture is generally associated with more severe outcomes. Under circumstances, such as a sudden increase in blood pressure or intense physical exertion, vulnerable and unstable plaques can rupture abruptly, which leads to acute coronary syndromes (ACS), for example, angina and myocardial infarction[10]. According to global statistics, nearly 20 million people die annually from acute vascular events, including ACS and sudden cardiac death, with most experiencing no preceding symptoms[11]. A study reported that the rupture of vulnerable plaques (VP) is responsible for ACS in approximately 70% of patients [12].

Plaque formation in coronary arteries is common, and an individual may have multiple plaques in their coronary arteries. However, not all plaques rupture and lead to clot

formation. The vulnerability of the plaque itself determines whether the plaque is prone to rupture. To elucidate these concepts, two terms need to be explained: culprit plaques and VP[13]. "Culprit plaque" refers to the specific plaque that causes coronary artery blockage and is considered the main cause or "culprit" for acute cardiovascular events, leading to adverse outcomes. On the other hand, VP is a plaque apt for thrombus formation and can potentially develop into a culprit plaque rapidly. While the culprit plaque concept is retrospective, as it identifies the plaque causing an acute cardiovascular event after the event has occurred. By contrast, the VP concept is prospective, as it aims to predict the plaque that would likely rupture and form a thrombus before an event occurs. In other words, a VP can be viewed as a "future culprit plaque." Therefore, the clinical assessment of the VP-associated risk is crucial for the early prediction and treatment of ACS [14].

1.2 Current Vascular Imaging Technology

Medical imaging technology is a crucial player in the study of mechanisms underlying AS and VP. Various imaging technologies are currently used to visualize the components and function of the arterial lumen, APs, endothelial cells, and other relevant factors. These imaging tools are always categorized as noninvasive imaging and invasive imaging.

1.2.1 Non-Invasive Imaging Technology

Noninvasive imaging technology is primarily used for examining the carotid artery because of its relatively large diameter, proximity to the body surface, and limited movement. The noninvasive imaging techniques mainly employed in this context are computed tomography (CT), noninvasive ultrasound imaging, and magnetic resonance imaging (MRI).

1.2.1.1 Computed tomography

In CT, a single-axis X-ray rotation is used to irradiate the human body. Because the X-ray absorption characteristics of different biological tissues are different, the detector captures projection data directly linked to the tissue's attenuation coefficient. By inputting all the projection data into a computer and applying an image reconstruction algorithm, a two-dimensional (2D) topography of the detection plane can be reconstructed. The grayscale value of the image corresponds to the tissue's attenuation coefficient (Fig. 1.3). In coronary artery imaging, two CT types are commonly used: electron-beam CT (EBCT) and multi-slice CT (MSCT)[15].

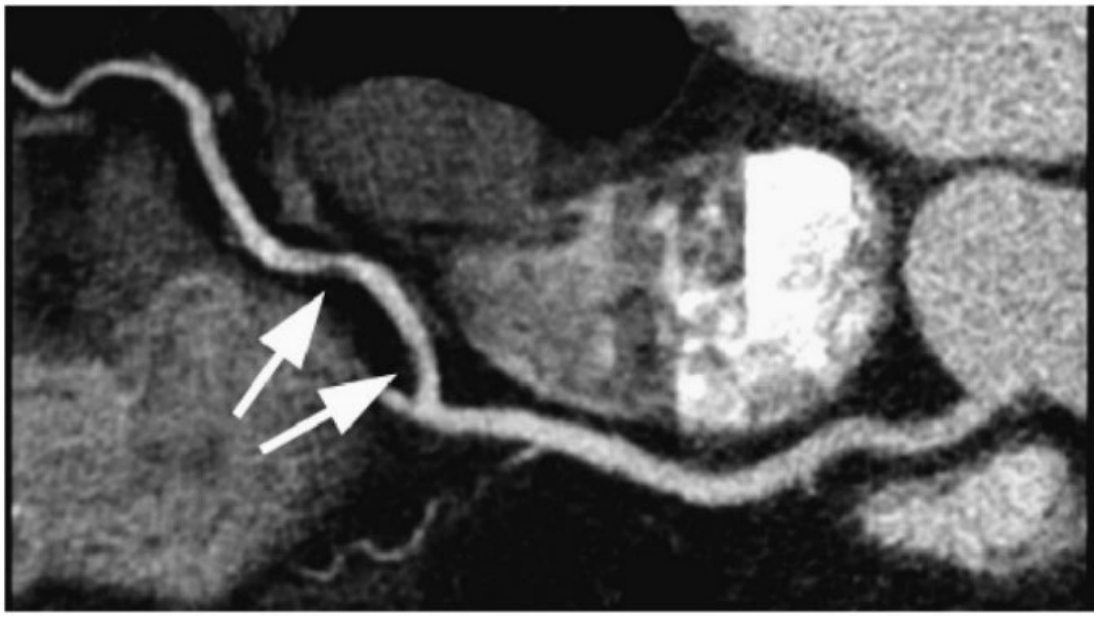

Fig. 1.3. A CT image of the coronary artery showing two plaques (white arrows) [15].

EBCT uses a deflection motion of an electron beam instead of the rotating motion of an X-ray tube, like in conventional CT, for mechanical scanning. Therefore, EBCT can achieve scanning speeds several times faster than conventional CT[16]. Because of its short scan duration and exposure time, EBCT scans can be performed during a deep inhalation hold, thereby effectively eliminating respiration-induced motion errors[17].

EBCT can display APs near the main coronary artery and its branch vessels, and the plaque density can provide an approximate indication of its type. EBCT exhibits higher sensitivity in detecting coronary artery calcified plaques than coronary angiography and intracoronary ultrasound[18]. Although EBCT excels in detecting calcified plaques for early coronary stenosis, its ability to evaluate subtle plaque tissue structures, such as fibrous cap thickness, remains limited[19]. Plaque inspection using EBCT is <80%

successful, and the high cost and single-purpose design of EBCT have restricted the number of manufacturers and hindered its widespread clinical application.

Remarkable advancements have been made in detector structure and data processing systems of MSCT, thereby resulting in improved scanning speeds that are particularly advantageous for coronary artery and cardiac imaging. MSCT can visualize the vascular lumen to detect stenosis. It can also image the vascular, allowing for the differentiation of various plaque components and facilitating the identification of vunerable plaques[20].

However, MSCT is dependent on density variations among tissues for surface reconstruction, and therefore, it cannot accurately represent the color of the vascular intima. Consequently, displaying flat APs and other superficial mucosal lesions by using MSCT may be challenging. Furthermore, MSCT may not always provide information that is completely reliable for measurements, such as lumen wall thickness, identification of plaque components such as calcified deposits, and distinction of plaque properties.

1.2.1.2 Noninvasive ultrasound imaging

Sound with frequency above 20 kHz is defined as ultrasound. Each biological tissue possesses unique acoustic impedance; hence ultrasound waves propagate at different speeds through these tissues. At the interface of tissues with distinct acoustic

impedances, a part of the ultrasound waves is reflected, whereas the remaining part continues to propagate. On reaching deeper tissue boundaries, the propagated portion is further divided into components that propagate and reflect. An ultrasound image can be generated by detecting all the reflected echoes and subjecting them to signal processing (Fig. 1.4)[21].

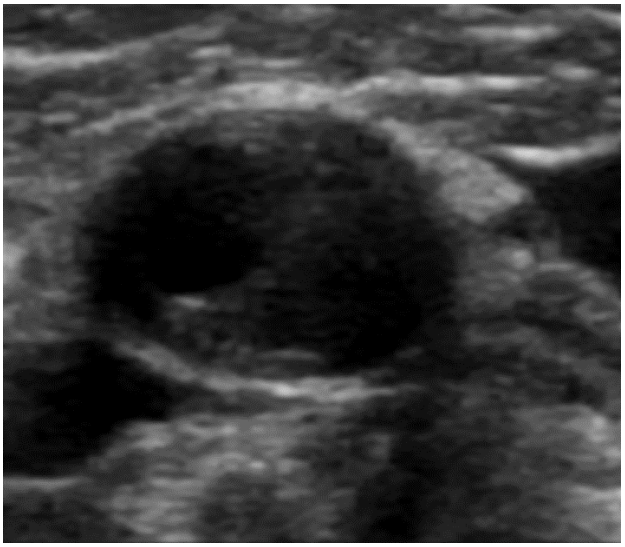

Fig. 1.4. Noninvasive ultrasound image of an AP [21].

Ultrasound imaging, particularly B-mode imaging, is extensively used in clinical practice to assess the health of the carotid arteries. The primary focus of most ultrasound clinical diagnoses is vascular stenosis evaluation. Through carotid artery ultrasonography, Mathiesen et al. observed an elevated risk of ischemic stroke associated with echolucent plaques[22]. Furthermore, ultrasound is used for measuring carotidintima–media thickness (IMT) as an early predictor of AS development[23]. Apart from B-mode ultrasound imaging, M-mode ultrasound imaging allows for vessel

elasticity assessment by measuring carotid artery pulsation[24].

New ultrasound imaging techniques have recently emerged with the study of ultrasound radiofrequency (RF) signals. Pulse wave velocity estimation, for example, contributes to the assessment of arterial wall stiffness[25]. Additionally, three-dimensional (3D) ultrasound has been proposed to acquire a comprehensive 3D topography of plaques[26]. These advancements highlight the expanding capabilities of ultrasound imaging in carotid artery assessment[27].

1.2.1.3 MRI and MRA

Using the motion of nuclear spins, MRI, a form of tomographic imaging, activates protons within a specific region of interest by applying pulsed RF energy in an external magnetic field. When protons absorb specific energy, their nuclear magnetic energy changes with distance. The detector captures MR signals from various spatial positions. A computer then processes and converts these signals to generate an image of the region of interest[28].

Magnetic resonance angiography (MRA), a novel MRI technology, takes advantage of the void phenomenon created by blood flowing within blood vessels. Flow velocity influences the MR signal intensity in blood. Fast-flowing blood typically exhibits low signal intensity, whereas slower flow results in high signal intensity. This contrast between flowing blood and adjacent tissue enables effective vascular imaging[29].

MRA is currently employed for diagnosing large and medium vascular lesions (Fig. 1.5)[30], and ongoing advancements continue to enhance the capabilities of MRA[31].

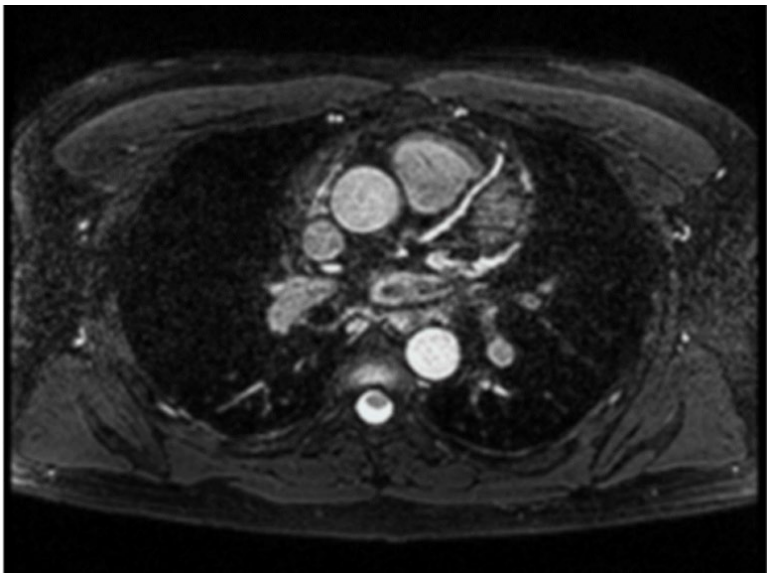

Fig. 1.5. A whole-heart coronary MRA image[30].

MRA is a noninvasive method of obtaining vascular morphology and tissue function information, which thus eliminates the need for invasive procedures or contrast agent injection. This modality allows objective imaging analysis of the anatomical morphology, wall motion, myocardial perfusion, and cardiac function of the major heart vessels. Cross-sectional, sagittal, coronal, and various oblique plane views can be obtained through MRA for comprehensive evaluation[32].

Furthermore, MRA enables the detection of blood flow velocity (BFV), observation of plaque components, and differentiation of a lipid core and fibrous cap. Specific plaque

morphologies, for example a large lumen curvature and thin fibrous cap, which are strongly associated to plaque vulnerability, can be identified using MRA[33]. Additionally, MRA molecular imaging technology can be applied to find plaque components[34]. However, these MRA capabilities are primarily applicable to lesions in the main coronary artery. MRA cannot be used for vessels with small diameters. Factors such as patient respiratory movement and breath-hold duration can impact the quality of images obtained through MRA. Moreover, the accuracy of MRA is restricted, with an imaging resolution of >0.5mm in the absence of a contrast agent[35]. This accuracy level does not meet the demands for analyzing the structural characteristics of coronary plaques.

1.2.2 Invasive Vascular Imaging Technology

Invasive vascular imaging is a technique in which a catheter is inserted into a blood vessel for imaging purposes. This invasive technique helps acquire detailed and accurate information about the lumen and plaque because of the proximity of the catheter to the target tissue. Invasive imaging methods can be classified as follows: Coronary angiography (CAG), optical coherence tomography (OCT), and IVUS.

1.2.2.1 CAG

CAG is a diagnostic technique that requires the entering of a catheter through an artery, followed by injecting the contrast agent into the arteries via the catheter while acquiring

an image of the artery by using X-ray projection technology[36]. CAG provides 2D contour images of the coronary lumen, thereby allowing plaque identification and vascular stenosis assessment by observing changes in the vessel diameter (Fig. 1.6)[37].

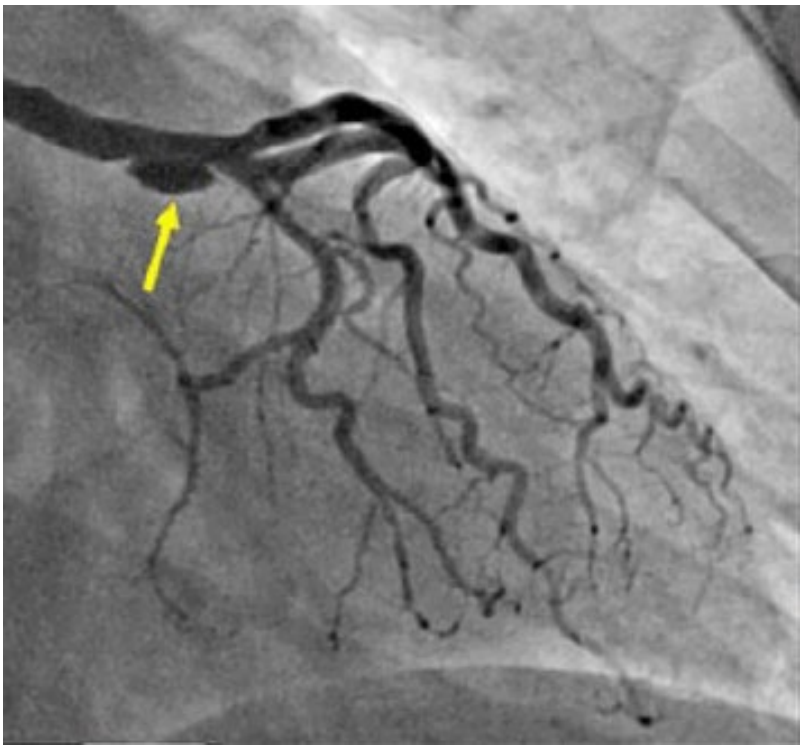

Fig. 1.6. CAG imaging of coronary angiography with spontaneous coronary artery dissection (yellow arrow)[37].

CAG is widely considered a primary diagnostic tool for CVD and has conventionally served as the "gold standard" for clinical decision-making and treatment guidance[38]. However, CAG is associated with several limitations. First, CAG can evaluate the vascular lumen size and cannot provide detailed information about coronary plaque characteristics. Second, vascular stenosis assessment by using CAG is primarily

dependent on the comparison of lumen diameter ratios between the target segment and adjacent normal vessels. However, AS is a diffuse process, and the vessel used as a reference segment in the angiography image may not be healthy, which may lead to an underestimation of the lesion extent[39]. Third, during early CAD stages, the diseased blood vessels often undergo compensatory expansion, which can cause an underestimation of the disease extent by CAG. Fourth, CAG can only provide a visual representation of the contrast agent filling the vascular cavity and cannot accurately measure parameters such as the vascular wall thickness and cross-sectional area. Consequently, detecting coronary abnormalities with CAG is challenging when the degree of coronary stenosis is <40%. Finally, when intracoronary APs are eccentric or irregularly shaped, CAG may not allow comprehensive visualization of these plaques[40]. These limitations restrict the clinical utility of CAG. Intravascular ultrasound, which offers higher resolution and allows the observation of intravascular structures, has recently emerged as a preferred method for diagnosing coronary artery lesions. According to clinical research, many patients with normal CAG results have early AS and coronary endothelial disorders, as confirmed by IVUS imaging.

1.2.2.2 IVUS

Ultrasound imaging is extensively applied in clinical diagnosis by reason of its safety and ease of operation. IVUS has recently become a critical coronary artery imaging modality. During an IVUS imaging process, a catheter is carefully plugged into an

artery, and at the remote end of the catheter, an ultrasonic transducer emits ultrasound signals. By receiving different ultrasound echo signals from various tissue components with diverse acoustic impedance, real-time tomographic images including the artery wall structure and plaque tissue cross-section can be obtained[41]. IVUS presents clear sectional views of the adventitia, media, intima, APs, and vessel walls, thus enabling the diagnosis of early coronary lesions (Fig. 1.7). With IVUS, plaque tissue components can be differentiated on the basis of their acoustic characteristics, which facilitates the selection of appropriate treatment strategies[42]. Furthermore, the vascular lumen diameter and area, which are invaluable in evaluating the degree of coronary stenosis, guiding treatment options and interventional procedures, and assessing treatment effectiveness, can be measured using IVUS[43]. IVUS has been widely used clinically for the diagnosis and interventional treatment of CHD.

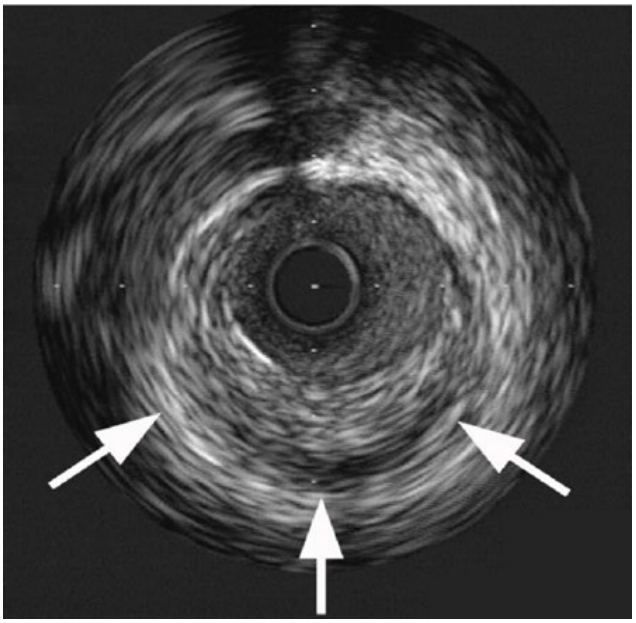

Fig. 1.7. IVUS image showing three lesions (white arrows)[15].

Despite remarkable advancements in IVUS, the ability to accurately differentiate plaque tissue characteristics is challenging because of low ultrasound image contrast, and the presence of noise and various artifacts. Although traditional IVUS can evaluate plaque characteristics based on echo intensity, it is limited in accurately distinguishing tiny VPs[44].

1.2.2.3 OCT

In OCT, an interferometer that evenly divides the light into detection and reference light paths is required for using the infrared light within the 800−1300 nm range. The detection light, which is directed toward the tissue, interacts with it and subsequently gets reflected. Different biological tissues have varying refractive indices, and so, the infrared optical density reflected by these tissues also varies[45]. On the other hand, the

reference light is modulated and reflected through the movable reference mirror, which enables it to interfere with the light response from the target tissue. This interference yields valuable information about the amplitude and delay of the tissue reflections (Fig. 1.8)[46]. The resulting interference light is then transmitted back to the signal processing system, and a 2D image is generated using specialized computer software [47].

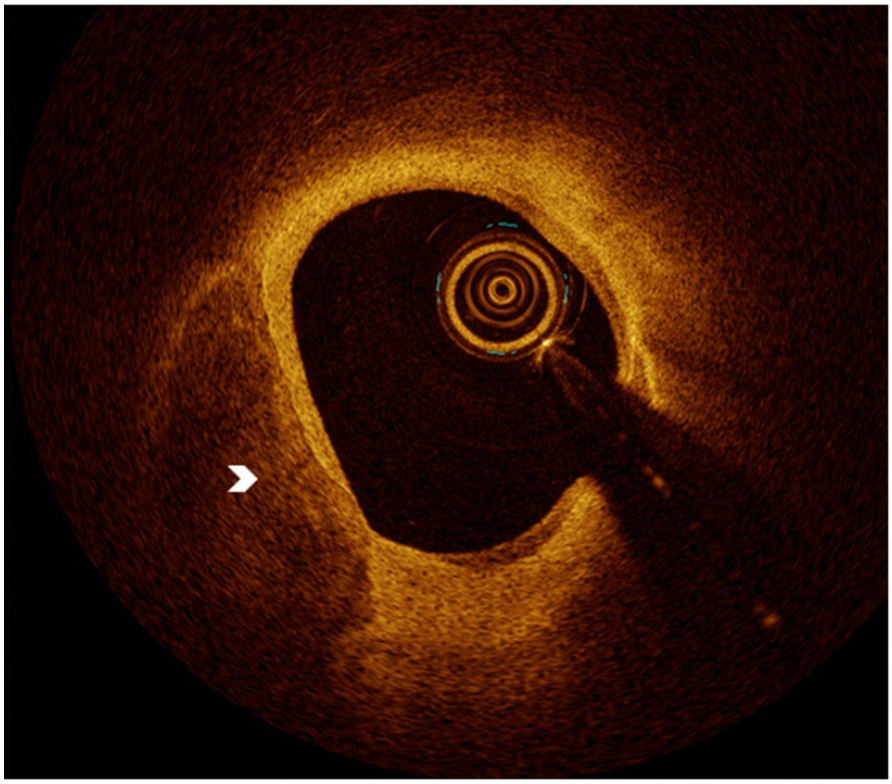

Fig. 1.8. OCT image of a highly calcified artery. The arrow indicates the border [46].

The technical principles underlying OCT are similar to those of IVUS. In both techniques, energy beams are used to scan the blood vessel cavity in a 360° manner aims to acquire cross-sectional morphology of vascular. However, OCT distinguishes

itself from IVUS through its exceptional spatial resolution. OCT is currently the technology with the highest spatial resolution (about 10 μm). This high resolution leads to the production of clear and detailed cross-sectional images of the vascular lumen, thereby making OCT particularly advantageous for examining plaque morphology.

Notably, OCT allows the visualization of distinct layers of the vessel wall, including the inner tunica intima, media, and adventitia, with remarkable clarity. Furthermore, it aids in accurately identifying different plaque types, measuring the fibrous cap thickness, and determining lipid size deposits within the plaque. Through a quantitative analysis of OCT signals, the optical attenuation coefficient of AP can be measured, thereby aiding in the differentiation of plaques from arterial wall components[48].

Notably, OCT extends beyond exhibiting the anatomical structure of the blood vessel; it also provides valuable insights into the characteristics of plaque, thrombus, tissue fragments, and other relevant features. Consequently, OCT is of great value in guiding interventional therapy.

1.3 IVUS Imaging Technology

The IVUS imaging system has three essential components: an imaging console, a catheter, and a rotation/pullback device[49]. The imaging console comprises the necessary hardware and software, such as an image processing unit, a computer, and a monitor. These items are used to convert ultrasonic signals into visual images. The

catheter serves as a conduit for the ultrasound transducer, allowing its insertion into the body's interior and facilitating direct imaging of the interior of blood vessels. The catheter is inserted through blood vessels or other ducts within the body. The ultrasound transducer, a fundamental element of the IVUS imaging system, generates sound waves and detects the resulting echo signals. Finally, the rotation/pullback device permits the rotation and pullback of the catheter, thus enabling capturing of more comprehensive 3D real-time images of the blood vessels.

1.3.1 IVUS Catheter

The IVUS catheter is a medical device designed specifically for obtaining ultrasound images of the cardiac artery in vivo. Regarding coronary interventional treatment, IVUS catheters typically have a diameter in the range of 0.9–1.0 mm, while its length is approximately 1.8–2.0 m. Owing to these dimensions, the catheter can easily reach the inside of the heart through the coronary artery, thereby facilitating the ultrasound examination and treatment of blood vessels.

The catheter itself has a flexible and slender shaft, typically composed of a polymer material. The ultrasound transducer, which is located at the catheter's tip, transmits and receives ultrasound waves to capture detailed images of the blood vessel (Fig. 1.9)[50].

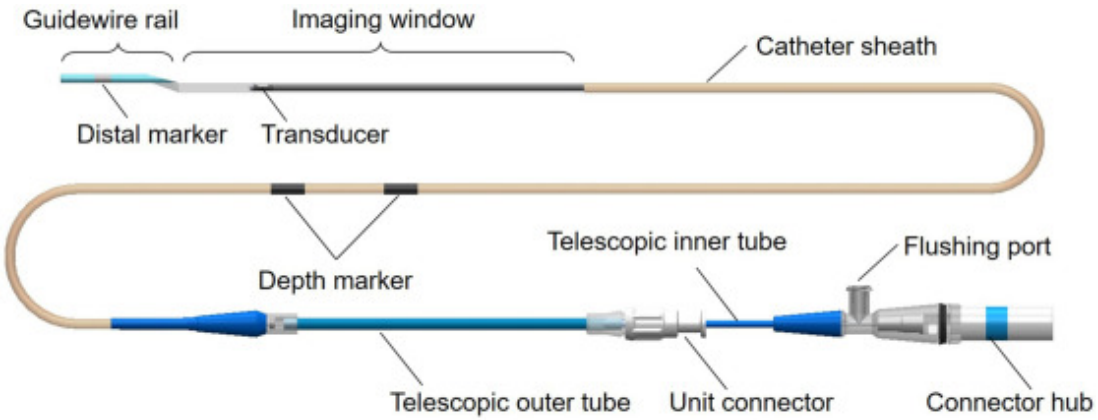

Fig. 1.9. Schematic of a mechanical IVUS catheter[50].

At present, several notable manufacturers produce IVUS catheters, including Boston Scientific, Terumo, and Philips. They offer a diverse selection of IVUS catheter products, thereby catering to different needs of the medical field. These advancements are aimed at promoting the imaging abilities and overall performance of IVUS catheters. Thus, healthcare professionals are provided with more comprehensive and precise information for diagnostic and interventional procedures.

1.3.2 IVUS Transducer

At the remote end of the IVUS catheter, a tiny transducer is positioned. The transducer primarily transmits High-frequency ultrasound (HFU) waves into the blood vessel and captures the resulting echo signals. After processing, these signals are converted into image data, and the formed images are displayed on the screen of the IVUS imaging platform. Thus, the doctors are provided with the detail information about the structure and size of the blood vessel.

1.3.2.1 IVUS transducers types

Based on the number of elements, IVUS transducers are categorized into single-element and phased array transducers[51, 52](Fig 1.10). The single-element transducer is arranged in a mechanical or rotational catheter, which rotates at high speeds because of a motor. While rotating, the transducer emits and receives ultrasound waves, allowing for the formation of cross-sectional ultrasound images of blood vessels[53]. Because of the rotational movement, detailed information from different angles can be gathered, which enhances the viewable of the vessel's internal morphology.

The phased array transducer has an array of 64 elements arranged radially around front-end of a solid-state catheter. Unlike the mechanical catheter, this catheter need not be rotated during imaging. Under the control of an imaging console, each element of the transducer sequentially transmits and receives ultrasonic waves. This sequential process allows the reconstruction of ultrasound images of the blood vessels[54].

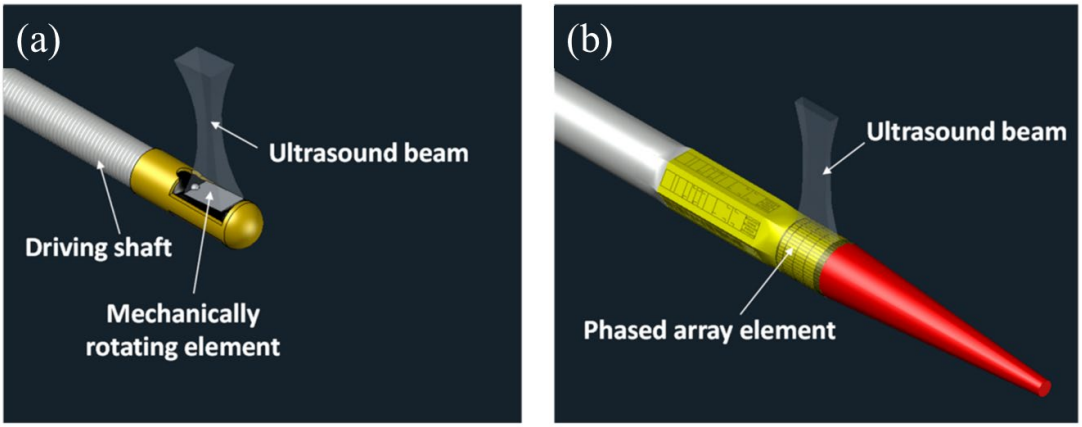

Fig. 1.10. Illustration of (a) mechanical and (b) solid-state IVUS transducers [52].

Because of its elevated frequency range (40–60 MHz), single-element IVUS has superior spatial resolution compared to phased-array IVUS (20 MHz). Nevertheless, a single-element IVUS has some limitations, namely the presence of guidewire artifacts and nonuniform rotational distortion, which substantially prevent the accurate diagnosis of APs.

1.3.2.2 Characterization of IVUS transducer

The IVUS transducer mainly includes electrical, acoustical, and imaging characteristics.

(1) Electrical characteristics

Impedance curve

The impedance curve of an IVUS transducer presents the impedance values at

different frequencies across its operating frequency range. It provides the transducer's electrical behavior and can help in impedance matching and optimizing the transducer's performance. Typically, the impedance curve is presented as a plot with frequency and impedance magnitude (|Z|) (Fig 1.11). This curve typically displays a minimum point called the resonant frequency, which corresponds to the point where the transducer's electrical and mechanical properties are matched, resulting in maximum energy transfer efficiency.

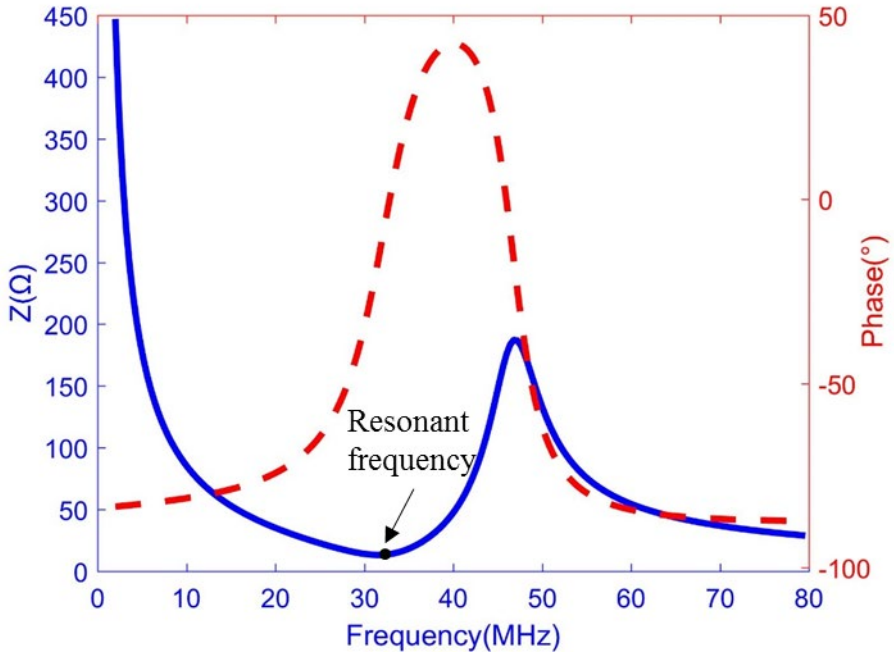

Fig. 1.11. An impedance curve example. Impedance curve (blue), phase curve (red).

Phase curve:

The phase curve of an IVUS transducer presents the phase shift of the electrical signal

across its operating frequency range. It provides the difference of phase between the input electrical signal and the transducer-emitted ultrasonic wave. The phase curve is typically plotted with frequency and phase shift (Fig. 1.11). Similar to the impedance curve, the phase curve exhibits a characteristic behavior at the resonant frequency. The phase shift is typically minimal or zero at the resonant frequency, which indicates a phase alignment between the electrical input and the generated ultrasound wave.

(2) Acoustic characteristics

Pulse-echo curve

The pulse-echo curve illustrates the shape of the received echo signal. It provides information about the transducer's response to the emitted pulse and the resulting echoes from a reflector. In general, the pulse-echo curve is plotted with time and signal amplitude on the X-axis and Y-axis, respectively (Fig. 1.12). The pulse-echo curve helps understand the transducer's ability to transmit ultrasound waves and detect reflected signals.

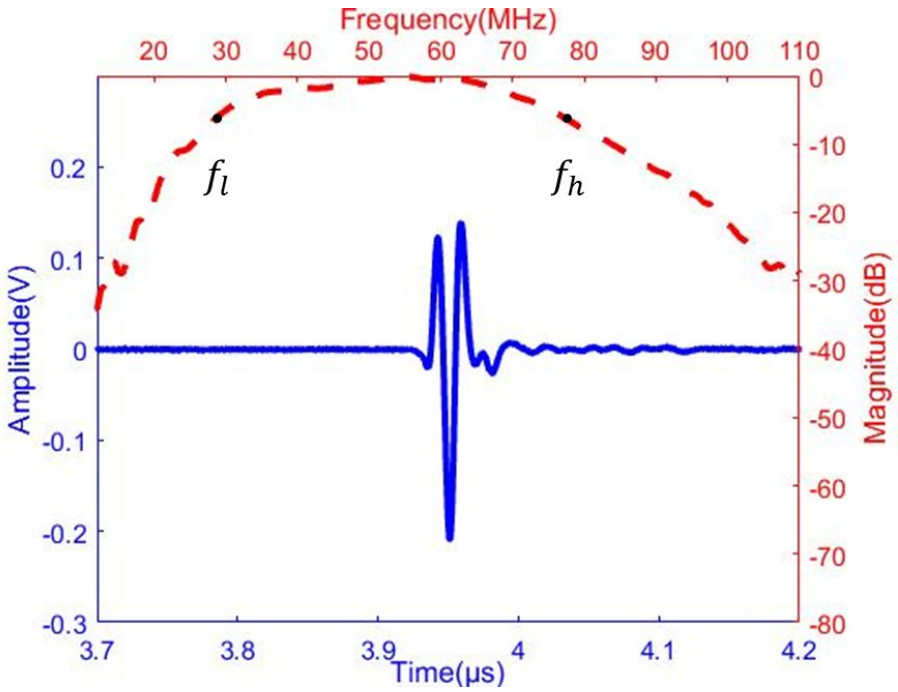

Fig. 1.12. A pulse-echo curve example. Pulse-echo curve (blue), frequency spectrum (red).

Frequency spectrum

The frequency spectrum generally refers to the distribution of frequencies present in a signal. In ultrasound imaging, the frequency spectrum is the range of frequencies present in the received echo signals (Fig. 1.12). An ultrasound wave transmitted into the tissue contains a range of frequencies because of the wave duration and shape. As the wave propagates through the tissue and interacts with various structures, echoes are generated at various frequencies. The frequency spectrum of the pulse-echo signals can be acquired through Fourier analysis. The Fourier analysis decomposes a complex signal into its constituent frequencies, and thus, the frequency components present in the echo signals can be identified.

The F_c and −6 dB BW can be calculated by applying the following equation that relies on the frequency spectrum:

$$F_c = \frac{f_l + f_h}{2} \tag{1.1}$$

$$\text{BW} = \frac{f_h - f_l}{F_c} \tag{1.2}$$

where f_l and f_h represent low and high frequencies at which the spectrum reaches -6 dB from the peak response.

Insertion loss (IL)

The insertion loss (IL) reflects the capability of a transducer to transform electrical signals into ultrasonic waves and detect ultrasound echoes[55].

$$\text{IL} = 20log_{10}\frac{V_o}{V_i} + Attn_{reflector} + Attn_{water} \tag{1.3}$$

In the aforementioned equation, V_o represents the echo signal, and V_i denotes the voltage of the input electrical signal. $Attn_{reflector}$ and $Attn_{water}$ represent the attenuation of the reflector and water medium, respectively. The IL is critical for the depth of imaging penetration.

(3) Imaging characteristics

Spatial resolution

The minimize distance between two distinguishable adjacent characteristics in an ultrasonic image is identified as spatial resolution[56]. It can be further classified as axial and lateral resolutions, representing the resolutions in the depth and width directions of the ultrasound image, respectively. The axial resolution allows the differentiation of features along the ultrasound propagation direction. The following formula provide a method to estimate axial resolution[57]:

$$R_{axial} = \frac{c}{2F_c BW} \tag{1.4}$$

where c is the sound speed. The formula demonstrate that a higher center frequency and wider bandwidth contribute to the superior axial resolution of the ultrasonic image.

Lateral resolution in ultrasound imaging is the ability to distinguish features perpendicular to the ultrasound propagation direction. It can be estimated as follows [57]:

$$R_{lateral} = \frac{cF_{\#}}{F_c} = \frac{cF_n}{F_c D} \tag{1.5}$$

where F_n represents the focal length of the ultrasound transducer, D denotes its aperture size, and $F_{\#}$ is the ratio of the focal length to the aperture size. Consequently, a higher center frequency and a smaller $F_{\#}$ contribute to an improved the lateral resolution of ultrasound image.

Contrast-to-noise ratio (CNR)

The CNR is the ability of IVUS imaging to distinguish the target area from the surrounding tissue. CNR is calculated as follows[58]:

$$CNR = \frac{|\mu_T - \mu_B|}{\sqrt{\sigma_T^2 + \sigma_B^2}} \tag{1.6}$$

where μ_T and μ_B are the mean acoustic intensities within the target and background area, respectively. σ_T and σ_B are the standard deviations of the acoustic signal intensity within the target and background area, respectively. The CNR represents the relative difference in acoustic intensities. Higher CNR values indicate better differentiation and clearer visibility of small target features against the background tissue.

Signal-to-noise ratio (SNR)

The SNR is the capability of a transducer to identify the acoustic signal above the background noise. It is the ratio of the amplitude of the acoustic signal to the background noise. SNR is calculated as follows:

$$SNR = 20log_{10}\frac{V_{tissue}}{V_{noise}} \tag{1.7}$$

where V_{tissue} is the amplitude of the signal detected from a target area, while V_{noise} is the amplitude of noise. SNR indicates the voltage of the signal above the noise. A

larger SNR demonstrates a more detectable echo signal in relation to the noise, which leads to improved image quality and enhanced ability to visualize structures of interest.

1.3.3 IVUS Coded Excitation Technology

The attenuation of sound waves in ultrasonic propagation is proportional to the frequency. Higher frequencies result in greater attenuation[57]. Consequently, when a higher resolution is desired by increasing the imaging frequency, a trade-off occurs with a significant reduction in penetration depth. One direct approach for enhancing the penetration depth is to increase the transmitting power by raising the excitation voltage or extending the excitation pulse duration. However, in medical ultrasound diagnostic systems, the peak intensity of the excitation signal is limited because of safety concerns.

Coded excitation, an advanced signal processing technique, has made significant progress in increasing the penetration depth in HFU imaging[59]. Using a modulated waveform with a longer duration in coded excitation enables multiple energy transfers into tissues[60]. Compared with conventional short-pulse excitation schemes, coded excitation imaging offers noteworthy improvements in the SNR, with transmit energy increasing to more than 10 dB[61]. This enhancement in SNR contributes to improved image quality and diagnostic accuracy in HFU imaging.

Fig. 1.13 presents the comparison between traditional ultrasound imaging and coded excitation imaging. The differences between the two techniques include:

Transmitting part: In coded excitation imaging, the transmitting waveform comprises a modulated long-pulse sequence. Because of this modulated waveform, multiple energy pulses are transferred into tissues, extending the penetration depth. By contrast, traditional imaging employs short pulses for excitation.

Receiving part: In coded excitation imaging, the receiving process involves pulse compression for achieving an axial resolution comparable to that of traditional imaging. Pulse compression is a signal processing technique that combines echoes received over a longer duration, thereby resulting in an improved axial resolution.

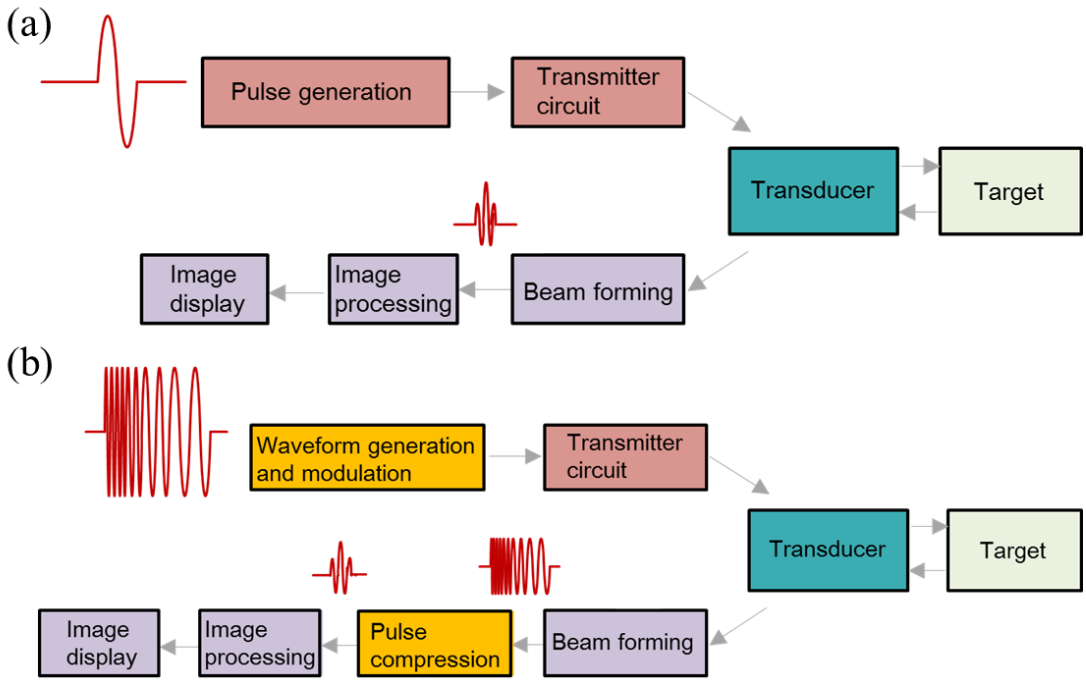

Fig. 1.13. Comparison of (a) traditional and (b) coded excitation ultrasound imaging.

Coded excitation imaging commonly uses two coding methods: frequency coding and phase coding. Phase coding is a binary coding form and includes coding techniques such as Golay code, M sequence, and Barker code. On the other hand, frequency coding employs Chirp code. Chirp coding is considered the optimal and most stable coding method in ultrasound imaging[60]. Therefore, in this thesis, Chirp coding was selected as the coding method for investigation and analysis.

In the Chirp excitation waveform, the instantaneous frequency varies linearly with time. With this linear frequency modulation, a broad range of frequencies can be transmitted. The Chirp excitation waveform can be expressed as follows:

$$s(t) = \alpha(t) \cdot \cos(2\pi f_0 t + \pi b t^2) \tag{1.8}$$

where $s(t)$ represents the Chirp excitation waveform at time t. $\alpha(t)$ is a window function used to shape the waveform. The starting frequency of the Chirp waveform is denoted as f_0. b is the sweep rate and can be calculated by $(f_1 - f_0) / T$, where f_1 is the ending frequency and T indicates the waveform duration.

The demodulation process in the receiver involves convolving the echo signal with a compression filter. Mathematically, the following convolution operation is performed:

$$s_r(t) * p(t) = \int_{-\infty}^{\infty} s_r(\varphi) p(t - \varphi) d\varphi \tag{1.9}$$

where the ultrasound echo signal is represented as $s_r(t)$, and a compression filter is

denoted as $p(t)$. Because of this procedure, the demodulated signal transforms into a signal of short-duration, which resembles the echo signal obtained through the excitation of short-pulse.

By increasing the duration of excitation signal, Chirp coding excitation effectively increases the transmission power and causes improvements in both the imaging depth and SNR compared with traditional short-pulse excitation. Fig. 1.14 illustrates the comparison of imaging effects between these two methods[62].

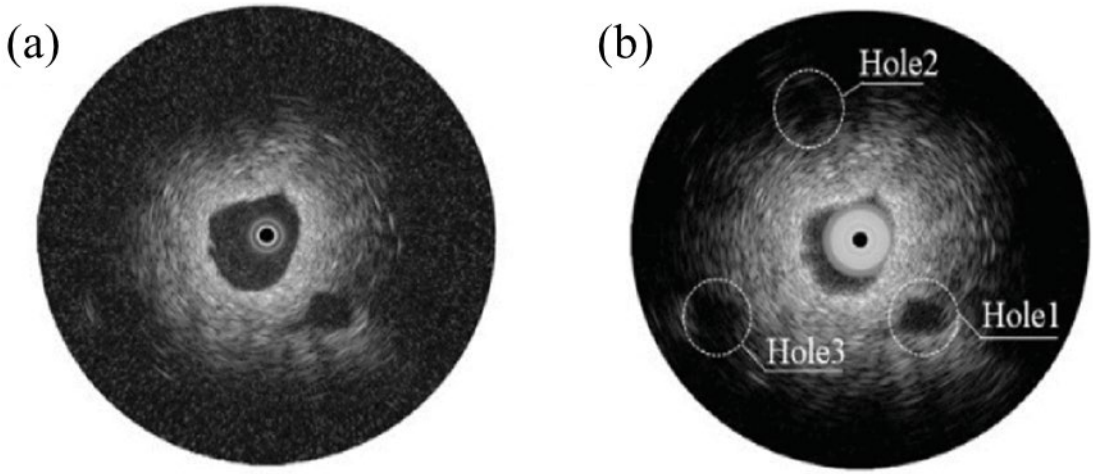

Fig. 1.14. Images acquired by (a) sine pulse and (b) Chirp-coded excitation[62].

The comparison confirms that Chirp code excitation imaging exhibits a noticeable increase in both the SNR and penetration depth, which are crucial for obtaining clearer and more detailed ultrasound images. These images allow better visualization and analysis of the underlying structures.

1.3.4 Imaging Process of IVUS System

(1) IVUS signal processing.

In mechanical IVUS, ultrasound imaging involves a single transducer that operates in a transmit-receive mode. The imaging console generates a trigger signal synchronized with the transducer's rotation. Then, the console then transmits an electrical signal to the transducer. The signal is transformed by the transducer into ultrasound wave, which is emitted into the target. When the ultrasound waves encounter interfaces within the target, they are reflected toward the transducer. The transducer then detects the reflected ultrasound signals and converts them back into electrical signals. This transmission and reception of ultrasound signals occur repeatedly with each rotation of the transducer, allowing for image data acquisition for IVUS imaging. Fig. 1.15 illustrates the IVUS signal processing.

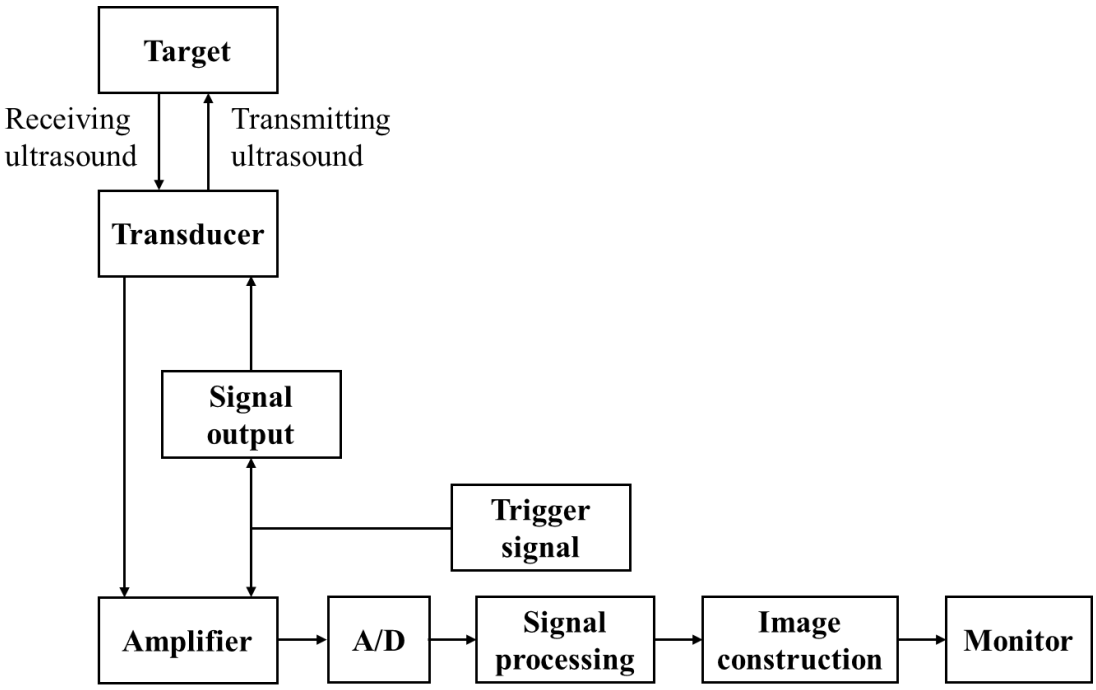

Fig. 1.15. Flowchart depicting the IVUS signaling processing.

(2) IVUS image construction processing.

The image construction process of the IVUS system is displayed in Fig. 1.16[50]. In Fig. 1.16 (a), the echo data represent information captured from a single scan line during a single transmission and reception of the IVUS transducer. In Fig. 1.16 (b), a complete image frame is formed by multiple scan lines. The horizontal value is the number of scan lines (range: 256–1024 lines), while the vertical value is the number of sampling points along each scan line, corresponding to the imaging depth. Higher linear density results in finer image details. However, it also increases the amount of data per frame, leading to a decrease in frame rate. Fig. 1.16 (b) presents the 2D matrix of information. However, the actual IVUS image appears circular, as depicted

in Fig. 1.16 (c). To achieve this circular image, a transformation from Cartesian to polar coordinates is required.

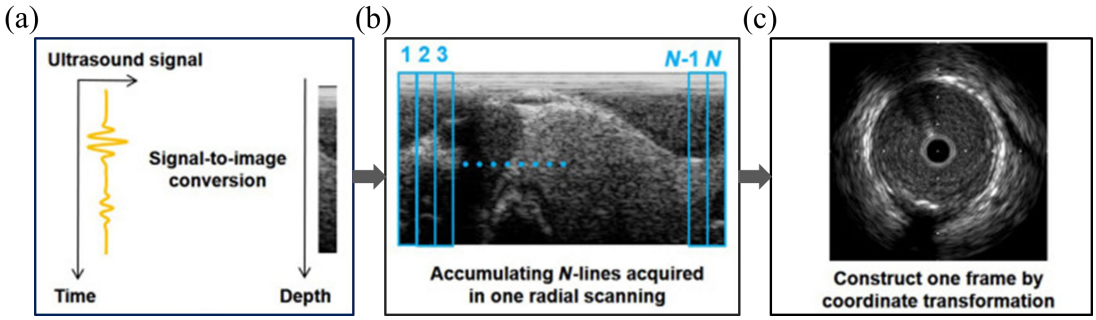

Fig. 1.16. The image construction process of the IVUS system. (a) Single-line scanning. (b) Radial scanning. (c) Image construction[50].

(3) IVUS imaging data processing.

Fig. 1.17 illustrates the data processing steps involved in IVUS imaging. The original RF data are obtained using the analogue-to-digital converter (ADC) and collected by the field programmable gate array (FPGA) in the hardware system. These data serve as the input data. To eliminate out-of-band noise, the original data are first subjected to bandpass filtering, followed by envelope demodulation for extracting the amplitude information of the echo signals, which enables B-mode imaging. In the envelope extraction process, the in-phase (I) and quadrature (Q) signals are obtained through a Hilbert transform. By using Cordic, the modulus of the I/Q signal is computed to eliminate the carrier frequency and extract the envelope. The demodulated data are logarithmically compressed to facilitate subsequent grayscale display with 256 levels.

The digital scanning transformation is employed to convert the data from Cartesian to polar coordinates, thereby a more intuitive display of cross-sectional images of blood vessels is achieved.

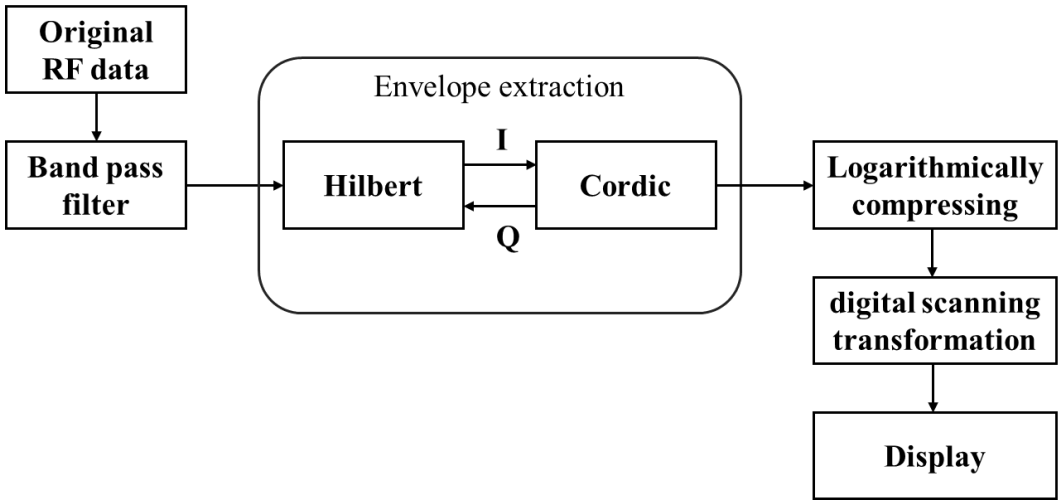

Fig. 1.17. Flowchart depicting the IVUS imaging data processing.

1.3.5 IVUS Image Post-Processing.

Grayscale IVUS imaging offers valuable details of the artery wall structure and plaque size. However, this technique has limitations in quantitatively assessing the plaque tissue composition. Certain plaque components, such as dense fibrotic tissue and calcified tissue, exhibit strong echogenic reflections, and differentiating these reflections by using grayscale IVUS images alone is challenging. To address this problem, various techniques have been proposed to post-process echo signals and generate images depicting complex and VP tissue. Fig. 1.18 illustrates four commonly employed clinical IVUS RF signal analysis methods[63]. These methods better

enhance the characterization and visualization of plaque tissue composition than conventional grayscale IVUS imaging.

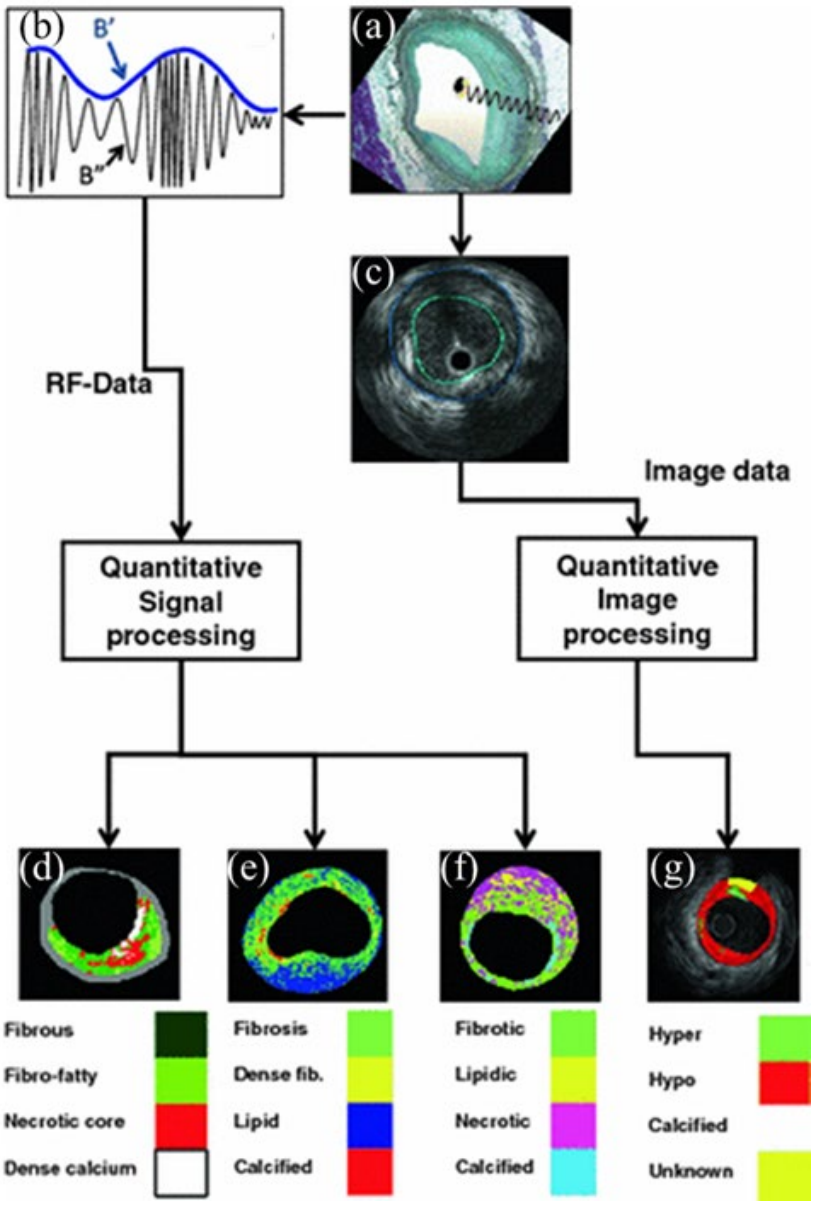

Fig. 1.18. A variety of IVUS image post-processing. (a) IVUS propagation in tissues. (b) RF signal. (c) Gray-scale IVUS image. (d) VH-IVUS image. (e) IB-IVUS image. (f) iMAP–IVUS image. (g) ADE image[63].

VH-IVUS is the pioneering commercially available tool designed for IVUS that can analyze tissue composition. It has been widely utilized in clinical medicine[64]. Unlike conventional grayscale IVUS, VH-IVUS uses the envelope amplitude of the echo signals and performs spectrum analysis on these signals of different tissues. By leveraging the distinct echo frequencies of various plaque tissues, VH-IVUS simulates and displays the plaque tissue composition, thereby establishing a corresponding color atlas. This tool allows a more intuitive qualitative and quantitative evaluation of plaque composition. VH-IVUS uses a mathematical autoregressive model for identifying four fundamental plaque tissue components[65]. With the detailed tissue characterization obtained through VH-IVUS, the evaluation of plaque composition is improved, thereby supporting clinical decision-making processes.

iMAP-IVUS uses an algorithm to analyze the echo signal spectrum. It generates color-coded images that are integrated with the grayscale IVUS images[66]. These color-coded images provide additional details about the plaque composition by assigning different colors to specific tissue types. By integrating the images as mentioned above, iMAP-IVUS improves the visualization and characterization of plaque components.

In the IB-IVUS analysis, which is an alternative approach, RF signals are analyzed by employing a Fast-Fourier Transform (FFT) to calculate the power of the components of frequency within the backscattered signal. The signal strength can be calculated in this

analysis, typically in decibels (dB)[67]. Different plaque components exhibit varying power levels in their reflected RF signals. With the quantification of the signal strength at different frequencies, IB-IVUS can distinguish between tissue components based on their distinctive power profiles. This method offers valued information into the relative composition and characteristics of different plaque tissues, thereby aiding the identification and assessment of specific tissue styles within the artery.

Unlike the aforementioned analysis methods of RF signals, ADE employs the differences in grayscale intensity within grayscale IVUS images to characterize the components of hardened APs[68]. This approach is dependent on the varying acoustic properties, such as echogenicity, of different tissue components. The quantitative IVUS analysis determines the relative gray values of specific regions, so as to detect variations in the grayscale intensity. Plaque components are classified based on these differences. For instance, hyperechoic regions with grayscale values higher than the adventitia layer are identified as hardened plaque components. Moreover, bright components with extremely high grayscale values, accompanied by acoustic shading, are always recognized as calcium deposits. However, components within the acoustically shadowed regions, where a calcium layer predominantly reflects the ultrasound wave, are classified as unknown. This method can be applied to previously acquired IVUS data, regardless of the specific IVUS console or catheter employed.

1.4 Development of IVUS Transducers

The preceding section of the thesis clarifies that the sensitivity and resolution of the transducer significantly impact IVUS image quality. Consequently, numerous studies have been conducted to enhance these specific aspects of the transducer to improve its overall performance.

1.4.1 High Resolution IVUS Transducers

1.4.1.1 Broad bandwidth IVUS transducers

Factors such as the Fc and BW of the IVUS transducer decide its axial resolution. To enhance the bandwidth, the utilization of PMN-PT and PIN-PMN-PT single crystals have been explored. These particular crystal materials have exceptional electromechanical coupling coefficients, hence, they are favorable choices for IVUS transducer production. Furthermore, 1–3 composite materials have been implemented to further enhance the bandwidth. These composite materials consist of piezoelectric material rods or fibers embedded in a polymer substrate, which results in increased bandwidth and improves the overall performance of the IVUS transducer[69, 70].

1.4.1.2 Dual-frequency IVUS transducers

Conversely, research has been conducted to increase the center frequency of IVS transducers and thus improve their resolution[71]. However, higher transducer frequencies result in greater attenuation and shallower imaging penetration depths. In

response to this challenge, Ma et al. introduced a technique called dual-frequency IVUS (DF-IVUS) in 2015[72]. In this technique, catheters with back-to-back arrangements of ultrasonic elements operating at different frequencies were used. Fig. 1.19(a) illustrates the structure scheme and prototype of the transducer. These catheters were used for ex vivo coronary ultrasound imaging (Fig. 1.19). The high-frequency images generated provided greater details of the vessel wall, whereas the low-frequency images facilitated imaging of tissues located deeper within the vessel.

Furthermore, Munding et al. developed another method to fabricate a DF-IVUS catheter[73] and conducted in vivo experiments on pigs[74]. They demonstrated the feasibility of using DF-IVUS and showcased its potential for commercial product development. Another study proposed an optimized structure prototype featuring one coaxial connection with two elements, thereby further advancing DF-IVUS development[75].

These collective advancements in DF-IVUS technology have propelled its progression and hold promise for improving resolution and imaging capabilities in IVUS applications.

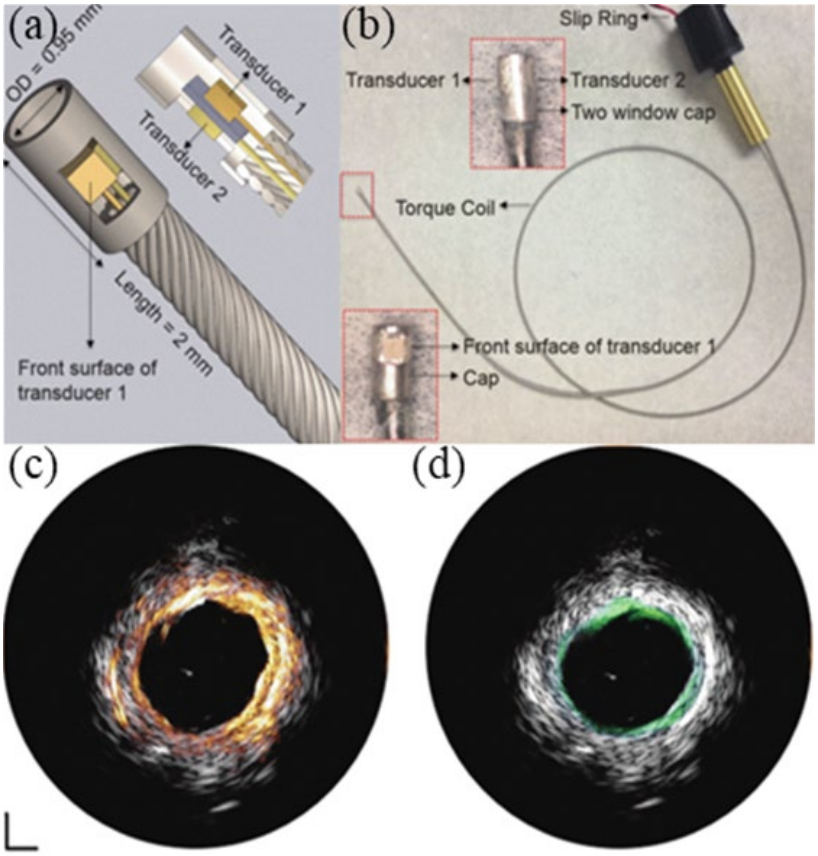

Fig. 1.19. (a) The structure diagram and (b) prototype of DF-IVUS, ultrasound images of (c) 35/90 MHz and 35/120 MHz IVUS[72].

DF-IVUS has been used for harmonic imaging (HI) to improve imaging resolution. In HI, a waveform is transmitted at a fundamental frequency and the response is received and imaged at multiple frequencies, which are multiples of the transmitted frequency[76], Using this approach, contrast and spatial resolutions can be improved simultaneously[77].

In 2015, Ma et al. developed a novel DF-IVUS catheter with a stacked configuration. This transducer was specifically designed for intravascular acoustic angiography[78].

This transducer utilized either a 6.5 MHz or a 5 MHz transducer for transmitting ultrasound waves, while a 30 MHz transducer was employed for receiving the waves (as depicted in Fig. 1.20a). It employed a 6.5-MHz or a 5-MHz transducer for transmitting ultrasound waves, while a 30-MHz transducer was employed for receiving the waves (Fig. 1.20a). The reception transducer was placed in front of the transmission transducer and had a smaller aperture than the reception transducer. Therefore, a portion of the transmission transducer was obstructed by the reception transducer. Lee et al. demonstrated a more refined structure by arranging the elements side-by-side at an angle[79] (Fig. 1.20b).

The HI DF-IVUS transducers provided several advantages in the acquired ultrasonic images, such as improved resolution, reduced reverberation effects, high contrast imaging of hyperechogenic regions, and enhanced imaging depth. Additionally, studies have investigated super-HI[80] and frequency compound imaging using DF-IVUS[81], thereby exploring the applications of HI in DF-IVUS.

These advancements in HI DF-IVUS contribute to enhanced imaging capabilities, higher resolution, and improved contrast for various clinical applications.

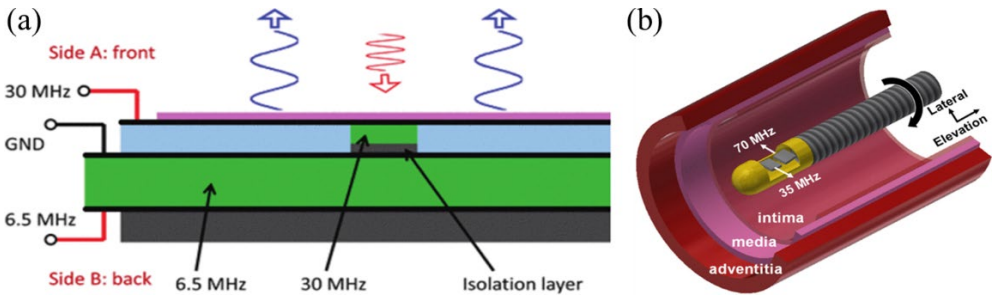

Fig. 1.20. The structure scheme of (a) stacked configuration DF-IVUS catheter [80] and (b) side-by-side DF-IVUS catheter[81].

One approach for increasing the imaging resolution is to focus on the ultrasound beam. Two primary means for beam focusing a single-element transducer are using an acoustic lens or a concave geometric surface. However, in IVUS transducers, which have high frequencies and small sizes, an acoustic lens is not suitable for beam focusing. Consequently, in numerous studies, the transducer was pressed into a concave spherical surface to achieve beam focusing.

1.4.1.3 Focused IVUS transducers

Chen et al.[82] and Yoon et al.[83] have used diverse processing procedures to enhance the imaging resolution of IVUS in which transducers with concave spherical surfaces were employed. Subsequently, 1-3 composite-focused IVUS has been proposed to further enhance imaging performance[84]. Moreover, the use of new piezoelectric materials and structures has been explored for the fabrication of focused IVUS transducers[85, 86]. Because of the tiny size of these piezoelectric elements in IVUS catheters, achieving a well-focused acoustic field is challenging.

1.4.2 Multi-Mode Intravascular Imaging Catheters

1.4.2.1 IVUS/OCT catheters

Although numerous methods have been proposed for enhancing the IVUS imaging resolution, clear visualization and characterization of the fibrous cap in VPs remain challenging. A dual-mode imaging approach combining OCT with IVUS has been employed to overcome this limitation. This combination approach offers complementary information from modalities, thereby enabling better VP identification and assessment.

OCT has gained considerable popularity in clinics for intravascular applications because of its ability to deliver super-resolution (approximately 10 μm) images[87]. To utilize the incorporate strengths of OCT and IVUS, Li et al. demonstrated a catheter in 2010 that integrates both modalities for intravascular imaging[88]. Their catheter design incorporated a ring-shaped focused transducer and an OCT probe positioned inside the transducer's central hole. A 45° mirror was arranged on the front of the combined probe to direct the light and ultrasound beam to the surrounding tissue (Fig. 1.21a). The images obtained from the rabbit aorta using this combined OCT/IVUS catheter had an enhanced penetration depth and resolution. Subsequent studies by Li et al. further verified the effectiveness and potential of this imaging technology[89, 90].

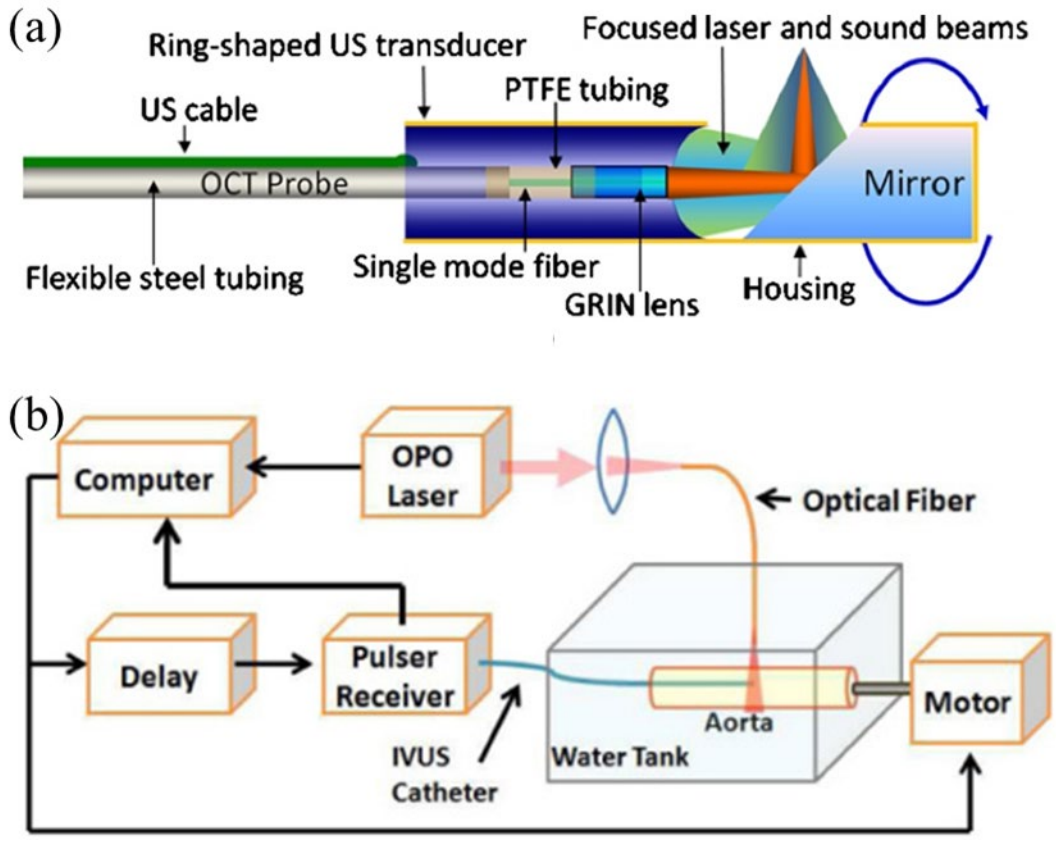

Fig. 1.21. (a) Schematic diagram of a typical IVUS/OCT catheter [88], (b) workflow diagram of an IVUS/ photoacoustic tomography (PAT) system[91].

1.4.2.2 IVUS/IVPA catheters

VPs often contain components such as lipids that cannot be easily distinguished in ultrasound images alone. Consequently, IVUS/intravascular photoacoustic (IVPA) imaging leverages the strengths of different imaging techniques and improves the prediction and evaluation of various plaque components, thereby enhancing the diagnostic capabilities of VP assessment.

In IVPA imaging, nanosecond pulsed lasers are applied to heat the surrounding tissue,

thus causing rapid thermal expansion. This expansion generates an acoustic transient pulse, which is detected by the IVUS transducer and also used for B-mode ultrasound imaging. Because of its high Grüneisen coefficients, lipids are an efficient medium for generating photoacoustic transients. Consequently, IVPA imaging is excellent in diagnosing lipid-rich plaque detection[31].

Wang et al. created an integrated IVUS/PAT imaging system (Fig. 1.21b)[91]. In this system, the IVUS transducer is positioned inside the blood vessel, whereas the optical fiber is located outside the blood vessel. The IVUS transducer receives photoacoustic signals generated through laser light irradiation of the tissue[30]. This study presents a novel approach for detecting lipid-rich plaques. However, the optical fiber placed outside the vessel may potentially compromise the accuracy of PAT evaluation. Additionally, other imaging technologies must be used to locate the IVUS catheter during the experiment.

1.4.2.3 B-mode/Functional parameters IVUS catheters

In addition to traditional B-mode images, the incorporation of other functional parameters such as BFV can offer valuable insights into plaque properties[92]. With these additional parameters, a more comprehensive evaluation of plaque characteristics and potential risk becomes possible.

Hong et al. developed an innovative intravascular catheter combining flow speed

detection with B-mode ultrasound imaging capabilities[93]. The catheter design incorporated two ultrasound elements: a 20-MHz element placed at the front of the catheter for flow detection and a 40-MHz element situated on the side for B-mode imaging (Fig. 1.22a). With this configuration, flow speed information and ultrasound images of the vessels can be acquired simultaneously. The integrated catheter serves as an important device for diagnosing CVD by allowing comprehensive and real-time assessment of BFV characteristics and vessel morphology.

The aforementioned integrated catheter enables clinicians to obtain important hemodynamic information and visualize vessel structures. This combined functionality improves the diagnostic capabilities of the catheter and allows a more comprehensive evaluation of cardiovascular health. Flow speed and ultrasound images when acquired simultaneously improve the understanding of CVD and assists in accurately diagnosing and treating patients.

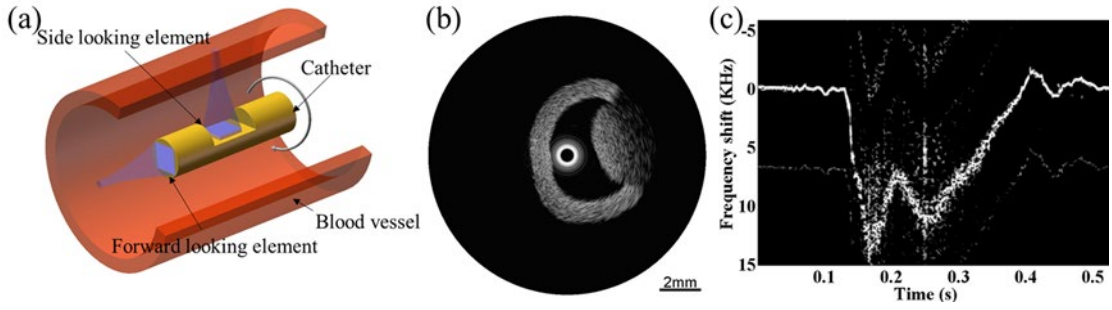

Fig. 1.22. (a) The dual-mode catheter, (b) B-mode ultrasound and (c) pulsatile flow images[93].

1.4.3 Summary

High resolution and multimodality are the primary development directions for IVUS catheters, which enhance imaging quality. Several methods are used to enhance the IVUS imaging resolution, including increasing the bandwidth and the center frequency and implementing acoustic beam-focusing techniques.

bandwidth can primarily be improved by using new materials characterized by high electromechanical coupling coefficients, piezoelectric coefficients, and a single crystal structure. Examples of such materials are PMN-PT, PIN-PMN-PT, and 1–3 composites.

Enhancement of the center frequency leads to higher attenuation. Consequently, DF-IVUS has been developed. In this system, multiple elements (≥2) are arranged in a catheter in a back-to-back or side-by-side configuration to facilitate fundamental imaging and HI. The low-frequency element ensures sufficient ultrasound imaging depth, whereas the high-frequency element provides superior imaging resolution. However, DF-IVUS has drawbacks such as a larger catheter size than standard IVUS and a complex mechanical connection, which may limit its application.

Geometric focusing is a valuable method for focusing the acoustic beam of IVUS. However, it is associated with challenges when a well-defined focal acoustic beam is desired for the miniature size of IVUS transducers. Moreover, fabricating a

geometrically focused IVUS transducer is arduous because of its tiny size.

Multi-mode IVUS catheters are used to obtain additional assessment parameters by combining techniques such as OCT, IVPA, NIRS, and NIRF with IVUS. This integration substantially improves the quality of AP assessments. However, these technologies also have drawbacks. For example, IVUS/OCT systems tend to be bulky and expensive. Moreover, the clinical processing of IVPA/IVUS encounters challenges because of the limitations in the penetration depth of the in vitro laser.

Despite these challenges, ongoing advancements in transducer, optical, and electronic technologies are expected to overcome these obstacles. Advancements in the quality of AP assessment and the application of a wider range of evaluation parameters have made CVD diagnosis increasingly quantitative. Customized diagnosis, where different assessment methods are used based on patient-specific conditions such as obesity, vascular stenosis, and hypertension, will soon become a trend.

1.5 Significance of this Thesis Work

The IVUS imaging device has advanced to a great extent in many medical companies, and its clinical applications are continuously expanding. However, certain technical limitations related to this device persist and need to be resolved:

Resolution limitation: The spatial resolution of conventional IVUS devices is limited.

This may result in insufficient clarity when certain structures, such as APs, are displayed. This limitation can impact lesion detection and diagnosis.

Image distortion: During IVUS detection, the mechanical catheter has to rotate at high speeds. However, factors such as resistance in narrow blood vessels and mechanical structures, this rotation may be uneven, leading to distortion of the obtained ultrasound images.

Imaging depth: Ultrasound waves are absorbed and reflected when propagating through tissues and organs in the human body. This can make clear visualization of deeper target areas challenging. Supplementary imaging technologies or adjustments, such as changing the position or direction of the ultrasound transducer, may be necessary.

To address these issues, we designed and fabricated two focused IVUS transducers by using different materials and structures to increase IVUS imaging resolution. In addition, we developed a dual-element IVUS catheter for improving the quality of mechanically scanned IVUS images. With an improved image resolution, an expanded visualization range, and advanced imaging capabilities, these novel IVUS technologies offer clinicians unprecedented insights into the intricate details of arterial walls, plaque characteristics, and vascular structures. These technologies also provide more accurate and comprehensive information, thereby enabling precise assessment of disease severity, better selection of treatment strategies, and improved guidance during

interventional procedures.

1.6 Research Objectives

This study aimed to implement some precise enhancements to IVUS imaging technology, with a particular focus on improving the quality of IVUS images. These enhancements primarily revolve around advancements in transducer technology and the imaging platform.

The research objectives are as follows:

1. To design and fabricate a focal HFU transducer with a FZP layer for IVUS.

2. To design and fabricate a focal HFU transducer using PIN-PSN-PT ceramic for IVUS.

3. To design and fabricate a dual-element catheter for upgrading NURD conditions in IVUS imaging.

1.7 Outline of the Dissertation

This thesisi is arranged as follows:

Chapter 1 explains the background of IVUS imaging in terms of CVD, AS, CVD imaging techniques, IVUS imaging systems, and IVUS transducers.

Chapter 2 presents applying an FZP layer on the front face of a HFU transducer with meant to enhance the lateral imaging resolution of IVUS.

Chapter 3 presents a focal HFU transducer with geometric focusing using PIN-PSN-PT ceramic meant to enhance the lateral imaging resolution of IVUS.

Chapter 4 presents a dual-element catheter meant to improve the imaging rate and eliminate the NURD of mechanical IVUS imaging.

Chapter 5 provides a comprehensive summary of the study's results. It also highlights suggestions for future research, indicating potential directions for investigation in this field.

Chapter 2 Focal IVUS Transducer with a Fresnel Zone Plate Layer

2.1 Introduction

Conventional IVUS imaging is performed at frequencies between 20 and 60 MHz, with axial and lateral imaging resolutions of 50–120 μm and 150–250 μm, respectively[94], and these resolution cannot clearly distinguish TCFA thin cap fibro atheroma (TCFA). While, ultra-high frequency (UHF) IVUS transducers with frequencies exceeding 80 MHz have demonstrated remarkable axial resolution (~ 20 μm)[74], they often face challenges in achieving an ideal lateral resolution. And, the penetration depth of image is restricted owing to the significant attenuation of UHF ultrasound waves as they propagate through tissue. Focusing IVUS transducers have also been proposed to achieve clearer imaging (as shown in Fig.2.1). A focal transducer is designed by Chen et al. and Lee et al. to concentrate the ultrasound energy into a narrower beam, allowing for better spatial resolution and enhanced image quality[95]. However, the fabrication of geometrically-focused IVUS transducers can be challenging due to their small sizes, typically less than 1 mm. Additionally, achieving a well-focused acoustic beam in the transducer requires larger piezoelectric elements compared to traditional planar elements. This size limitation can pose challenges in practical clinical applications, as the transducer needs to be inserted into narrow blood vessels.

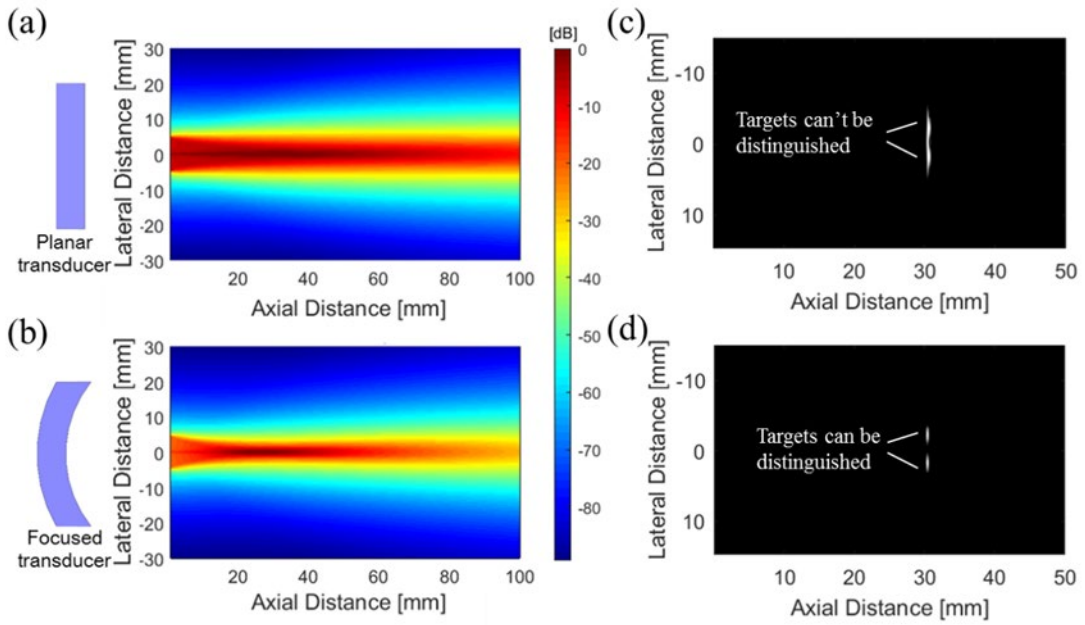

Fig. 2.1. Acoustic fields of (a) planar and (b) focused transducers; ultrasonic images obtained by (a) planar and (b) focused transducers.

Acoustic meta-lenses are currently a bright focusing strategy for a large number of imaging applications, including ultrasound imaging. Chen et al. designed an ultra-compact meta-surface lens to focus ultrasonic beam[96]. An acoustic meta-lens based on super-oscillating wave-packet was designed by Shen et al. and published in Nature Communications, which can break the far-field diffraction limit and improve the imaging resolution[97] (Fig 2.2). These acoustic lenses are applied to low-frequency (<1MHz) transducers to improve the imaging performance at those frequencies. The design and implementation of meta-lenses for high-frequency transducers pose additional challenges owing to the increased attenuation of HFU waves by the meta-lens layer.

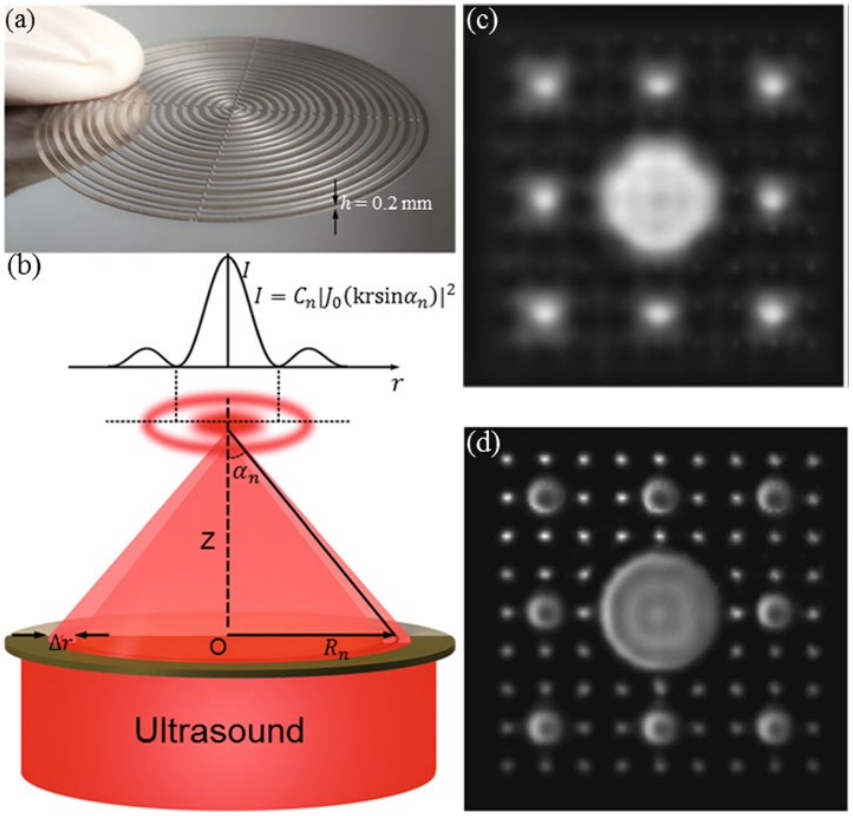

Fig. 2.2. (a) Super-oscillating acoustic meta-lens sample; (b) Diffraction effect of FZP on ultrasound; (c) Ultrasonic image of ordinary transducer; (d) Ultrasonic image of super-oscillating transducer[97].

FZP is a type of lens that has a foundation for the theory of diffraction and interference. It is composed of a range of concentric rings or zones that alternate between transparent and opaque regions. These zones are designed in a way that they cause constructive interference at a specific focal point, allowing the FZP to focus wave fields. Phase-reversal (PR) FZPs and Soret-type FZPs are the main types of FZPs[98, 99]. In Soret-type FZPs the transparent and opaque regions of the zones have different thicknesses. The difference in thickness creates a phase delay in the transmitted wavefront, leading to constructive interference at the focal position.

Soret-type FZPs are commonly used in optical systems[100]. These FZPs can be easily implemented in air[101, 102], where solid materials are used as the opaque zones and air acts as the transparent zones. The solid materials used in the FZP can have huge attenuation or large impedance differences with the surrounding medium, making them acoustically opaque. In contrast to the Soret-type FZPs, the transparent and opaque regions of PR-FZPs have the same thickness, but they alternate in phase. The phase shift between adjacent zones causes constructive interference at the focal area, resulting in focusing of the wave field. PR-FZPs are widely used in acoustic and ultrasonic imaging applications[98, 99]. Thus, in a Soret-type FZP, only sound waves passing through the acoustically transparent region contribute to the focus. However, in a PR-FZP, both sound waves passing through the acoustically transparent region and those passing through the obstructed region contribute to the focus. Therefore, a PR-FZP lens specifically designed for HFU transducers is proposed here due to its higher lens efficiency and focal strength. The ultrasound waves transmitted by the transducer will undergo diffraction by the Fresnel zone of the FZP lens stacked on the surface of the planar transducer and converge to the focal area[103], Additionally, the full width at half maximum (FWHM) of the focal region of the FZP transducer is smaller compared to that of a planar transducer without an FZP layer. This implies that the FZP serves the dual purpose of increasing the sound intensity of the transducer and reducing focal spot size.

This work stacks an FZP layer on the front surface of a planar HFU transducer, developing an FZP transducer and applying it to IVUS imaging. The FZP layer has the ability to diffract HFU waves passing through it. This diffraction makes the HFU waves to combine in the focal area, thereby enhancing the imaging resolution of IVUS. Finite element simulation software is utilized to simulate the acoustic beams produced by FZP transducers and planar transducers. Additionally, the measurement of transducer's electrical impedance and pulse echo are conducted. To evaluate the imaging resolution of the transducer, it is driven by the ultrasound imaging platform developed in Chapter 2 for imaging wire phantoms and porcine blood vessels in vitro.

2.2 Methods

2.2.1 FZP Design

Fig. 2.3 illustrates the schematic of the designed catheter. In front of the matching layer of the proposed transducer, a FZP layer is positioned, and its parameters are calculated by the Fresnel principle, as follows:

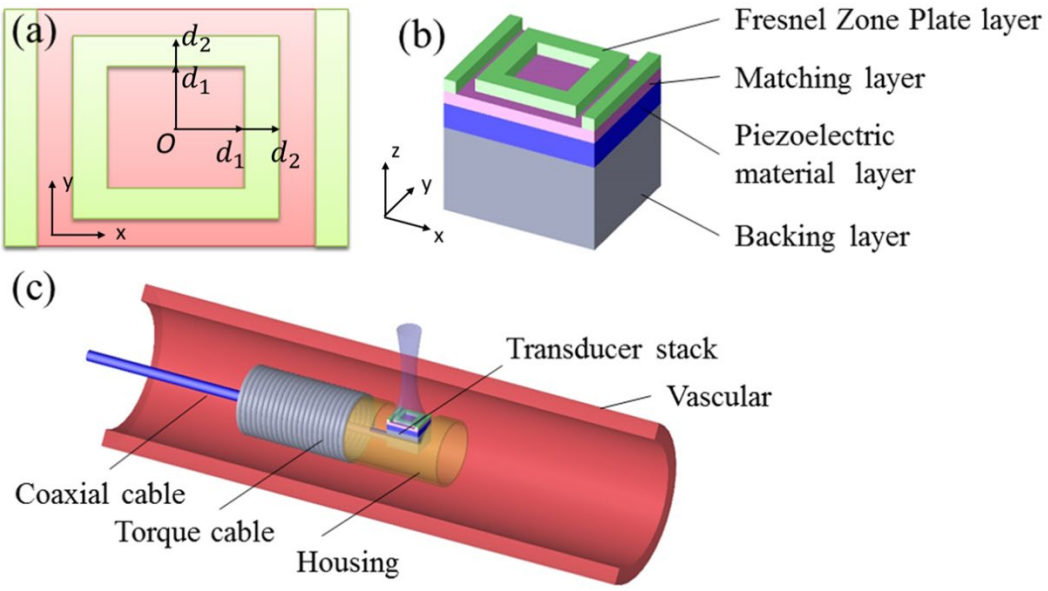

Fig. 2.3. Schematics of (a) the FZP layer, (b) transducer element, (c) FZP IVUS catheter.

In this study, the parameters of the Fresnel zone of the FZP transducer are calculated using the plane wave equation[104]:

$$d_n = 1/2[(d1 + d2 + n\lambda)^2 + \left(\frac{d_1^2 - d_2^2}{d_1 + d_2 + \frac{n\lambda}{2}}\right)^2 - 2(d_1^2 + d_2^2)]^{1/2} \quad (2\text{-}1)$$

In the case of plane wave incidence, where $d_1 \to \infty$, the focal length F is represented by d_2, and formula (3-1) can be simplified as:

$$d_n = \sqrt{n\lambda F + (\frac{n\lambda}{2})^2} \quad (2\text{-}2)$$

The width of each zone, d_n (n = 1, 2, …, N), is arranged from the center of the Fresnel zone, and N represents the zone number, and the focal length is denoted as F = 2 mm. The width of a zone (indicated by the green zones in Fig. 3.2) is $W_n = d_{2n}$-d_{2n-1}.

To achieve the desired focusing quality of the FZP transducer, it is necessary to have a phase difference of π between the FZP zones and grooves (indicated by the red zones Fig. 2.3). The phase difference Δφ was computed using the following equation:

$$\Delta\varphi = \frac{2\pi}{\lambda} \frac{|c_0 - c_1|}{c_1} t \quad (2\text{-}3)$$

Here, c_0 and c_1 represent the sound velocity of water and FZP layer material respectively, λ represents the wavelength of water and t denotes the thickness of FZP layer.

2.2.2 COMSOL Simulation

The finite element simulation is often used in calculations in the fields of fluid mechanics, structural mechanics, and electromagnetic mechanics. The main principle of finite element simulation is to discretize the unit in the continuous solution domain, and transform a continuous degrees of freedom (DOF) problem into a discrete finite DOF problem by solving an approximate function for each discrete unit. In this study, COMSOL software was utilized to simulate the acoustic beam of the transducer. The obtained results were used to optimize the transducer parameters accordingly. COMSOL simulation software provides a significant advantage through its capability to perform multi-physics coupling calculations. By utilizing the finite element calculation approach, the software can mathematically solve partial differential equations for both single and multi-physics scenarios, thus enabling the simulation of

real-life physical phenomena. The simulation steps are shown in Fig 2.4.

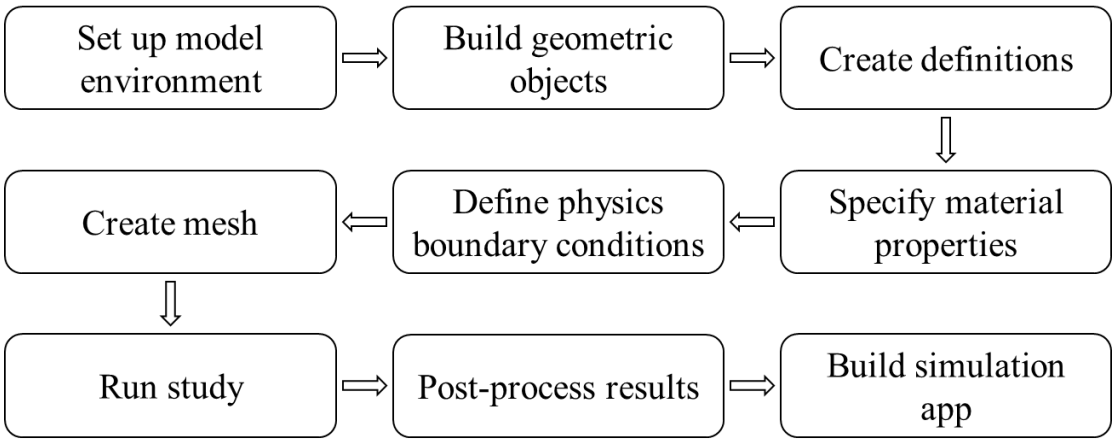

Fig. 2.4. The Comsol simulating workflow.

To construct a simulation model, it is necessary to select the pressure acoustics physical field and create the model. The selection of the simulation domain for the frequency domain field is determined by the calculation type being performed. Next, the transducer structure and simulation domain range and shape are drawn according to the actual parameters of the proposed transducer. We selected the piezoelectric material and sound pressure domain material parameters from the software material library. For the piezoelectric material, PZT-5H ceramic is used, and for the sound pressure domain material, Water is used. To mitigate reflections at the interface between the transducer and water, the inclusion of a matching layer is necessary. The design parameters of the FZP and planar transducer, which were optimized using simulation software, are provided in Table 2.1.

Table 2.1. Parameters of the planar and FZP transducer.

Parameter	FZP transducer	Planar transducer
Aperture (mm)	0.778×0.9	0.778×0.9
Piezo- material	PZT-5H	PZT-5H
Thickness (μm)	35	35
The material of 1st Matching layer	Ag/epoxy	Ag/epoxy
Thickness (μm)	10	10
The material of 2nd Matching layer	N/A	Parylene C
Thickness (μm)	N/A	12
FZP layer material	Ag/epoxy	N/A
hickness (μm)	8	N/A
Backing layer material	E-solder 3022	E-solder 3022
Thickness (μm)	300	300

To avoid sound wave reflection at the boundary, the piezoelectric material is added as the boundary load to serve as the excitation power of the transducer. The acoustic radiation boundary condition is set as the sound pressure domain boundary condition to accurately calculate the sound field distribution of the transducer. Proper grid division is performed on the entire calculation area to ensure accurate sound field distribution calculation, where the maximum size of the grid division is typically λ/6.

To conduct the calculation, appropriate analysis parameters are added, and the Fc of the transducer is set as the calculation parameter for the frequency domain field

simulation. After calculation, the corresponding drawing group is added according to the data that needs to be viewed by reading the calculation data.

2.2.3 Fabrication

3203HD ceramics (CTS Co., Tianjin, China) is chosen as the piezoelectric material for fabricating the transducer owing to its desirable characteristics. It possesses a high electromechanical coupling coefficient, a small particle size of ceramic powder, and exhibits stable performance when ground into ultra-thin sheets. These properties make it suitable for creating HFU transducers. Firstly, the sputtering machine (NSC-3500, NANO-MASTER Inc., TX, USA) was utilized to sputter Cr/Au electrodes onto one surface of the ceramic sample. The sputtering system can be seen in Fig. 2.5. Next, the electrode-plated surface of the wafer was bonded on the surface of a sapphire slice using wax. The slice, with the sample bonded to it, was then putted on a grinder for the grinding process, as illustrated in Fig. 2.6. The ceramic sample was ground down to a 35 μm thickness. Following the grinding process, Cr/Au electrodes were sputtered onto the ground surface of the sample.

Fig. 2.5. Magnetron sputtering system.

Epoxy (Insulcast 502, ITW Performance Polymers, Montgomeryville, USA) serves as the primary material for manufacturing both the matching and FZP layer. To create a conductive mixture with appropriate acoustic impedance, silver powder with a particle size of 2~3 μm (Sigma Aldrich, Burlington, USA) is mixed into the epoxy as filler. The prepared mixture was utilized to fabricate both the matching and FZP layer, which were subsequently deposited onto the surface of the ceramic sample. The deposited layer was then ground down to 18 μm. For planar transducer, the thickness is 10 μm. Finally, the sample was flipped and bonded to another sapphire plate. The backing material, which is conductive epoxy, was stacked on the other surface of the sample to serve backing layer and provide support and electrical conductivity.

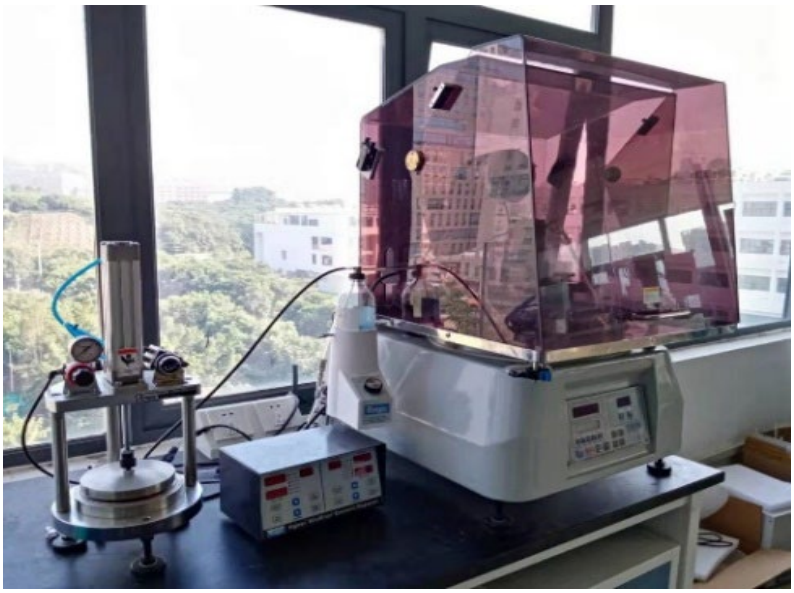

Fig. 2.6. Precision lap machine.

After grinding the backing material to the desired thickness, the sample is flipped over once again. The upper surface of the sample is then etched using a laser instrument to create grooves according to the designed size. This process completes the shaping of the FZP layer on the sample upper surface. After etching the grooves to a depth of 8 μm, the sample is divided into small piezo stacks with dimensions of 0.778×0.9 mm^2 using a dicing device (ADT 7122, ADT Co., Israel). The dicing machine is displayed in Fig. 2.7.

Fig. 2.7. Dicing machine.

Fig. 2.8(a) displays a representative piezoelectric stack. To link the positive and negative electrodes of the piezoelectric stack, three steps are involved. First, a conductive epoxy is used to connect the conductive backing layer to the signal wire of a coaxial cable. Next, the piezoelectric stack is mounted into a copper housing. The housing is also boned to the ground wire of the cable using conductive epoxy. In the final step, epoxy is used to fill the space between the piezoelectric stack and the housing, as shown in Fig. 2.8(b). Additionally, a Cr/Au layer is sputtered onto the surface of the copper housing and the matching layer of piezoelectric stack to establish an electrical connection between them.

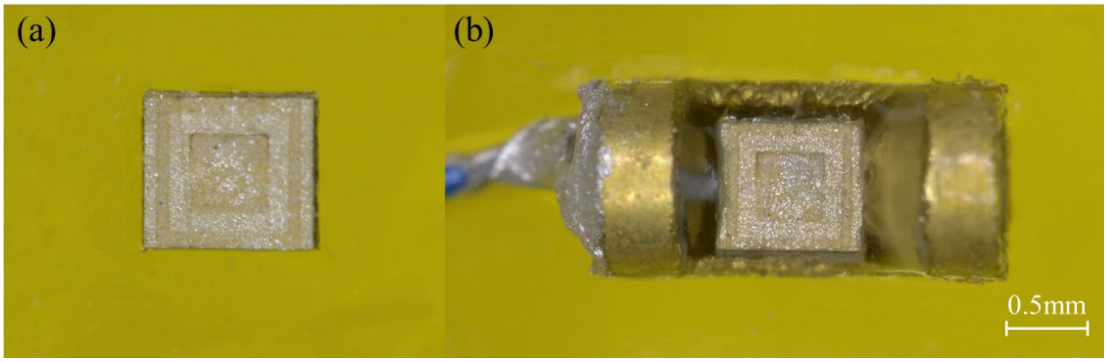

Fig. 2.8. Image of (a) a piezoelectric stack, (b) an assembled transducer.

2.2.4 Transducer Performance Characterization

The electrical performance of the FZP and planar transducer are measured using an impedance analyzer, as depicted in Fig. 2.9. A quartz reflector is positioned on front of the transducers. Both the reflector and the transducers are immersed in deionized water for pulse-echo test experiments. A pulser/receiver (UT340) is utilized to excite the transducer. The excitation pulse wave is set to a length of 2 ns with a voltage of 100 V. The received echo is displayed on a digital oscilloscope after a gain of 10 dB. The instrument setup is displayed in Fig. 2.10.

Fig. 2.9. Impedance analyzer.

Fig. 2.10. Pulse echo test platform.

2.2.5 Phantom and Ex Vivo Tissue Imaging

The imaging evaluation system is shown in Fig. 2. 11. A house made imaging platform, which can be found in our previous work, was used to drive the transducers[105]. The platform comprises integrated excitation pulse generation and data reception functions. The excitation pulses are amplified in two stages and then

passed through a customized power amplifier for high-voltage short or coded pulse output. The transducer is attached to a rotation device, enabling the easy acquisition of sectional images. An interactive interface based on Visual Studio 2013 (Microsoft Corporation, Redmond, WA) permits the easy configuration of ultrasound transmit and receive parameters, including pulse repeat frequency (PRF), depth, and frame rate, and supports real-time image display and raw data storage. Imaging software acts as an important bridge between the hardware platform and personal computer (PC). The parameters of the software interface are transmitted via USB 3.0 to the FPGA of the hardware platform, which subsequently analyzes the parameters sent by the software and configures them in the appropriate registers to control the ultrasound transceiver process.

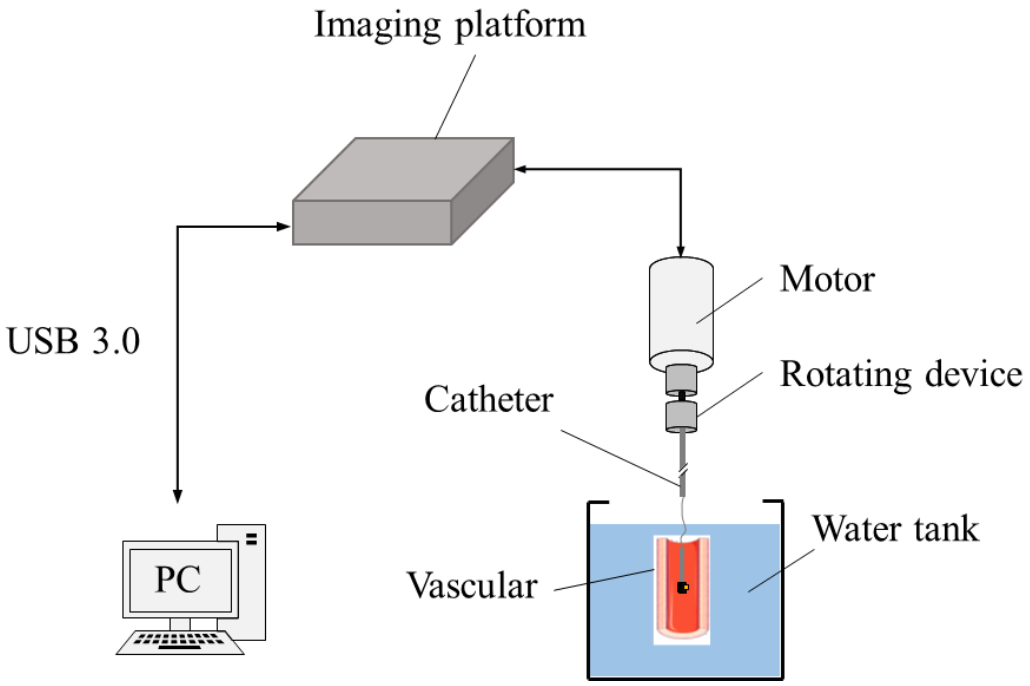

Fig. 2.11. Imaging evaluation system

The signal gain of the imaging platform is set to 35 dB for data acquisition. To evaluate the imaging quality of the transducers, a house-made wire phantom is used. The wire phantom is created by making a workpiece with a series of holes arranged in a regular pattern on concentric circles of varying radii. In this particular wire phantom, three tungsten wires (OD: 12.7 μm) are installed in the holes located on concentric circles with radii of 2, 3, and 4 mm, respectively. The wire phantom is illustrated in Fig. 2.12. The transducers were positioned at the central of the wire phantom to ensure accurate imaging and proper alignment. The transducer is equipped with a motor that allows it to rotate. During the acquisition process, the data will be collected and recorded by the imaging platform in real time. To further verify the tissue imaging quality of the planar and FZP transducers, a porcine blood vessel was isolated and prepared as a specimen.

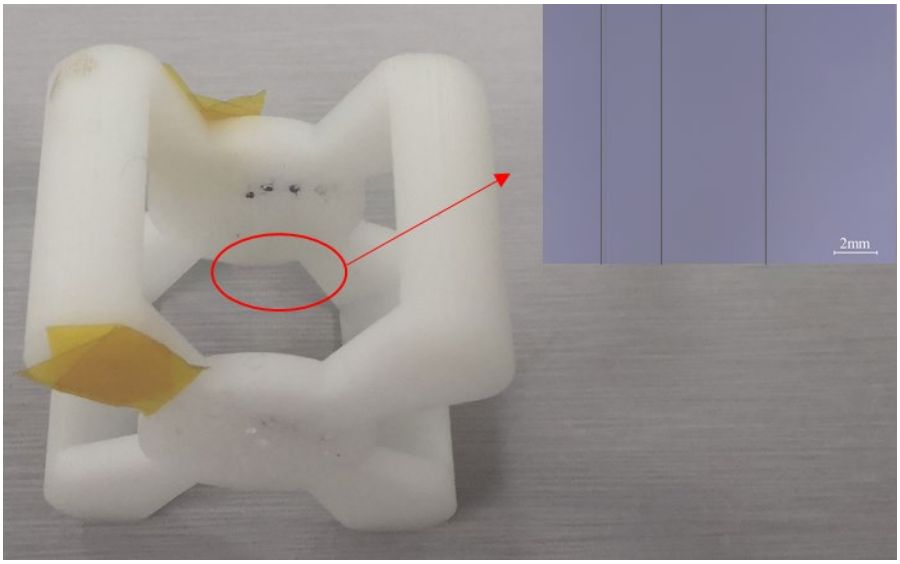

Fig. 2.12. Wire phantom.

2.3 Results

2.3.1 Simulation Results

The simulation results were acquired by the Comsol software. The simulated acoustic field of the transducer is demonstrated in Fig. 2.13. As depicted in Fig. 2.13(a), the planar transducer generates an acoustic field with a natural focus located at 7.5 mm, accompanied by side lobes exhibiting weaker sound pressure. Conversely, the FZP transducer produces an acoustic field with a focal point at 1.8 mm, as displayed in Fig.2.13 (b). Fig. 2.13(c) displays the signal amplitude distribution along the dashed line on the focal plane depicted in Fig. 2.13(a) and Fig. 2.13(b). It is evident that the FZP transducer exhibits a smaller FWHM at the focal point (FWHM = 0.0755 mm) compared to the planar transducer (FWHM = 0.3603 mm). Additionally, the side-lobe of the FZP transducer is narrower than that of the planar transducer, indicating a more focused and improved imaging performance.

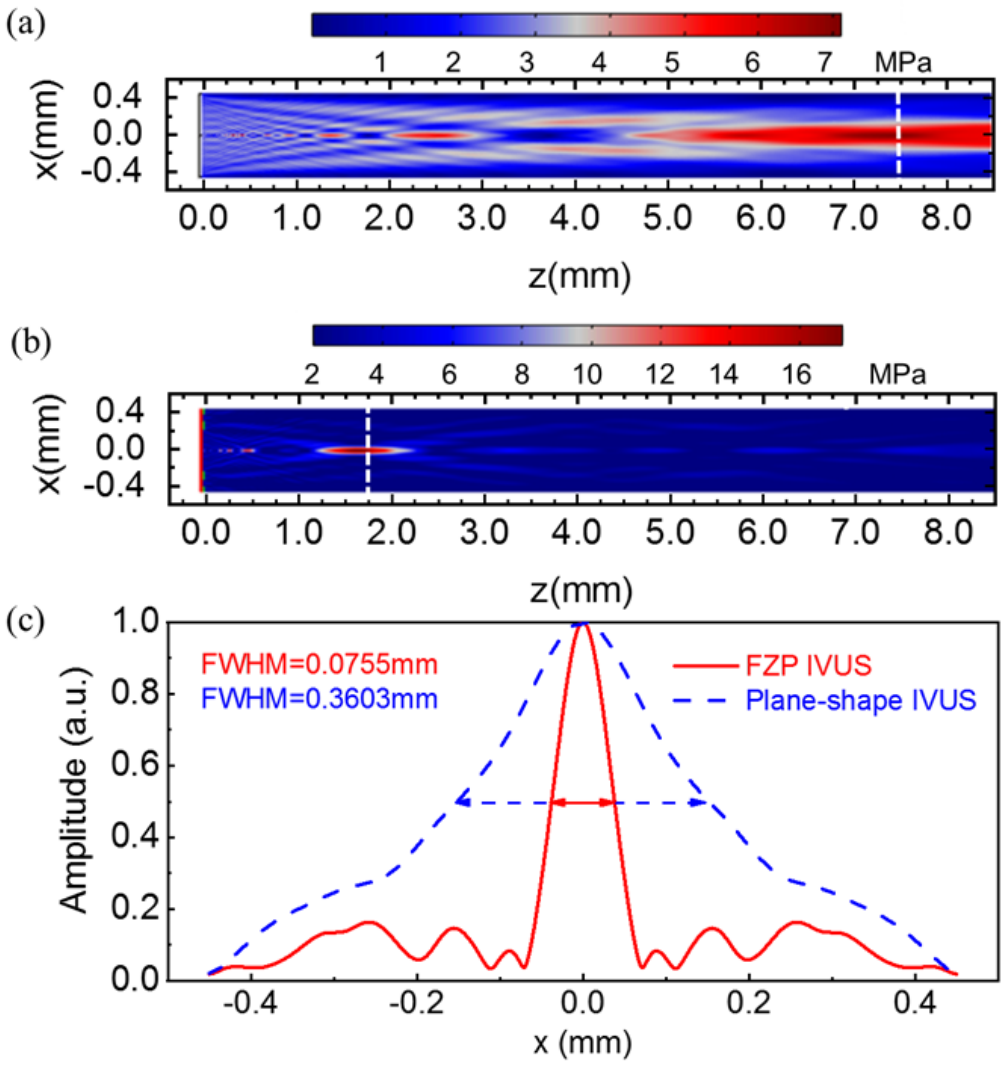

Fig. 2.13. The acoustic beams of (a) the planar and (b) FZP transducers. (c) The amplitude of the planar and FZP transducers.

The simulation results demonstrate the effective modulation of ultrasonic waves by the FZP layer integrated with the planar transducer. The comparison of the FWHM of the amplitude, computed for both the FZP transducer and the planar transducer, indicates that the FZP transducer is capable of achieving higher lateral imaging resolution compared to planar transducers. These findings highlight the potential of

FZP transducers for improving imaging resolution in various applications.

2.3.2 Electrical and Acoustic Performance

Fig. 2.14 (a) and (b) display the electrical performance of the FZP and planar transducers, including impedance and phase curves. The curves display that the FZP transducer has a resonant frequency of 57.3 MHz, with an impedance of 10.3 Ω at that frequency. Similarly, the planar transducer exhibits a resonance frequency of 56.3 MHz, with an impedance of 4.5 Ω at that frequency. These results demonstrate that both transducer types yield comparable outcomes, indicating that the FZP layer attachment affects the transducer's electrical impedance to a limited extent.

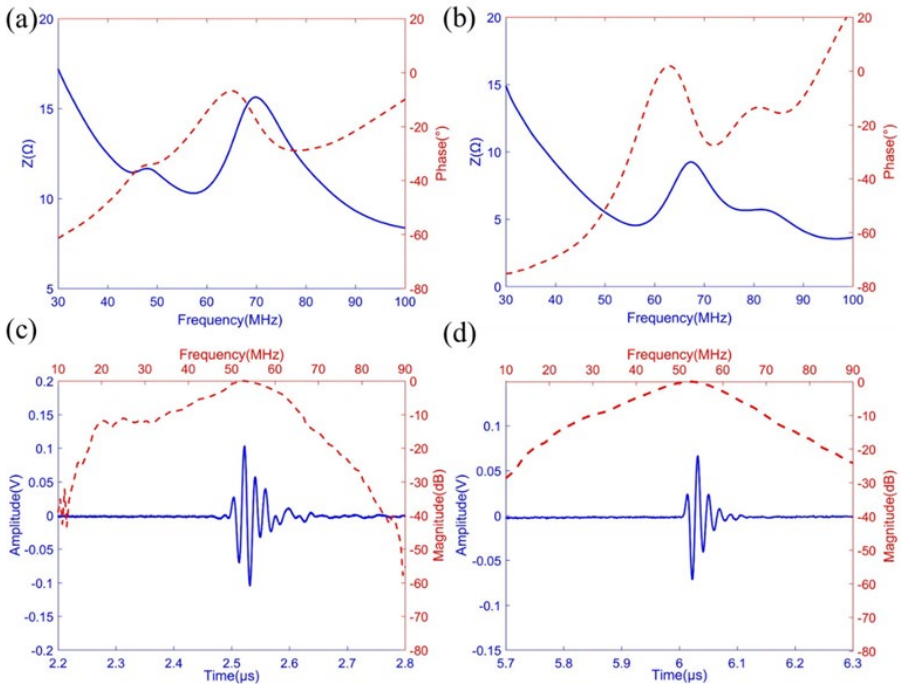

Fig. 2.14. Impedance and phase curves of the (a) FZP and (b) planar transducers. Pulse echo and spectrum curves of the (c) FZP and (d) planar transducer.

The echo received by the FZP and planar transducers were displayed and recorded by an oscilloscope, as depicted in Fig. 2.14 (c) and (d). The FZP transducer has an Fc of 52.5 MHz and a -6 dB BW of 42%. In contrast, the planar transducer has an Fc of 51.3 MHz and a -6 dB BW of 58%. The performance of FZP and planar transducers are shown in Table 2.2. The results show that the -6 dB BW of the FZP transducer is inferior to that of the planar transducer. This is mainly due to the weakening caused by the FZP layer and the absence of a second matching layer.

Table 2.2. The performance of FZP and planar transducers

	FZP transducer	Planar transducer
Resonant frequency (F_r)	57.3 MHz	56.3 MHz
Impedance at F_r	10.3 Ω	4.5 Ω
Center frequency (F_c)	52.5 MHz	51.3 MHz
-6 dB bandwidth	42 %	58 %
Axial resolution	47 μm	44 μm
Lateral resolution	184 μm	314 μm
SNR	37.2 dB	33.9 dB

2.3.3 Imaging Measurement

The wire phantom ultrasound images were reconstructed using Matlab software (MathWorks Inc., Natick, USA), and the imaging resolution was analyzed and calculated by the software. An ultrasound image of the wire phantom acquired with the planar transducer is depicted in Fig. 2.15(a). The axial beam profile of the planar transducer is depicted in Fig. 2.15(b), while the lateral beam profile is depicted in Fig. 2.15(c). The planar transducer achieved axial and lateral resolutions of 44 μm and 314 μm respectively.

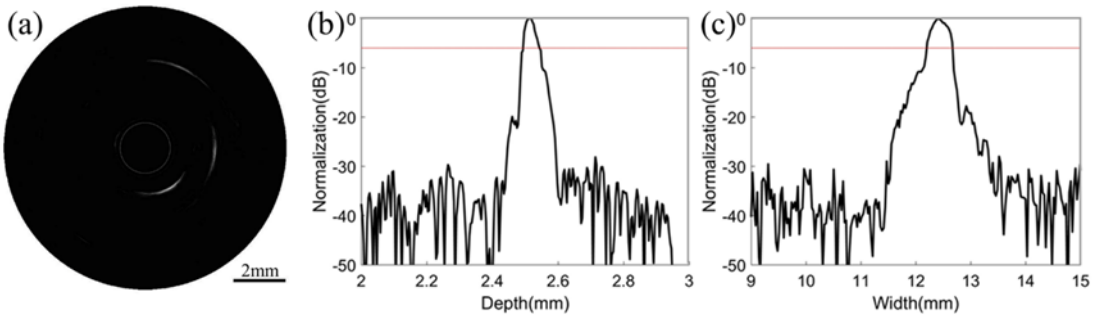

Fig. 2.15. (a) A wire phantom ultrasound image of the planar transducer. (b) Axial and (c) lateral beam profiles of the ultrasound image. In both (b) and (c), the red lines indicate the -6 dB magnitude.

Fig. 2.16(a) displays an ultrasound image of the wire phantom obtained using the FZP transducer. The axial beam profile of the FZP transducer is depicted in Fig. 2.16 (b), while the beam profile is depicted in Fig. 2.16(c). The FZP transducer achieved axial and lateral resolutions of 47 μm and 184 μm respectively.

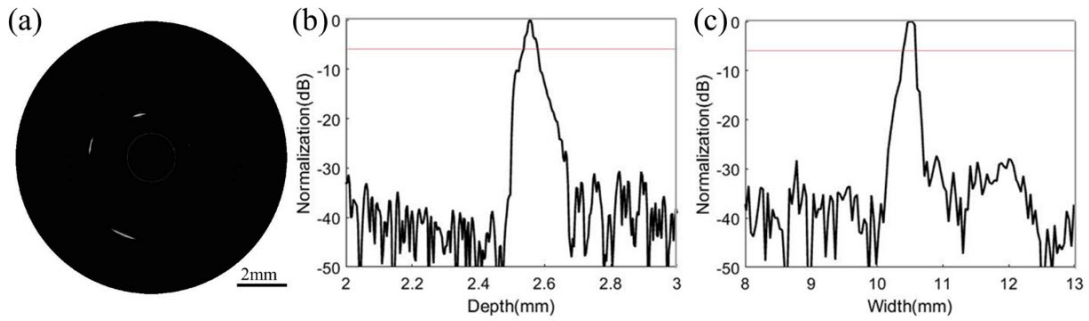

Fig. 2.16. (a) A wire phantom ultrasound image of the FZP transducer. (b) Axial and (c) lateral profiles of the ultrasound image. In both (b) and (c), the red lines indicate the -6 dB magnitude.

To calculate the SNR, one can subtract the average background noise from the magnitude of the largest signal obtained from the image. The FZP transducer exhibited an SNR of 37.2 dB, while the planar transducer had an SNR of 33.9 dB. The FZP transducer exhibits a higher SNR, indicating its superior imaging capability compared to the planar transducer.

Ultrasound imaging was conducted on an ex vivo porcine artery using both FZP and planar transducers. The obtained ultrasound images are presented in Fig. 2.17. In the FZP transducer ultrasound image, there is clearer distinguishable between the blood vessel wall and fatty tissue, indicating improved distinguishability compared to the planar transducer images.

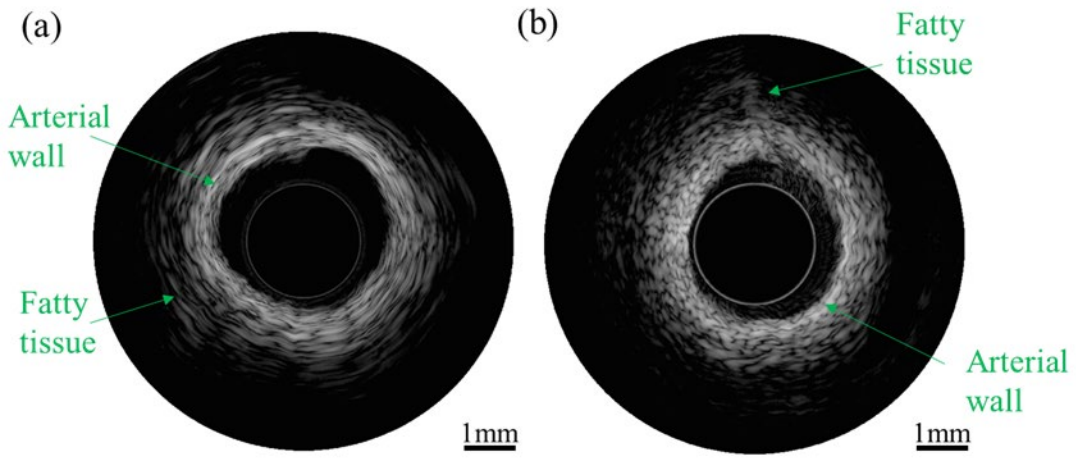

Fig. 2.17. Ultrasound images of a swine artery acquired by the (a) FZP and (b) planar transducers.

2.4 Discussion

IVUS imaging is a crucial diagnostic tool for detecting AP. However, the conventional IVUS catheters suffer from limitations in terms of poor lateral resolution, which restricts their applications. To address this issue, a HFU transducer incorporating an FZP layer is developed to enhance the lateral imaging resolution of IVUS. The acoustic beams of the FZP transducer, along with a planar transducer of identical dimensions, were simulated using COMSOL. In the proposed FZP transducer, the focal spot is obviously decreased compared to the planar transducer. However, due to the second matching layer is replaced by the FZP layer, the -6 dB BW of the FZP transducer (42%) is inferior to that of the planar transducer (58%). Consequently, the axial resolution of FZP transducer presents a slightly worse axial resolution than that of the planar transducer. On the other hand, the imaging of the wire phantom and their beam profiles indicate that the FZP layer effectively improves the lateral imaging resolution of the

transducer.

Chapter 3 Geometrically Focused IVUS Transducer using PIN-PSN-PT Ceramics

3.1 Introduction

Atherosclerosis (AS) contributes significantly to the growth of large number of CADs, including stroke and ischemic cardiomyopathy[3]. In the advanced stages of AS, atherosclerotic plaque (AP) formation occurs. Some plaques are classified as vulnerable, and a plaque rupture will cause severe conditions, such as angina pectoris and other ACS[10]. Thus, the development of a imaging technology with high resolution that can identify vulnerable plaques, accurately characterize coronary AS patterns, and monitor morphological changes in plaques after intensive drug therapy holds significant clinical implications[106].

The IVUS catheter is a minimally invasive diagnostic technology that offers high resolution, thereby enabling clear differentiation between the arterial wall and lumen. It effectively detects various plaque morphologies, such as fiber, fibrous fat, calcification, and necrosis. In addition, IVUS provides the measurements of artery size; lumen zone; and the depth, extent, and profile of calcification, making it an indispensable diagnostic tool for assessing arterial vascular lesions[107]. Regarding the treatment of vulnerable plaques, one safe and effective method involves the deployment of a stent within the artery stenosis. IVUS is a crucial character in guiding the clinician in determining the

appropriate size and location for stent placement. Moreover, IVUS facilitates the postsurgical assessment of the stent's fit and overall performance[108].

In Chapter 2, our research focused on the design and fabrication of an FZP layer to enhance the lateral imaging resolution of IVUS by effectively focusing the acoustic beam. However, there was a challenge due to the mismatch in electrical impedance between the transducer, which was fabricated using PZT-5H ceramic and had a size of 0.9 × 0.778 mm (resulting in an impedance of approximately 10 Ω), and the imaging platform, which had an impedance of 50 Ω. This impedance mismatch can have a passive effect on the imaging quality of IVUS. Lee et al.[85] reported on a focused IVUS transducer with element sizes of 0.5 × 1 mm. However, this transducer only focused in one direction, which means that its elements had a cylindrical surface rather than a spherical surface, consequently weakening the focusing effect of the transducer. Another IVUS transducer proposed by Chen et al.[82] featured geometrical focus on the upper surface only, whereas the lower surface remains planar, resulting in suboptimal focusing capabilities. Jian et al.[84] developed a geometric focusing transducer; however, its electrical impedance was relatively low (approximately 10 Ω). This low impedance can lead to certain disadvantages, such as decreased insertion loss (IL), in the transducer.

In this study, a geometrically focused IVUS transducer that utilizes PIN-PSN-PT piezoelectric ceramics was proposed. The choice of PIN-PSN-PT ceramics was based

on its favorable dielectric constant, which enables a sufficient match of electrical impedance between the transducer and imaging platform. This impedance match is crucial for enhancing the sensitivity of IVUS imaging.

3.2 Field II Simulation

Field II, a comprehensive and flexible software, is used in the field of medical ultrasound research for its ability to simulate complex ultrasound scenarios and accurately model ultrasound wave propagation. These capabilities make it an indispensable tool for studying, optimizing, and advancing ultrasound imaging technologies[109-111].

3.2.1 Acoustic Field Simulation

We simulated the acoustic beam of transducers with different geometries using the Field II program. Fig. 3.1(a) schematically shows the geometry of the focal IVUS transducer. The focal length of the transducers is designed at 2.25 mm. The geometric focus is situated at the center of the sphere, whereas the acoustic focus is located at the position with the highest amplitude of the acoustic field. The acoustic focal depth is usually smaller than the geometric focal depth. Figs. 3.1(b) and (c) illustrate the acoustic field of the planar and focused transducers with an aperture of 0.3 mm. It is evident that the beam profiles of the acoustic field for both transducers rapidly diverge after the acoustic focus, and the focusing has minimal impact on the beam

pattern as the geometric focal depth surpasses the natural focal depth. However, when the aperture is increased to 0.6 mm, the effect of focusing becomes prominent, resulting in intensified intensity at the acoustic focus (illustrated in Figs. 3.1 (d) and (e)). Furthermore, the acoustic focal depth of the focused transducer is smaller than that of the planar transducer owing to the focusing effect.

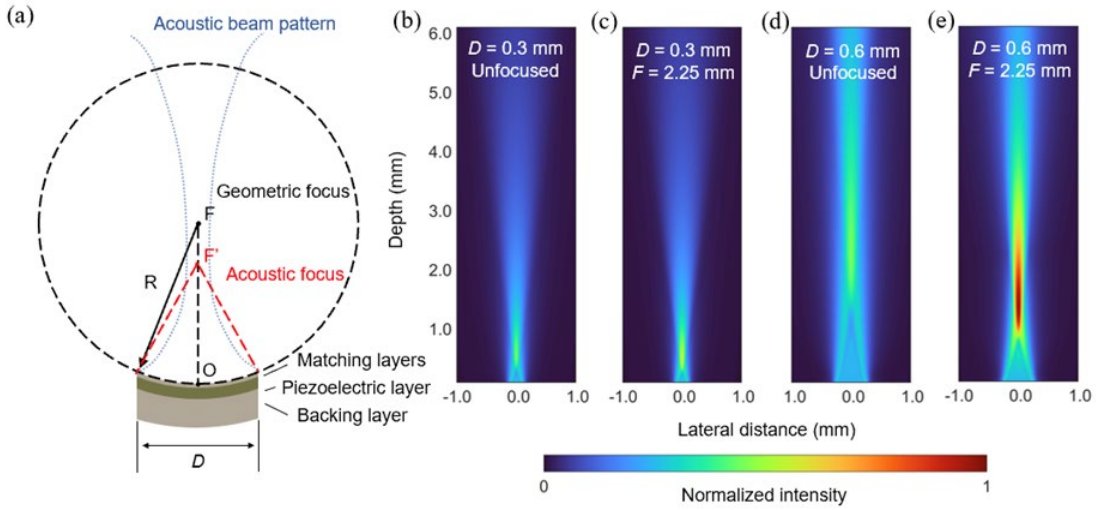

Fig. 3.1. (a) Diagram of the focused IVUS transducer. Simulated acoustic field of (b) 0.3-mm planar (unfocused) transducer, (c) 0.3-mm focused transducer, (d) 0.6-mm planar transducer, and (e) 0.6-mm focused transducer.

The −6 dB beam width is a commonly used parameter to depict the main lobe width of the beam pattern produced by an acoustic transducer. The lateral imaging resolution is depending on the beam width of the acoustic field. A smaller −6 dB beam width indicates a narrower main lobe and better lateral resolution, enabling the system to resolve smaller details and separate closely spaced reflectors more

accurately. The −6 dB beam widths of the acoustic field for transducers with different geometries were included in this study.

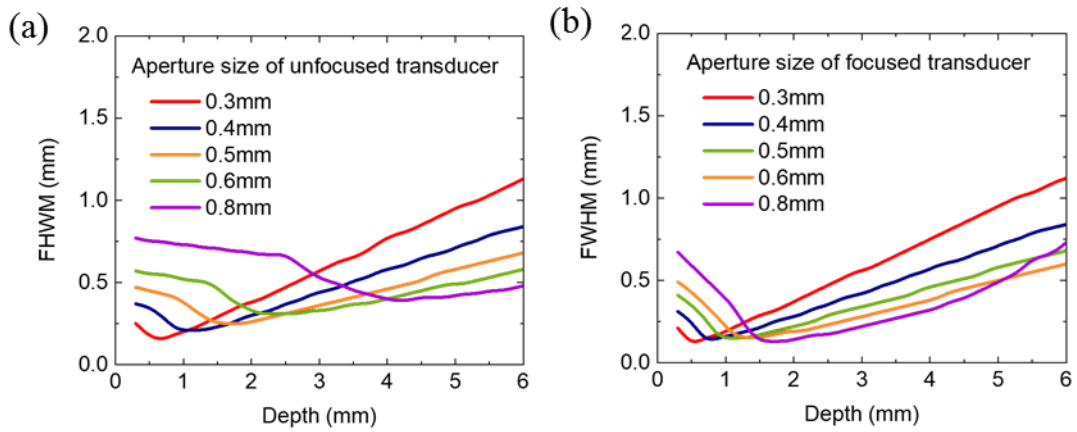

Fig. 3.2. A −6 dB beam width with respect to depth for the (a) planar and (b) focal transducers with different aperture size.

Figs. 3.2(a) and (b) depict the relationship between the beam width and depth of several planar and focused transducers with different aperture sizes. For the planar transducer, the minimum beam width is attained at the natural focal depth. It is noteworthy that the beam width is directly in proportion to the square of the aperture size, which means that as the size of aperture expands, the beam width also increases, resulting in a worse lateral imaging resolution. Meanwhile, the focal transducer beam width is influenced by the focusing effect and the beam width at the acoustic focus is narrower, indicating improved lateral resolution. Furthermore, the effect of focusing becomes more significant as the aperture size increases, strengthening the intensity at the acoustic focus and further enhancing the lateral imaging resolution. Overall, the

comparison of beam widths demonstrated that the focusing technique could have a substantial impact on the lateral imaging resolution of transducers, particularly for larger aperture sizes.

3.2.2 Ultrasonic Imaging Simulation

We conducted wire-imaging simulations to assess the spatial resolution of planar and focused transducers with varying apertures. The imaging method was arranged as horizontal scanning, and there were 1500 scan lines along the horizontal direction. Transducers with an aperture of 0.3 and 0.6 mm were simulated, respectively. The Fc of these transducers was set at 40 MHz and the focal length of all focal transducers was 2.25 mm. Five wires were arranged in the front of the transducer in a sequential manner, each located distance 1 mm from the previous wire and starting 1 mm away from the transducer. The simulation imaging area covered a region of 6 × 6.5 mm. The resulting simulated ultrasonic images are presented in Fig. 3.3.

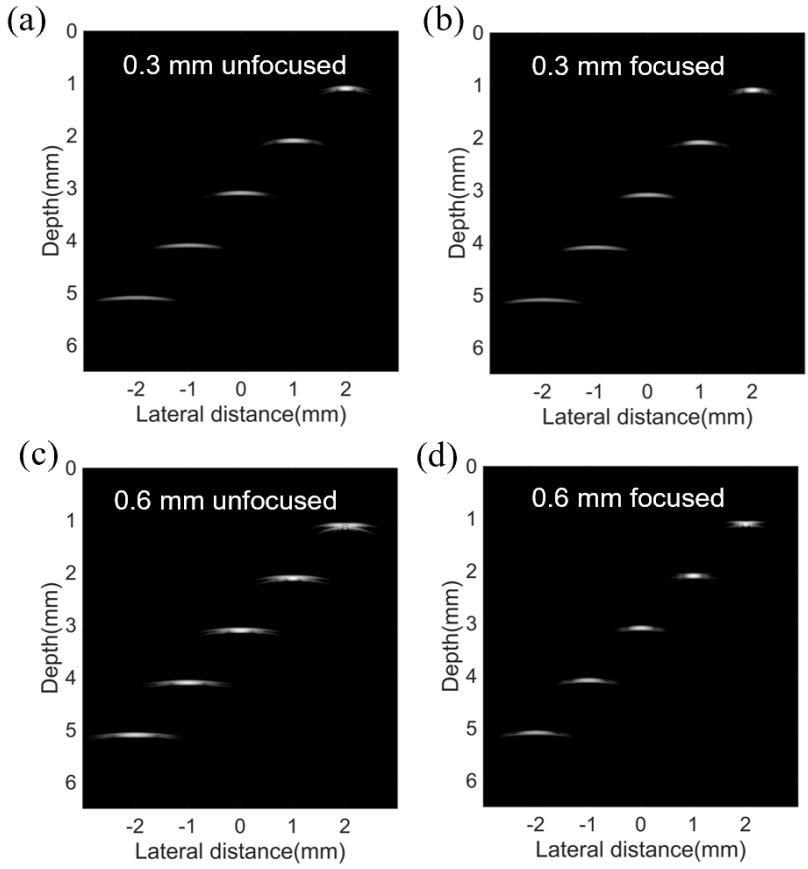

Fig. 3.3. Ultrasonic imaging simulations of (a) 0.3-mm planar transducer, (b) 0.3-mm focused transducer, (c) 0.6-mm planar transducer, and (d) 0.6-mm focused transducer.

We also calculated the axial and lateral imaging resolutions of the transducers at different locations, as outlined in Table 3.1. The axial resolutions of focused transducers were similar to those of unfocused transducers with the same apertures. However, significant improvements in lateral resolution were observed with focusing. Moreover, transducers with larger apertures exhibited greater improvements in the lateral resolution. Of note, the natural focus lengths for transducers with the aperture sizes of 0.3 × 0.3 mm and 0.6 × 0.6 mm were 0.6 and 2.4 mm, respectively.

Consequently, the lateral imaging resolutions of unfocused transducers with a 0.3-mm aperture decreased as the imaging depth improved. By contrast, the lateral imaging resolutions of unfocused transducers with a 0.6-mm aperture initially increased before reaching the optimal resolution at 2.4 mm.

Table 3.1. Axial and lateral resolutions of different transducers at different locations.

Resolution type	Transducers' type	Aperture (mm)	Wire location (mm)				
			1	2	3	4	5
Axial resolution (μm)	Unfocused	0.3	41.2	40.9	40.7	40.0	41.7
		0.6	42.3	43.8	41.8	41.2	41.0
	Focused	0.3	40.9	40.4	40.9	41.7	41.5
		0.6	45.4	40.6	40.9	41.0	41.5
Lateral resolution (μm)	Unfocused	0.3	143.2	273.5	388.2	493.3	633.7
		0.6	320.7	158.0	218.4	283.0	353.3
	Focused	0.3	137.9	262.9	378.4	503.5	603.3
		0.6	82.8	139.1	203.1	273.1	328.6

3.3 Materials and Methods

3.3.1 Preparation of High-Performance Textured PIN-PSN-PT Ceramics

The textured PIN-PSN-PT ceramics were produced via the conventional templated grain-growth method using the 0.19PIN-0.445PSN-0.365PT powder and 2.5 vol.% <001>-oriented BaTiO3 (BT) templates, as described earlier[112]. The microstructure of the ceramics was characterized using FE-SEM and XRD (Smart Lab, Japan), and a quasi-static d_{33} meter was used to measure the piezoelectric coefficient of the ceramics. The measurement of the material's permittivity was performed using an LCR meter

(E4980A, Agilent, USA) at a frequency of 1 kHz. All measurements were performed using a program-controlled furnace. The coercive field (EC) was obtained from the polarization-electric (P-E) field hysteresis loop, which was plotted operating a ferroelectric testing system. The longitudinal sound velocity and k_t in the thickness mode of the ceramics were calculated using the methods specified by the IEEE standards[113]. The clamped dielectric constant ($\varepsilon^S_{33}/\varepsilon_0$) was calculated by measuring the capacitance at twice the anti-resonant frequency using a precision impedance analyzer (HP4294A, Agilent, USA).

3.3.2 Fabrication of the Focused IVUS Transducer

Fig. 3.4(a) illustrates the schematic of the focused IVUS catheter, which comprised the focused acoustic stack, brass housing, torque coil, and coaxial cable. The fabrication of the acoustic stack followed the conventional technique described by Cannata et al.[114]. According to the properties of the textured PIN-PSN-PT ceramics, the structural parameters of the acoustic stack were optimized using a simulation software (PiezoCAD, Sonic Concepts, USA). The ceramics were lapped to 38 μm thick. Cr/Au electrodes (thickness: 50/150 nm) were deposited onto the both surfaces of the ceramics via DC magnetron sputtering (NSC-3500, NANO-MASTER, USA). The first matching layer was fabricated by blending epoxy with silver powder and then casting it onto the negative electrode of the ceramics. The material was subsequently lapped to 10 μm thick according to the design specifications. Some of conductive epoxy was laid on

the positive side of the ceramics to serve as the backing material. The acoustic stack comprised the Ag-epoxy layer and piezo-ceramic wafer, and conductive layer was then ground to a final thickness of 350 μm and diced into 0.6 × 0.6 mm pieces.

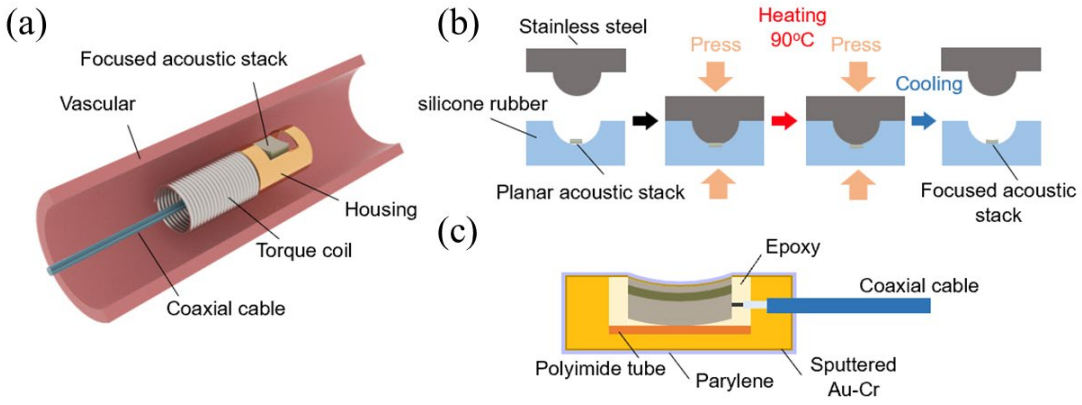

Fig. 3.4. (a) Schematic diagram of focused IVUS catheter. (b) Fabrication of focused acoustic stack using the press-focusing technique. (c) Cross section of the focused IVUS transducer.

The press-focusing technique was employed to achieve a spherical shape for the acoustic stack (Fig. 3.4(b)). The planar acoustic stack was placed into a soft silicone rubber mold and was compressed using a stainless-steel cover with a 4.5-mm diameter ball, which was conformal with the soft mold. The entire assembly, comprising the stack, mold, and cover, was heated to 90°C and maintained for 30 min. This process resulted in the formation of a spherical-focused shape, with the geometric focus located at 2.25 mm.

Fig. 3.5. Parylene deposition system.

The assembly of the acoustic stacks into the catheters involved the following steps. First, the signal wire of a 50-Ω micro-coaxial cable (48AWG, Hitachi Metals, Japan) was bonded to the acoustic stack connective-backing layer. Next, the acoustic stack and ground wire were affixed to a brass housing using instant adhesive (Super Glue, 3M, China) and conductive adhesive, respectively. A polyimide tube was inserted between the stack and housing to provide electrical insulation. The remaining space within the housing was filled using epoxy. A Cr/Au layer was fabricated to electrical connected the housing with the matching layer of the piezoelectric stack to establish an electrical

connection between them. Finally, the catheter was placed in a vapor deposition system (P6, Diener, Germany), and parylene C powder was evaporated in the system and deposited on the catheter's surface. The parylene deposition system is shown in Fig. 3.5. This layer is not only a second matching layer, but also provided waterproof protection. Fig. 3.4(c) provides a schematic representation of the longitudinal-section view of the IVUS catheter structure. Figs. 3.6(a) and (b) display the assembled focused and planar acoustic stacks within the brass housings, respectively, and Fig. 3.6(c) is a photograph of the developed focused IVUS catheter with the torque coil.

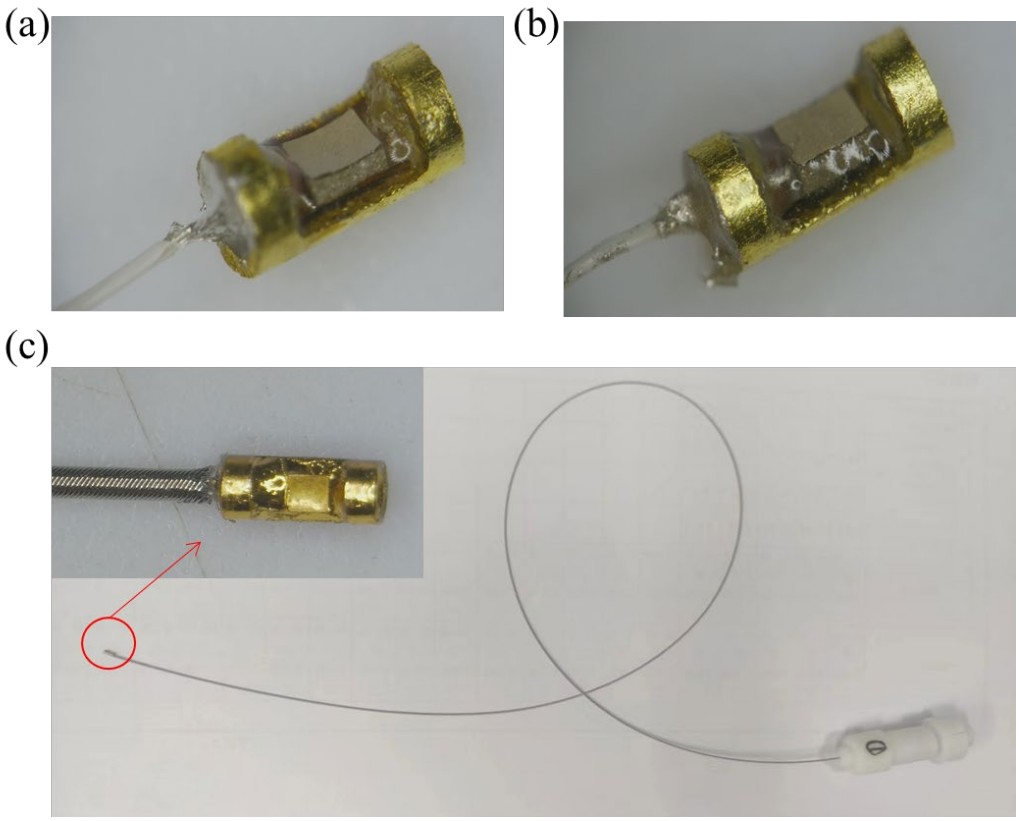

Fig. 3.6. Photographs of the (a) focused and (b) planar IVUS transducer. (c) Photograph of the as-developed focused IVUS catheter.

3.3.3 Transducer Characterization

The electrical impedance curves of the focused and planar transducers were obtained using a precision impedance analyzer. An ordinary pulse-echo test was executed to characterize the impulse response, Fc, and BW of the focused and planar transducers. The transducer was submerged in deionized water and connected to an ultrasonic pulser/receiver (DPR500, JSR Ultrasonics, USA), and a 3 μJ energy negative pulse was applied on the transducer for transmitting. So as to obtain the echo signal with maximum amplitude reflected from a polished quartz target, the adjustment of the position and emit angle of the transducer was performed using a multi-axis moving stage. The received signal of echo was finally displayed on a oscilloscope. The frequency response was then computed using FFT analysis performed by the oscilloscope.

3.3.4 Imaging Evaluations

A house made wire phantom was fabricated in this study for measuring the imaging resolution of the IVUS transducers. Three tungsten wires (OD: 10 μm) were securely placed in the phantom at the depths of 2, 3, and 4 mm. In addition, the imaging capability evaluation of transducers was performed by employing a swine coronary artery.

In the imaging procedure, both the phantom and artery sample were immersed in

deionized water. At the center of these objects, the transducers were positioned ready for imaging. To obtain real-time IVUS images, a servomotor operating at 20 rotations per minute (r.p.m.) was utilized to rotate the IVUS transducer through the torque coil. The transducer was connected to the ultrasonic imaging platform via a slip ring and coaxial cable. Chapter 2 provides additional details regarding the imaging platform as well as the data acquisition and processing methods.

3.4 Results

3.4.1 Properties of Textured PIN-PSN-PT Ceramics

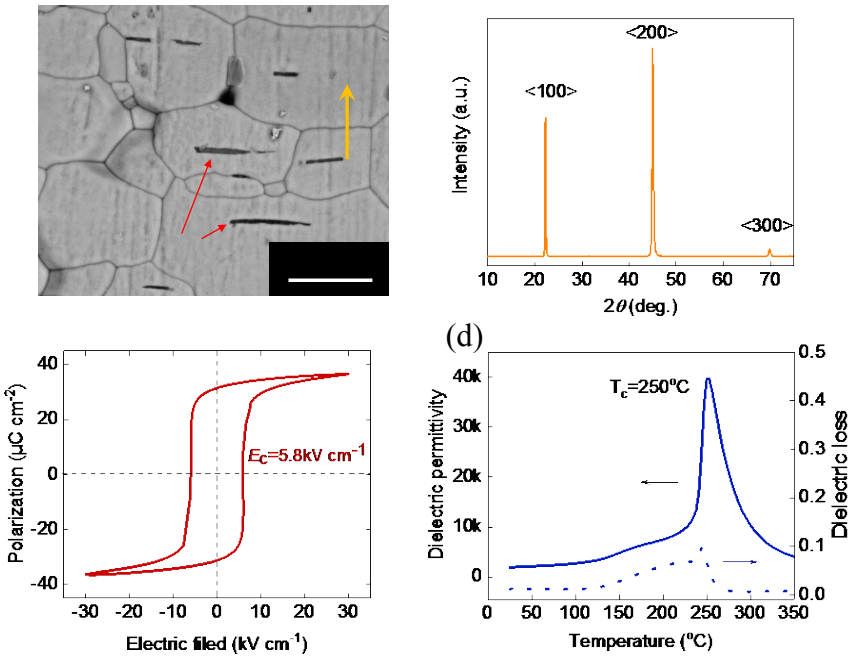

Fig. 3.7. Characterization of the textured PIN-PSN-PT ceramics. (a) SEM image of the fracture surface, (b) XRD pattern, (c) P-E loop, and (d) dielectric constant at 1 kHz. The red arrows in (a) indicate the <001>-oriented BT template seeds in the crystalline grains.

Figs. 3.7 (a) and (b) depict the microstructure of the textured PIN-PSN-PT ceramics as characterized via SEM and XRD. In the SEM image (Fig. 3.7 (a)), the crystalline grains were observed to grow along the [001] direction with the guidance of <001>-oriented BT templates, indicated by the red arrows. The XRD pattern (Fig. 3.7(b)) revealed only the presence of the characteristic <001> peaks of the perovskite structure, confirming the <001> orientation of the textured PIN-PSN-PT ceramics.

Fig. 3.7(c) and (d) present the P-E field hysteresis loop and permittivity of the textured PIN-PSN-PT ceramics, respectively. The coercive field (Ec) was 5.8 kV/cm, whereas the Curie temperature (TC) was 250°C. These values are higher than those of relaxor-PbTiO3 crystals (phase transition temperature Tr-t < 130 °C, Ec < 4.5 kV cm−1).

For comparison, Table 3.2 summarizes the main characteristics of the textured PIN-PSN-PT ceramics and commonly used piezoelectric materials for IVUS transducers. Of note, the textured PIN-PSN-PT ceramics presented a d_{33} of 900 pC/N and k_t of 0.60, which are similar to those of the advanced relaxor-PbTiO3 crystals. This performance can be attributed to the [001]-oriented growth of crystalline grains. Furthermore, the textured PIN-PSN-PT ceramics demonstrated excellent temperature and electric field stability, making them resistant to depolarization during transducer fabrication (such as hot press-focusing) and the ultrasonic imaging process.

Of particular importance, the clamped permittivity of the textured PIN-PSN-PT

ceramics was lower than that of relaxor-PT single crystals and other piezoelectric ceramics used in previous studies[115, 116]. This characteristic is advantageous for focused IVUS transducers, considering the requirement of 50-Ω electrical impedance matching.

Table 3.2. Characteristics of some piezoelectric materials commonly used in IVUS transducers [115-117].

Materials	Piezoelectric coefficient (pC/N)	Relative clamped permittivity $\varepsilon^s/\varepsilon_0$	Electromechanical coupling coefficient k_t	Longitudinal velocity vl (m/s)	Density ρ (kg/m^3)
PMN-PT single crystal	1400	850	0.58	4600	8000
PIN-PMN-PT single crystal	1450	780	0.58	4450	8180
$LiNbO_3$ single crystal	100	39	0.34	7340	4700
PZT-5H ceramic	593	1470	0.51	4590	7500
Sm-PMN-PT ceramic	1000	3000	0.54	4450	7690
Textured PIN-PSN-PT ceramic (This work)	900	440	0.60	4480	7650

3.4.2 Characterization of the textured PIN-PSN-PT-based IVUS Transducers

Figs. 3.8(a) and (b) present the frequency-dependent electrical impedance measurements of acoustic stacks before and after being shaped by pressing,

respectively. The impedance values of both the planar and focused stacks fell within the range of 32–62 Ω, satisfying the requirement of 50-Ω electrical matching. Of note, the resonance peaks were highly damped after the pressing process. This damping effect can be attributed to the residual stress generated during the high-temperature press-focusing process, which occurs at approximately 90°C. The presence of residual stress increases the mechanical loss within the acoustic stack, leading to a reduced mechanical quality factor. Figs. 3.8(c) and (d) show the measured impedance of the planar and focused IVUS transducers after encapsulating into the IVUS catheters. The impedance spectra exhibited three resonance peaks because of the parylene coating, which serves as the second matching layer. In addition, the impedance values were reduced by approximately half owing to the effect of the 50-Ω micro-coaxial cable.

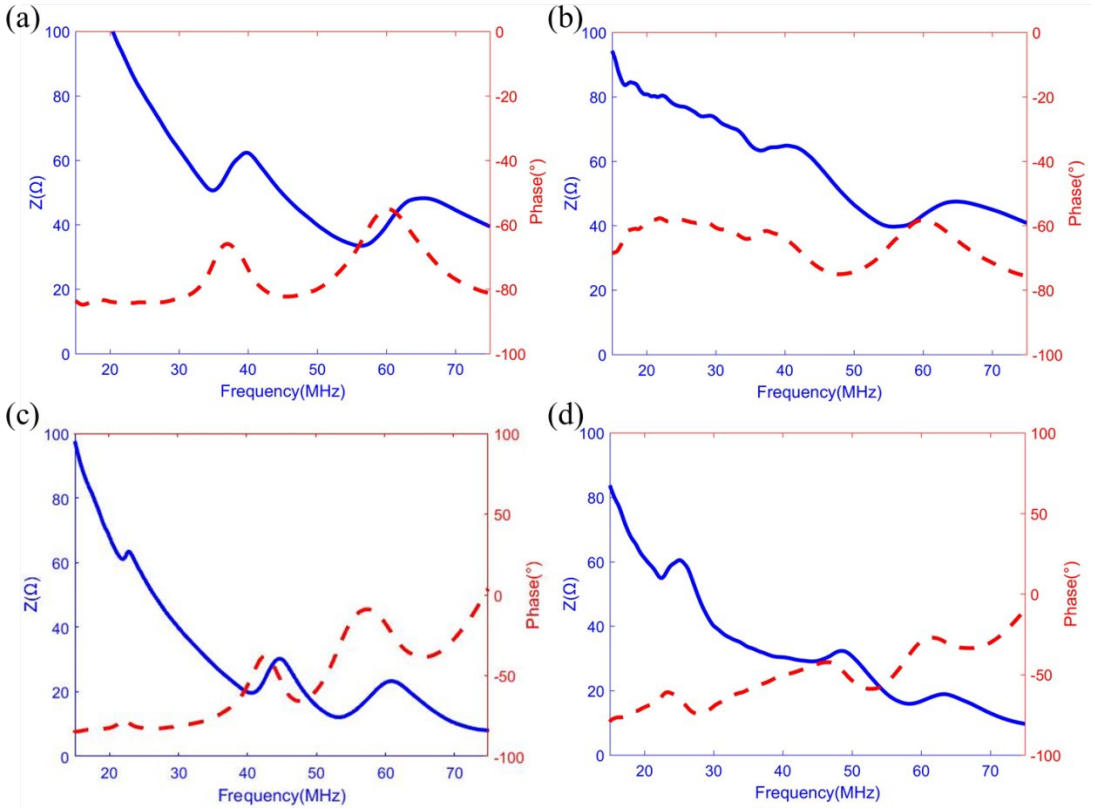

Fig. 3.8. Impedance (blue) and phase angle (red) of the textured PIN-PSN-PT-based transducers. (a) Planar acoustic stack, (b) focused IVUS acoustic stack, (c) planar IVUS transducer, and (d) focused IVUS transducer.

Figs. 3.9(a) and (b) present the echo responses and normalized spectrum for the planar and focused IVUS transducers, respectively. The peak-to-peak voltages (V_{pp}) of the unamplified echo signals were 1.8 V for the planar IVUS transducer and 1.9 V for the focused IVUS transducer. The focused transducer has higher echo amplitude attributed to the focusing effect, which enhances the ultrasound energy at the focal point.

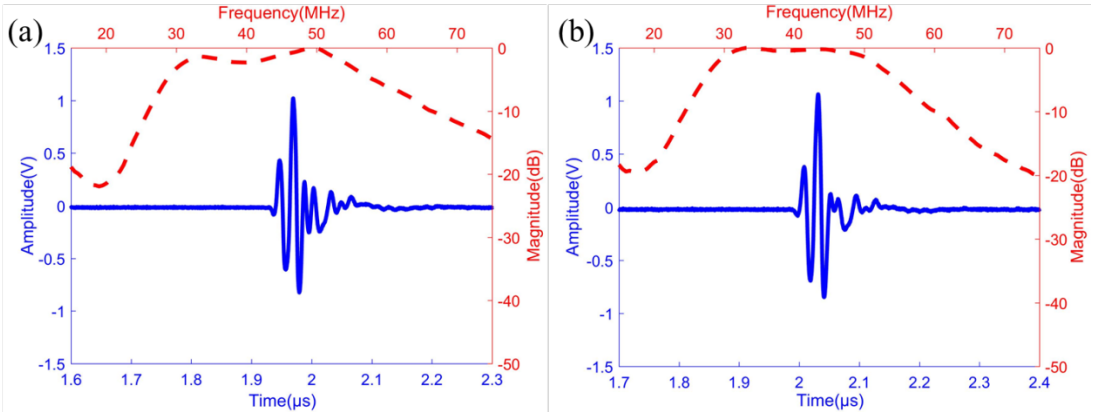

Fig. 3.9. Pulse-echo (black solid line) and spectrum (red dotted line) of planar (a) and focused (b) IVUS transducer.

The center frequencies of the planar and focused IVUS transducers were measured as 41 and 42 MHz. Furthermore, the −6 dB relative BWs were 68% for the planar transducer and 71% for the focused transducer. The BW of the focused IVUS transducer was slightly higher than that of the planar IVUS transducer. This difference can be attributed to the lower mechanical quality factor caused by the pressing process, which causes damping and broadens the frequency response.

3.4.3 Imaging Evaluation of the textured PIN-PSN-PT-based IVUS Transducers

Figs. 3.10(a) and (b) present the wire phantom images acquired by the planar and focal PIN-PSN-PT-based IVUS transducers. It is evident that the focused transducer provided superior lateral resolution than the planar transducer at different depths.

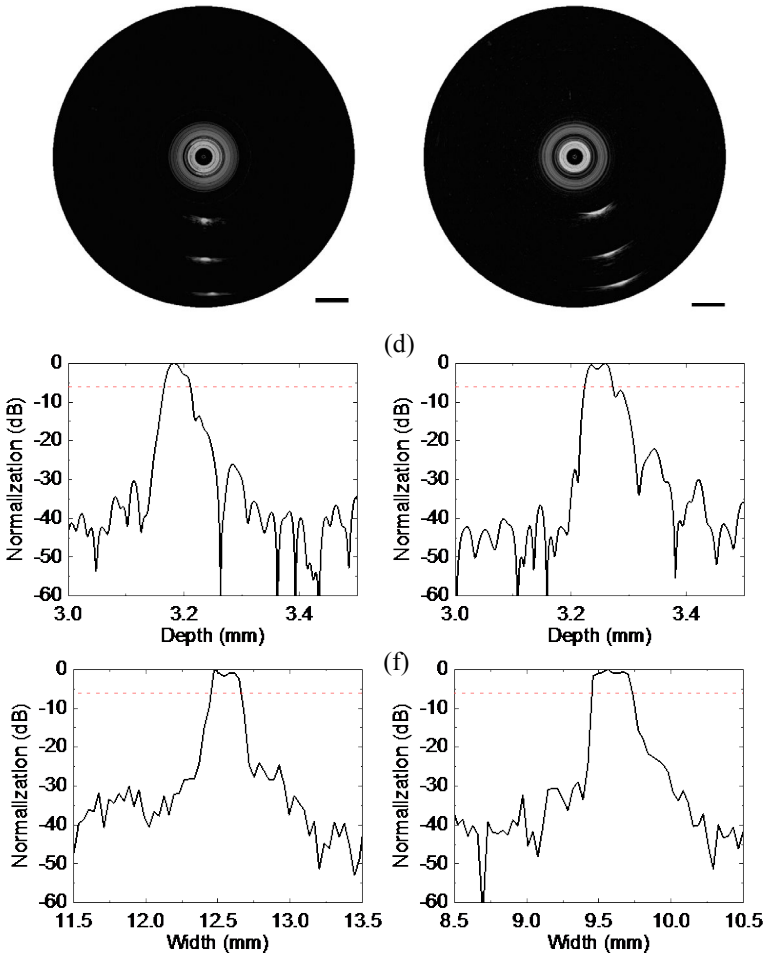

Fig. 3.10. The images of wire phantom acquired by the textured PIN-PSN-PT-based (a) focused and (b) planar IVUS transducers. axial resolution of the (c) focused and (d) planar IVUS transducers. lateral resolution of the (e) focused and (f) planar IVUS transducers. Dynamic range: 50 dB.

Fig. 3.11 displays the axial and lateral beam profiles used for resolution calculation. The axial and lateral resolutions of the focused transducer, determined using the FWHM width, were 45 and 208 μm, respectively. By contrast, the planar transducer exhibited the axial and lateral resolutions of 48 and 282 μm, respectively. Thus, these experimental results aligned well with the simulated results. The focused transducer

exhibited improved resolution performance in both axial and lateral aspects compared with the planar transducer.

Table 3.3. Comparison of simulated and measured spatial resolutions for the planar and focused IVUS transducers.

	Axial resolution (μm)		Lateral resolution (μm)	
	Simulated	Measured	Simulated	Measured
Focused	41	45	203	208
Planar	42	48	243	282

A segment of porcine coronary artery was selected for ultrasound imaging to assess the tissue imaging capabilities of the textured PIN-PSN-PT-based focused and planar IVUS transducers and traditional PZT-5H-ceramic-based planar transducer (Fig. 3.10). The resulting images from both types of transducers revealed fatty tissue-surrounded vessel walls in 50 dB dynamic range. The focused transducer provided a clearer distinction of the inner tunica intima of the vessel wall. Moreover, the focused transducer exhibited better imaging contrast than the planar transducer, resulting in a brighter image view. It is noteworthy that the PZT-5H-ceramic-based transducer exhibits significantly inferior imaging contrast, limiting visualization to approximately 0.5-mm-thick tissues. In contrast, the PIN-PSN-PT-textured ceramic-based focused and planar transducers allow visualization of thicknesses around 1 mm and 0.9 mm of tissues, respectively, under the same conditions. These results highlighted the potential

of focused IVUS transducers constructed with the textured PIN-PSN-PT ceramics for intravascular applications. The improved spatial resolution and SNR of the focused transducer can contribute to the enhanced visualization and characterization of vessel structures, making it a promising tool for intravascular imaging.

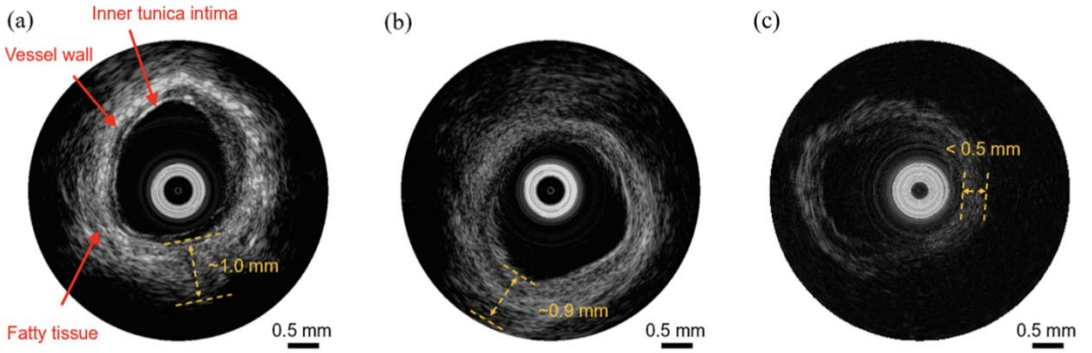

Fig. 3.11. Porcine artery ultrasound images acquired using the textured PIN-PSN-PT-based (a) focused and (b) planar IVUS transducers and commercial PZT-5H based planar IVUS transducer with dynamic range of 50 dB.

3.5 Discussion

In the field of vascular imaging, IVUS is a frequently employed technique owing to its capability to offer a real-time 3D visualization of plaque morphology. However, the imaging resolution of conventional IVUS is limited with regard to the diagnosis of early-stage plaques. Thus, there have been proposals for the use of UHF IVUS, which offer superior resolution[72, 118]. Nonetheless, the application of UHF ultrasound is restricted by their limited penetration depth because of its high attenuation [57]. In addition, geometrically focused IVUS has been suggested to enhance imaging

resolution[82-86]. However, the tiny size of the piezoelectric elements employed in IVUS poses a challenge in achieving a well-focused acoustic field.

The present study introduced a novel approach to focused IVUS catheters utilizing textured PIN-PSN-PT ceramics. The presence of electrical impedance mismatch in the transducer leads to a decrease in signal amplitude and SNR[119]. Conventionally, in order to achieve an appropriate electrical impedance (50 Ω), the aperture of the IVUS element is restricted to a small dimension of 0.4 × 0.5 mm^2. However, with the implementation of textured PIN-PSN-PT ceramics, the proposed transducer attains suitable electrical impedance while possessing a larger size of 0.6 × 0.6 mm^2. The simulation results confirm that this larger-scale transducer design generates a well-focused acoustic field. Comparative analysis indicates that, compared to the planar transducer, the focusing transducer exhibits negligible change in axial resolution, which is associated with bandwidth, while significantly improving lateral resolution.

Chapter 4 Dual-Element IVUS Catheter

4.1 Introduction

As discussed in Chapter 1, solid-state IVUS imaging and mechanical IVUS imaging are commonly used imaging modalities in clinical practice. The key distinction between these two modalities lies in the type of ultrasound transducer employed. In solid-state IVUS, the transducer is an array transducer with elements evenly arranged in a circular pattern in the tip of the catheter. Transmit and receive beamforming of ultrasound can be executed by employing different electronic delays to different elements to acquire ultrasound images[120]. However, due to their small size and processing challenges, solid-state IVUS transducers typically operate at 20 MHz frequency, resulting in limited imaging resolution.

In mechanical IVUS imaging, a HFU transducer with one element is installed in the distal end of a torque cable, and a motor is used to rotate the torque cable in circular motions. This scanning mechanism enables the acquisition of cross-sectional ultrasound images of intravascular morphology. Notably, the resolution of the image improves with higher ultrasound frequencies[121, 122]. Compared to solid-state IVUS, mechanical IVUS has a simpler design and the ability to achieve higher transducer frequencies, resulting in improved resolution and wider application potential. However, one limitation of mechanical IVUS arises when the catheters are maneuvered through

tortuous vessel segments. The friction between the sheath and drive shaft can lead to NURD [51, 123, 124]. Indeed, the NURD in mechanical IVUS catheters is an undesirable characteristic that can negatively impact the quality of IVUS imaging (as shown in Fig. 4.1). It makes it challenging to obtain accurate assessments of sharply curved coronary vessels[51, 125, 126].

One approach of image processing techniques is to track and predict tissue motion by analyzing the cross-correlation between different frames of IVUS images[127]. Additionally, structural markers such as scaffolds can be utilized to enable accurate registration and alignment of the acquired data[128]. Frequency-domain analysis of IVUS vascular image textures can provide valuable information for image compensation, specifically regarding the rotation velocity and angle of the transducer. [129]. Nevertheless, all of these techniques almost need a high degree of correlation between consecutive IVUS frames. Moreover, these techniques can be computationally intensive, especially when processing large amounts of image data. This can pose challenges when it comes to real-time implementation, as the processing time may exceed the desired frame rate for real-time imaging[130, 131].

Connecting the catheter ultrasound transducer or mirror directly to a built-in micromotor can indeed help improve NURD in mechanical IVUS imaging. However, integrating a micromotor directly into the catheter increases the processing complexity and aperture of the catheter. The motor rotational speed can be raised by increasing the

current magnitude, which in turn enhances the frame rate of the image acquisition. Nevertheless, this approach poses challenges related to heat dissipation[132-135]. The concept of integrating two array elements with different frequencies into a single ultrasound catheter has been proposed. This configuration allows for the utilization of super-harmonic imaging techniques[136] and represents a promising technique to optimizing the trade-off between spatial resolution and penetration depth[72, 73, 75, 137, 138].

A dual-element IVUS catheter is developed to address NURD encountered in mechanically rotating catheters in this work. In the catheter, two elements with similar frequencies and other properties are arranged in a back-to-back configuration. When the catheter experiences NURD during the imaging process, the abnormal image portion obtained from one element can be substituted with the corresponding good ultrasound image acquired by the other element in the catheter. In addition, it allows for obtaining two images in a single rotation, effectively doubling the imaging frame rate compared to a single-element configuration. To evaluate the imaging resolution of these two elements, wire phantom imaging was performed. Additionally, the feasibility and overall imaging performance of the proposed protocol were identified using a house made tissue phantom and porcine vascular imaging. The outcomes indicate that the strategy of this word has the potential to improve NURD artifacts.

4.2 Methods

4.2.1 Design and Fabrication

According to the typical clinical application requirements, the catheter's two elements are designed with the same size and an center frequency of 40 MHz[139]. To ensure that the two elements of the catheter can capture ultrasound images in the same cross-section as the catheter rotates one full revolution, they are arranged back-to-back within a copper casing. Fig. 4.1 presents a schematic diagram illustrating the structure of a dual-element catheter.

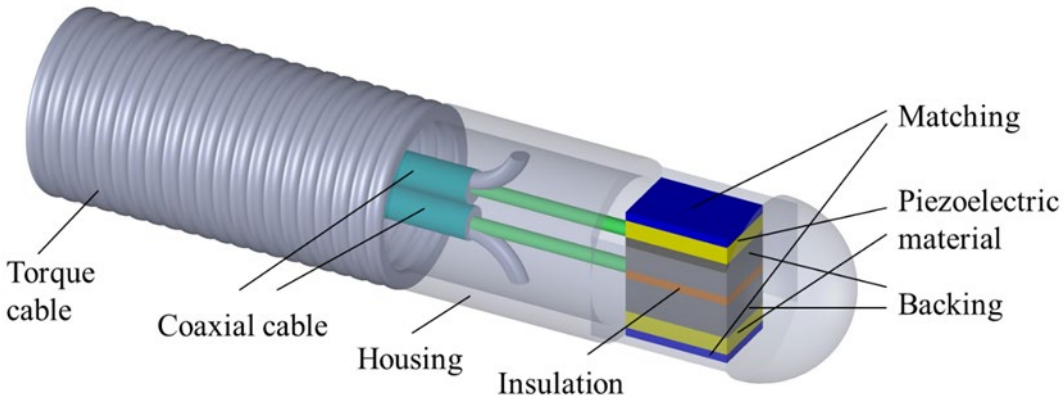

Fig. 4.1. Structural schematic diagram of the dual-element catheter.

The transducers in this study were made using PZT-5H ceramics as the piezo-material. PZT-5H is chosen for its excellent stability due to its high Curie temperature. The transducers made from PZT-5H typically do not require repolarization[73, 75]. The transducer surface is deposited with two matching layers. Table 4.1 provides the parameters and materials of the proposed catheters.

Table 4.1. Parameters and materials of the dual-element catheter.

Number of elements	2
Fc (MHz)	40
Aperture (mm)	0.4 × 0.6
The material of piezoelectric layer	3203HD ceremic
The material of 1st matching layer	Siliver powder/epoxy
The material of 2nd matching layer	Parylene C
The material of backing layer	Conductive epoxy

The fabrication process for the transducer's elements involves the following steps: First, The piezoelectric ceramic raw material is bonded onto the sapphire substrate using wax. Second, the ceramic is ground down to 50 μm thick using a grinding machine and polished it. Third, Cr/Au layers are sputtered onto both surfaces of the ceramic, serving as the electrode layer of the transducer. Fourth, 2-3.5 μm silver powder and epoxy are prepared and thoroughly mixed. This mixture is then cast onto the negative electrode surface, serving as the 1st matching layer and it is subsequently ground to 10 μm thick. Fifth, A conductive epoxy is applied onto the opposite electrode surface, acting as a backing material. It is then cured to ensure its solidification. Subsequently, the backing material is ground to obtain the desired thickness. Finally, the sample is divided into tiny stacks with dimensions of 0.4 × 0.6 mm^2.

An insulating epoxy is used to bond and assemble the two transducer elements into a

copper tube (OD: 0.96 mm). Two coaxial cables, each consisting of a ground and a signal wires, are employed to link the elements to the imaging platform. The signal wires of the cables are bonded to the conductive backing of each transducer element using E-Solder. The two cables are inserted within a torque cable (OD: 0.86 mm). Cables' ground wires are connected to the tube through the use of E-solder. A Cr/Au layer is sputtered on the tube to insure a sufficient connection to the ground. Lastly, Parylene is deposited on the catheter assembly to play the role of matching and protective coating.

4.2.2 Characterization

To acquire the measured Fc and -6 dB BW of the developed transducer, the following procedure is followed: The catheter is placed in deionized water. A polished quartz blocks is positioned on the front of the elements. A pulse generator/receiver is utilized to stimulate the transducers, and the received signals are shown on an oscilloscope. By analyzing the data obtained from the oscilloscope, the Fc and -6 dB BW of the transducer can be calculated.

An ordinary crosstalk measurement method was performed to evaluate the transmission crosstalk between the two elements. The following steps are performed: A function generator (AFG31252) with burst mode was employed, generating a 40MHz signal with a duration of 15 cycles with amplitude of $10V_{pp}$. The generated

signal is used to excite one of the elements of the catheter. An oscilloscope is used to measure the voltage across the other component. The method of dual-element crosstalk test was shown in Fig. 4.2. The transmission crosstalk of the two elements was calculated according to the following formula[140]:

$$\text{Crosstalk}_t = 20\log\frac{V_c}{V_r} \quad (4\text{-}1)$$

where V_c is the excited voltage, V_r is the received voltage.

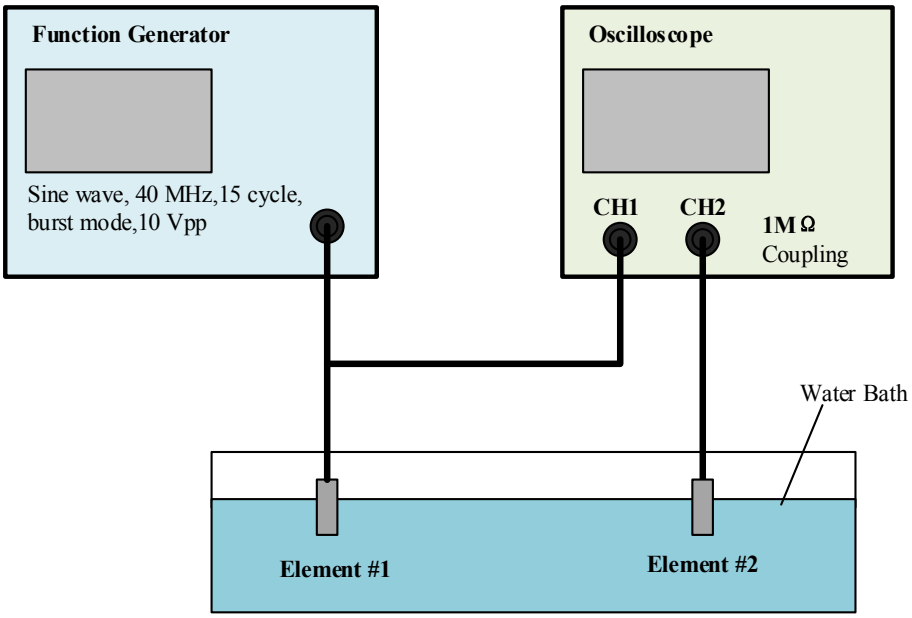

Fig. 4.2. Schematic diagram of crosstalk test method between elements.

4.2.3 Dual-Channel Imaging System

A system for dual-channel HFU imaging has been developed in this work, as depicted in Fig. 4.3. The system comprises several components, including a dual-element catheter, a multi-channel rotator, a dual-channel platform, and a personal computer.

The platform is implemented as a 12-layer PCB, housing two pulse generators/receivers. The imaging platform incorporates a power supply unit capable of generating high amplitude bipolar pulse with positive and negative signals. The excitation strategy is executed using metal-oxide-semiconductor field effect transistor (MOSFET) with characteristics of significant amplitude, significant output current and small threshold signals. These MOSFET drivers are manipulated by the FPGA to regulate the characteristics of the excitation pulses.

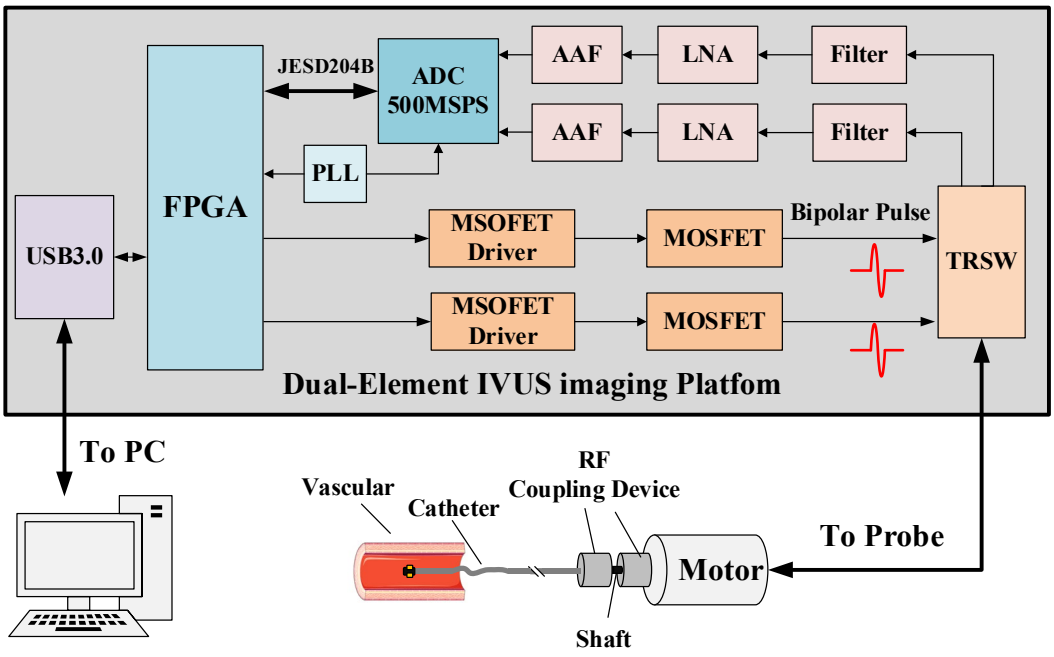

Fig. 4.3. Working diagram of the proposed imaging system for IVUS application.

In the rotation imaging of the IVUS system, the catheter is connected to a mechanical device equipped with a rotating motor. The rotation of the motor drives the catheter to achieve 360˚ imaging. Regarding the receiving part of the ultrasonic signal, the echo signal undergoes specific processing. Firstly, the transceiver switch (TRSW) clamps

the high-voltage portion of the received signal to 0.6V. This prevents the high-voltage transmission from damaging the components of the receiving channel. Subsequently, a two-stage small-noise amplifier is employed to amplify the clamped echo signal. This amplifier is designed to have a lower noise figure, ensuring minimal noise interference. The total gain of the system, after the two-stage amplification, is 52.6 dB.

To ensure accurate and reliable signal processing, a 5th-order analog LPF is designed in the system. This filter is responsible for attenuating HFU noise and reducing the aliasing of noise and signal. The analog-to-digital conversion stage utilizes a 14-bit dual-channel high-speed ADC. This enables the conversion of the dual-channel ultrasonic signals into digital format. Once digitized, the digital signals are transmitted to the FPGA through the JESD204B interface. This interface ensures high-speed data transmission with a maximum rate of 12.5 Gbps. In the FPGA, the echo data undergoes various signal processing operations, including low-pass filtering, Hilbert transform and envelope detection. These processing steps refine and enhance the captured ultrasound signals. Finally, the processed dual-channel ultrasound data is transmitted to the computer via the USB 3.0 interface. The data is displayed on the PC, providing immediate visualization and analysis capabilities.

4.2.4 Evaluation of Wire Phantom

To evaluate the spatial resolution, structural symmetry, and performance consistency of the two elements in the IVUS catheter, a tungsten wire phantom is created. The mold comprises 10 μm tungsten wires. The experimental setup involves placing the tungsten wire mold in deionized water. The dual-element catheter is then positioned at the center of the wire mold. A rotating device is connected to the catheter and used to drive it at a speed of 20 revolutions per minute. Each frame of the imaging consists of 500 scan lines. During the rotation, the IVUS system captures and saves the real-time imaging data of the tungsten wire model using the dual-array elements of the catheter. The subsequent image processing and analysis are conducted using Matlab, allowing for further evaluation and examination of the acquired imaging data.

4.2.5 Evaluation of Tissue Phantom

To evaluate the improvement of NURD condition by the dual-element IVUS catheter, verification experiments were conducted using tissue body membranes and isolated porcine blood vessels. The tissue body membrane is fabricated by blending Sigmacell cellulose and polyvinyl alcohol powder. The design requirements of the tissue phantom are detailed in Fig. 4.4. Two hypoechoic holes, one with a diameter of 2mm and the other with a diameter of 3mm, are created within the membrane. The central 3 mm hole functions as the imaging hole for the dual-element catheter. The 2 mm hole

serves as a reference for evaluating the preservation of tissue facts after image modification. Because of the hole of the tissue phantom is a regular circle, an isolated porcine blood vessel with an irregular lumen is selected to further assess the corrective capability of the dual-element catheter for NURD. This blood vessel provides a more realistic and challenging scenario for evaluating the correction capabilities of the catheter.

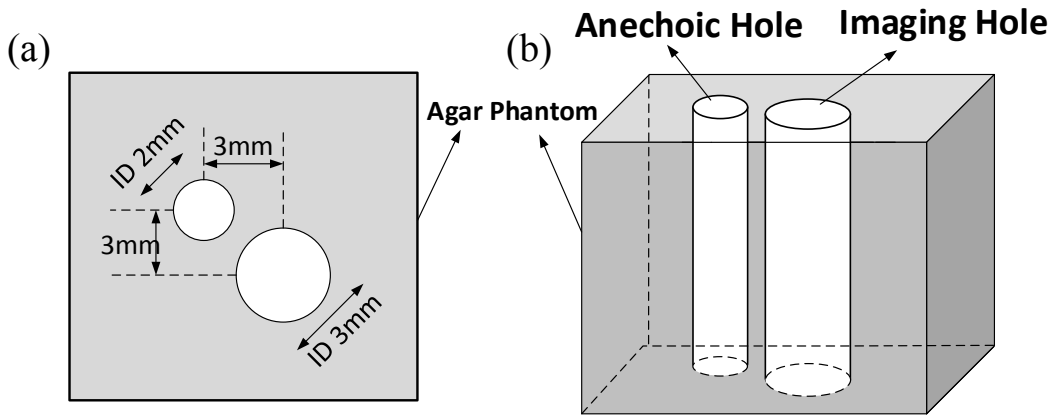

Fig. 4.4. Schematic of the house made tissue phantom: (a) top and (b) three-dimensional view.

4.2.6 Image Reconstruction

The rotational speed of the catheter is maintained at 20 rotations per minute. For each rotation, the imaging system is capable of simultaneously acquiring two frames of image. Importantly, one of the frames is identical to the other when rotated by 180°, thereby providing a symmetrical image. When the catheter passes through a section of an acutely curved vessel resulting in NURD, the same distortion will appear on the symmetrical position in the subsequent frame. By extracting accurate information

from both frames, a more complete image can be reconstructed. To ensure smooth image stitching, three adjacent lines at the location of the stitching are smoothed. This helps to minimize any visual discontinuities in the final image. By utilizing the accurate information from two frames, a comprehensive image can be reconstructed, enabling a more accurate representation of the imaged area. This technique helps to mitigate the impact of NURD on the final image quality.

4.3 Results

4.3.1 Performance of the Imaging Platform

Fig. 4.5 showcases the various components and equipment used in the imaging system. These components mainly include a rotator, a mechanical catheter, a power source, a tissue phantom, an imaging software and a dual-channel imaging PCB. The receiving channel of the system has a bandwidth of 20-75MHz, allowing for a wide range of frequency reception.

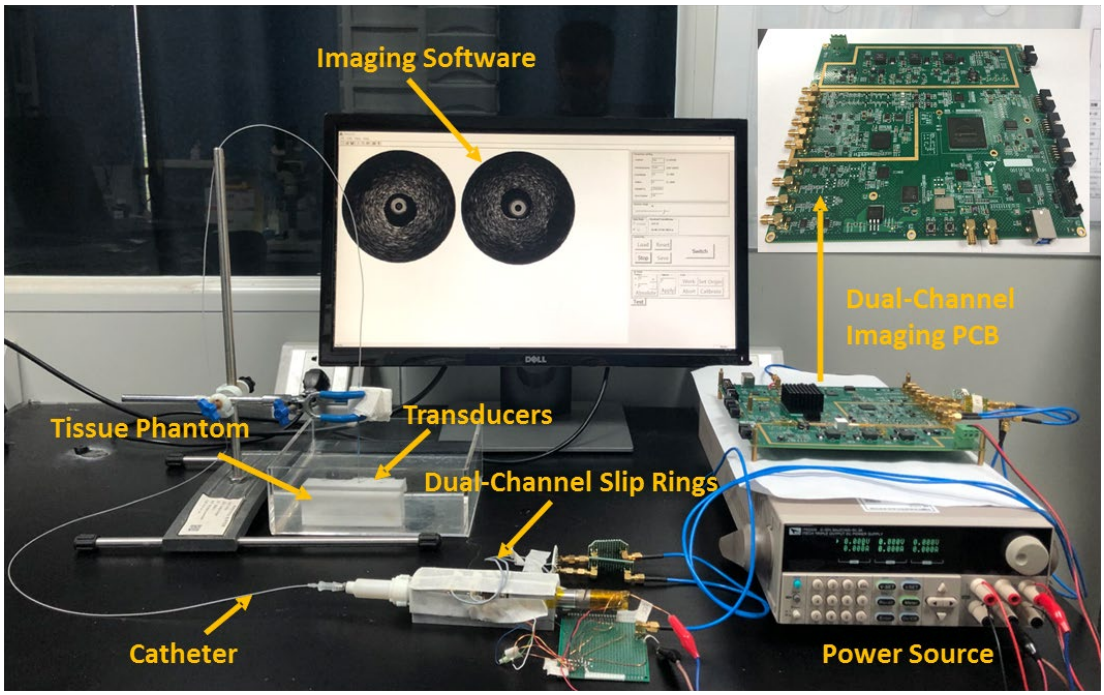

Fig. 4.5. Prototype of the dual-channel IVUS imaging platform.

The dual-channel pulse transmitting circuit generates a bipolar pulse (as shown in Fig. 4.6) with an Fc of 44.9MHz, a V_{pp} value of 94 V, and a 141% -6dB bandwidth. This pulse waveform is designed to cover the range of the frequency applicable to the dual-element transducer. The imaging platform utilizes the JESD204B interface for high-speed data transmission between the FPGA and ADC. The maximum channel rate achievable with this interface is 12.5 Gbps, ensuring efficient data transfer. After undergoing digital signal processing in the FPGA, the ultrasound data is transmitted to the host computer through a USB3.0 interface. The data transfer rate exceeds 100 MB/s, enabling real-time acquisition and presentation of the dual-channel imaging data.

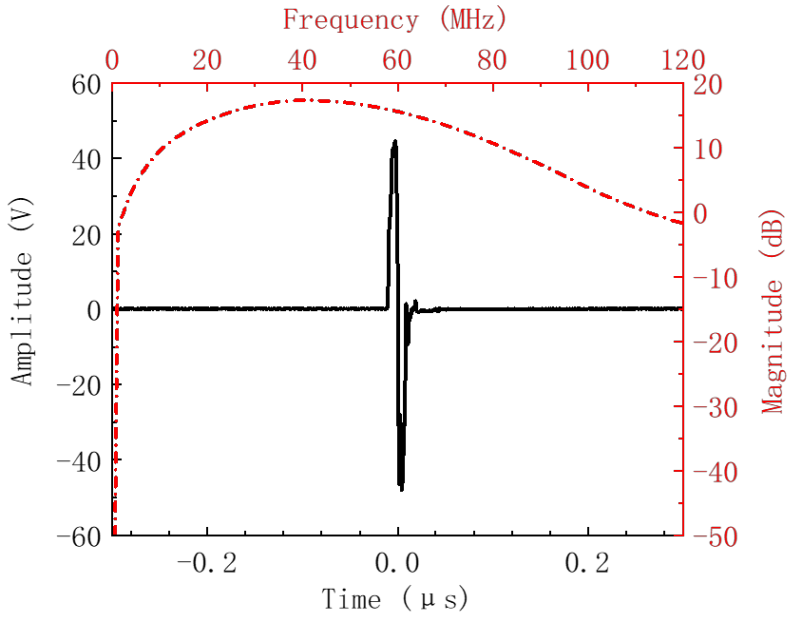

Fig. 4.6. The pulse waveform and spectrum of the bipolar pulse.

4.3.2 Characteristics of the Dual-Element Catheter

Fig. 4.7 presents the photographs of the prototype of the proposed catheter and transducer, providing a visual representation of the actual devices used in the system. In Figs. 4.7(b) and (c), the pulse-echo responses of the two elements are depicted. Element A has a center frequency of 40.4MHz, while element B has an center frequency of 41.1MHz. The -6 dB bandwidths of element A and element B are measured to be 67% and 63.3%, respectively.

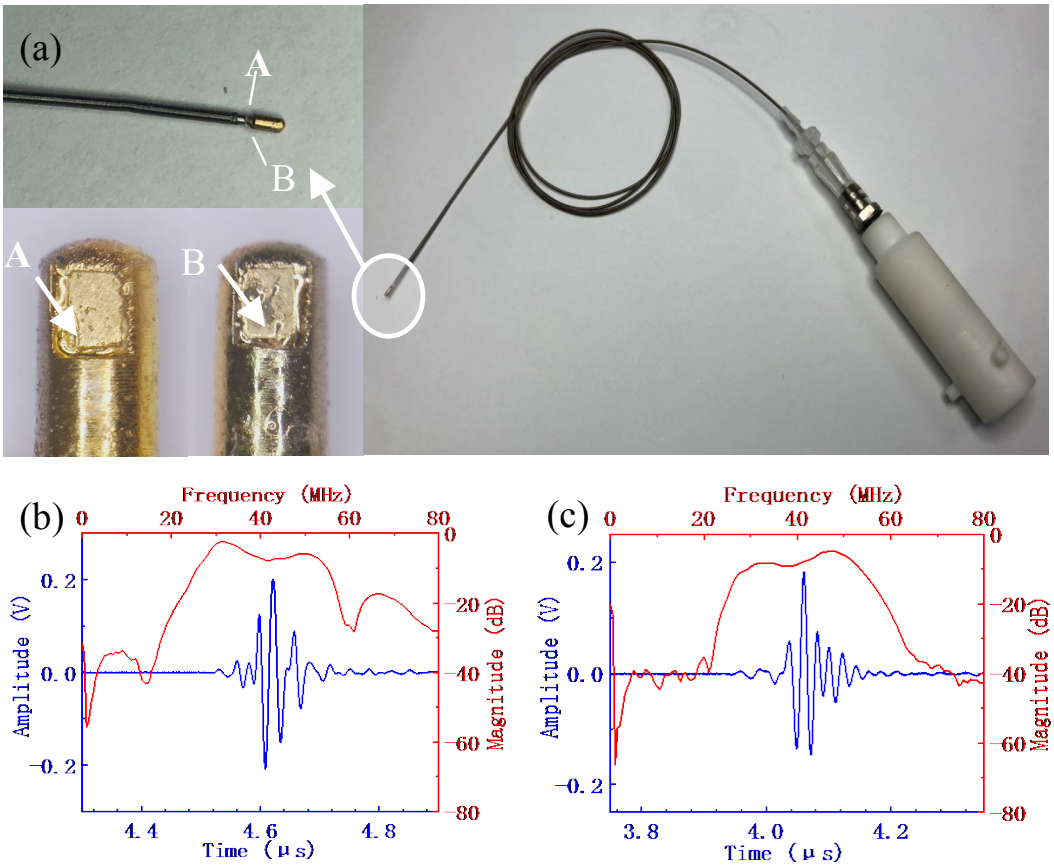

Fig. 4.7. (a) The image of the proposed catheter, echo curves of element (b) A and (c) B.

Furthermore, testing revealed that the crosstalk between the two components is -68 dB. Crosstalk refers to the interference or leakage of signals between adjacent transducer elements. A value of -68 dB indicates a minimal level of crosstalk between the two elements. According to the results, it can be deduced that the property of both elements is similar and meets the expected design requirements. The performance of both elements is shown in Table 4.2.

Table 4.2. The performance of element A and B.

	Element A	Element B
Center frequency (F_c)	40.4 MHz	41.1 MHz
-6 dB bandwidth	67%	63.3%
Axial resolution	31 μm	34 μm
Lateral resolution	167 μm	185 μm
SNR	25.2 dB	23.4 dB
Crosstalk	-68 dB	

4.3.3 Wire Phantom

Fig. 4.8(a) and (b) display the tungsten wire phantom imaging performed using the proposed catheter. In these two images, the echo amplitudes of the two sets of tungsten wire phantom are very similar. This demonstrates the consistency of the imaging performance between the two elements. Furthermore, the location of the five tungsten lines in Fig. 4.8(a) ranges from 21° to 31°, while in Fig. 4.8(b), it ranges from 198° to 208°. Observing the image, the difference of the angle between the tungsten wires imaging of the two elements is almost 180°. This illustrates that the two elements symmetry meets the design requirements.

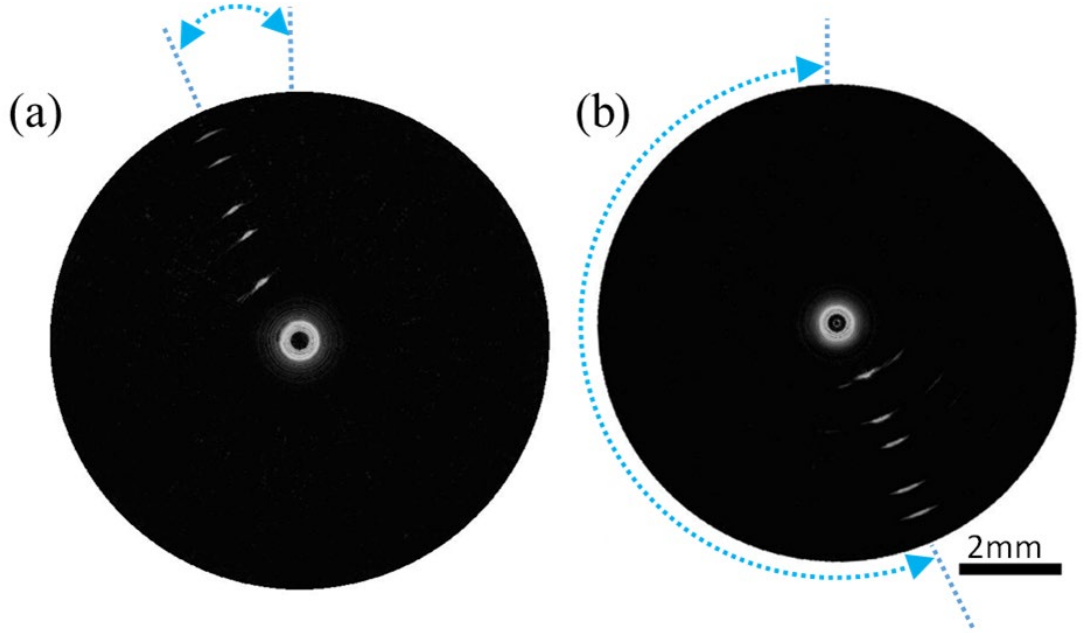

Fig. 4.8. Wire phantom images acquired by element (a) A and (b) B. Dynamic range: 35dB.

The resolution data analysis of the two elements is presented in Fig. 4.9(a-d). The axial and lateral imaging resolutions for elements A are 31 μm and 167 μm, respectively, while the axial and lateral resolution for elements B are 34 μm and 185 μm, respectively. The SNR of the images obtained by element A was calculated as 25.2 dB, while element B is 23.4 dB.

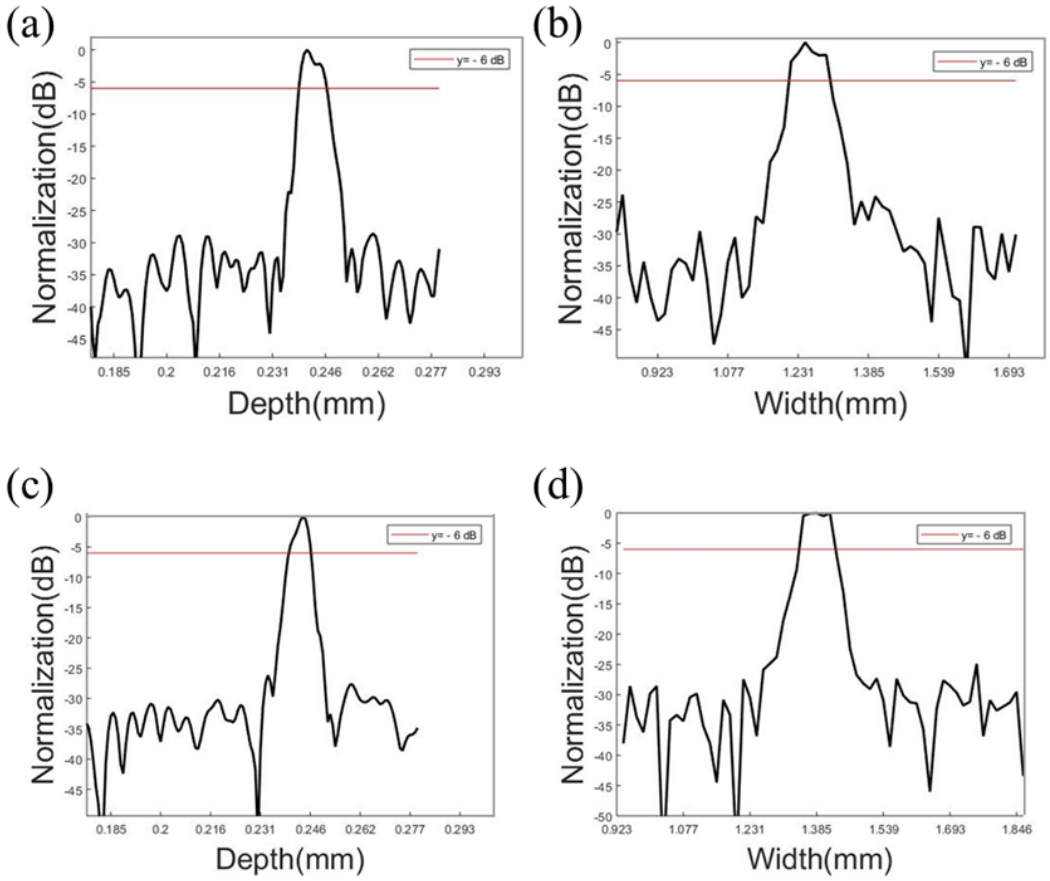

Fig. 4.9. The (a) axial and (b) lateral beam profiles of element A, the (c) axial and (d) lateral beam profiles of element B.

4.3.4 Tissue Imaging

Figs. 4.10(a-c) depict images of tissue phantoms representing a regular circular lumen. For ease of comparison, the starting locations of the two image frames are positioned symmetrically. During the real-time acquisition process, the image data is displayed sequentially in the direction of counterclockwise. Fig. 4.10 displays the images of NURD obtained from both elements. These images are acquired by significantly winding the torque coil. From Fig. 4.10(a), it can be concluded that the right

component of the ultrasonic image appears good result, while the left component exhibits NURD result (blue arrow), resulting in the loss of details from the hypoechoic hole. And, Fig. 4.10 (b) displays NURD on the right side (blue arrow zone), while the left component of the image appears normal, allowing the hypoechoic hole to be visible. To overcome the NURD effects and obtain a more complete image, Fig. 4.10 (c) demonstrates the extraction of the normal half of the tissue in the image of Fig. 4.10 (a) and (b). These extracted portions are then reconstructed into a single, complete frame. Gaussian filtering is applied to smoothen the image splicing process.

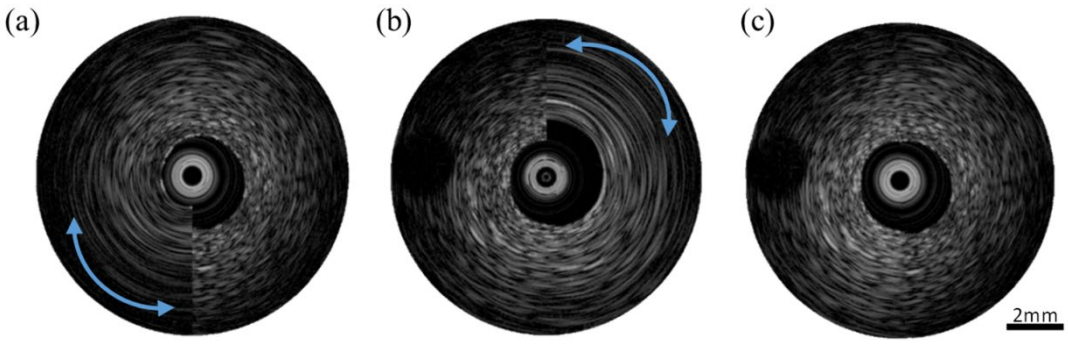

Fig. 4.10. NURD tissue phantom image of (a) element A and (b) element B. (c) Reconstructed image. Dynamic range: 35dB.

Figs. 4.11(a-c) showcase images of isolated porcine blood vessels, where the imaging lumen exhibits an irregular circular shape. Fig. 4.11(b) and (c) display the images with NURD zone captured by elements A and B, respectively. In Fig. 4.11(a), the NURD is appeared in the lower left component of the image (yellow arrow zone),

while the other component of the image appears available. And, Fig. 4.11(b) displays the top right component of this image is NURD (yellow arrow zone), while the other component of the image remains unaffected and appears normal. To obtain a complete and improved morphology of the swine artery, the right component of element A image and the left component of element B image are extracted. These extracted portions are then combined and reconstructed into a single frame. As illustrated in Fig. 4.11(c), this reconstruction process significantly improves the NURD phenomenon. By integrating the unaffected portions from both elements A and B, the negative impact of NURD is mitigated, resulting in a more coherent and representative image of the blood vessel structure.

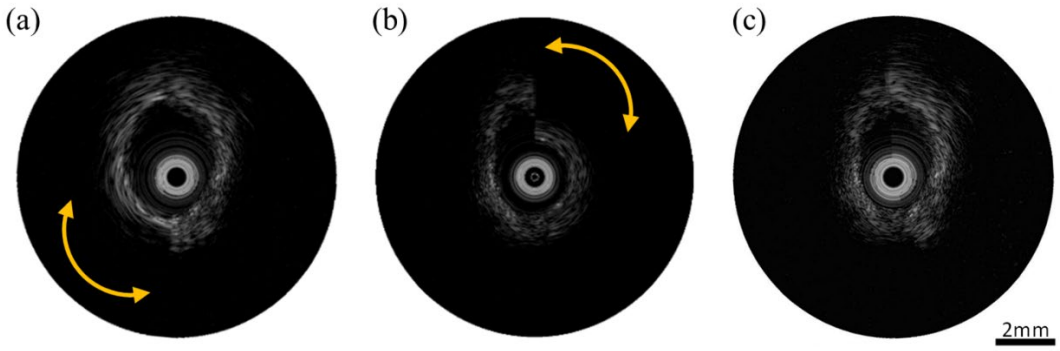

Fig. 4.11. NURD ex vivo porcine vessel image of (a) element A and (b) element B. (c) Reconstructed image. Dynamic range: 35dB.

4.4 Discussion

One of the significant advancements in modern medical technology is the application of IVUS in the early prediction and intervention of AS in arteries. Among the two

main types of IVUS catheters, the mechanically rotating IVUS catheter offers advantages in terms of design simplicity and the ability to achieve higher spatial resolution by operating at higher frequencies. As a result, it has found extensive applications in clinical settings. However, when mechanically rotating IVUS catheters are maneuvered through highly curved vessel segments, NURD often occurs. NURD is an inherent characteristic of mechanically rotating IVUS catheters. It can cause loss of image information in the affected segment, thus impacting the precise evaluation of acutely tortuous arteries. Prior studies have explored various methods to optimize NURD in catheter-based imaging tools, for example IVUS and OCT. Some approaches involve utilizing cross-correlation algorithms to track tissue motion and analyze the similarity of different frames of IVUS images, enabling compensation for NURD. Others employ frequency-domain analysis of IVUS vascular image textures to assess the rotation velocity and angle of the transducer, enabling appropriate adjustments. However, these techniques typically require high similarity among images, which may not always be achievable. Additionally, these methods involve substantial computational complexity, making real-time correction of NURD images challenging.

A dual-element IVUS imaging catheter that two elements were assembled back-to-back in one catheter was introduced in this work. The array elements in the catheter are designed to have the same center frequencies and dimensions.

Furthermore, an imaging platform with two channels was developed, incorporating a specially designed imaging platform with a dual-channel transceiver. To ensure the imaging consistency and similarity among the two elements, tungsten wire phantom imaging was performed and verified. The results demonstrate that the axial imaging resolutions of the two elements are 31 μm and 167 μm, respectively, and the lateral imaging resolutions of them are 34 μm and 185 μm, respectively. The effectiveness of the both elements in complementary imaging was further validated through the imaging of tissue phantom and isolated porcine blood vessels.

The tissue phantom, with its regular circular imaging aperture and uniform tissue composition, exhibits a better image reconstruction effect compared to isolated porcine blood vessels. The smoothing and filtering techniques applied during image reconstruction minimize the traces of splicing, resulting in a more seamless and visually coherent image. While there may be some traces of image splicing in the reconstruction of isolated porcine blood vessels, it does not hinder the overall observation and interpretation of missing tissue information. The fabrication of a dual-element IVUS catheter presents certain challenges. The two elements need to be precisely assembled within the metal housing, ensuring alignment and stability. Moreover, the alignment of the metal casing with the drive shaft must be maintained in a straight line. These intricate assembly requirements contribute to the complexity of manufacturing a dual-element IVUS catheter. In commercial IVUS catheters

commonly available today, the occurrence of NURD artifacts typically involves an area of less than 180 degrees. However, in extreme cases where the drive shaft becomes stuck or unable to rotate, it can significantly distort the imaging of both elements. The strategy proposed in this work may not be applicable in such extreme scenarios. Currently, the image data from both elements can be simultaneously acquired and subjected to offline processing. However, the future plan is to develop real-time compensation techniques to address NURD artifacts in the acquired images. This will enable on-the-fly correction of NURD artifacts and further enhance the imaging capabilities of the dual-element IVUS catheter.

Chapter 5 Conclusions and Future Work

5.1 Conclusions

In this thesis, several novel IVUS transducers were developed to improve the image quality of IVUS. Detailed research works were summarized as follows:

1. High frequency Focal IVUS transducer with a FZP layer

A HFU transducer with a FZP was developed in Chapter 3 for IVUS imaging. By employing theoretical calculations, the transducer's structure and parameters were optimized to achieve HFU capabilities. The COMSOL software was utilized to simulate the acoustic beam. The ultrasound element's aperture size is 0.778×0.9mm². In this study, both FZP and planar transducers were manufactured. The FZP transducer exhibited an Fc of 52.5 MHz and a –6 dB BW of 42%. In contrast, the plane-shape transducer possessed an Fc of 51.3 MHz and a –6 dB BW of 58%. To assess the transducers' performance, imaging experiments were performed using wire phantoms and porcine arteries. The FZP transducer demonstrated imaging resolutions of 47 μm axially and 184 μm laterally, while the planar transducer displayed imaging resolutions of 44 μm axially and 314 μm laterally. These findings indicate that the FZP transducer outperforms the planar transducer in terms of lateral resolution for IVUS applications. Consequently, this research presents a novel imaging tool could enhance the imaging quality of IVUS.

2. Geometrically focused IVUS transducer using PIN-PSN-PT ceramic

A focused IVUS catheter based on textured PIN-PSN-PT ceramics is designed and fabricated in this section. The focal transducer exhibited an Fc of 42 MHz and a -6 dB BW of 71%. For comparison, we also fabricated a planar transducer with identical parameters, featuring an Fc of 41 MHz and a BW of 68%. To assess the transducers' performance, the experiments of imaging were performed using wire phantoms and porcine arteries. The focused transducer demonstrated lateral imaging resolutions of 208 μm, while the planner transducer displayed lateral imaging resolutions of 282 μm. The focused transducer demonstrated superior lateral resolution, enabling enhanced visualization and differentiation of vascular structures. This advancement holds great potential for improving the efficacy and applicability of IVUS technology.

3. Dual-element IVUS catheter

Chapter 4 introduces a dual-element IVUS imaging catheter, where two elements with similar performance and the same center frequency are assembled back-to-back at the catheter head. The Fc and -6dB BW of these elements are 40.4 MHz with 67% bandwidth and 41.1MHz with 63.3% bandwidth, respectively. This configuration allows the catheter to acquire two frames of images during a single mechanical rotation. When NURD occurs due to extreme bending of the catheter, the distorted image from one element can be modified by the accurate image from the symmetrical

side element. This process enables the reconstruction of a complete and accurate image. Furthermore, in situations where NURD is not present, one rotation yields two frames of images, effectively doubling the imaging frame rate. To evaluate the symmetry and consistency of the two elements, a house made tungsten wire phantom was employed. The comprehensive imaging capability of the two transducers was validated using both tissue phantoms and isolated porcine blood vessels. Experimental results indicate that the proposed strategy effectively improves NURD condition and enhances the overall imaging performance.

5.2 Future Work

The IVUS imaging catheter holds significant value in the context of AP evaluation. However, despite its advantages, certain limitations have restricted its widespread application. The current research findings have made strides in addressing some of these issues. Nonetheless, there remains a need to explore and develop novel techniques to further optimize and enhance IVUS imaging:

1. High frequency array transducer

The implementation of an IVUS array transducer offers several advantages, including the ability to eliminate the need for mechanical transducer scanning, thus enabling safer and higher frame rate imaging. However, the fabrication of IVUS array transducers presents significant challenges, particularly as the frequency increases.

Consequently, conventional IVUS array transducers are typically limited to frequencies of up to 20 MHz, resulting in restricted resolution for visualizing atherosclerotic plaque (AP). To address this limitation, the development of HFU array transducers holds great potential for providing clearer ultrasonic images and becoming a crucial diagnostic tool for AP.

Therefore, it becomes imperative to explore novel fabrication methods and new materials for HFU array transducers. Such advancements could not only help reduce costs but also mitigate the fabrication difficulties associated with these devices.

2. Multi-mode imaging catheter

In recent times, there have been significant advancements in integrating IVUS with novel imaging modalities, including OCT, IVPA, fluorescence spectroscopy, and near-infrared reflectance spectroscopy (NIRS). These integrated techniques have proven to be valuable in enhancing diagnostic accuracy by providing additional information. However, the existing techniques face limitations in terms of their structural design and materials, hindering their widespread application and industrialization. Therefore, it is crucial to explore and develop novel materials and methods to optimize these multi-mode catheters. Such advancements hold the potential to promote the broader use of multi-mode catheters and offer effective diagnostic options for cardiovascular diseases.

Reference

[1] Y. Kokubo, and C. Matsumoto, "Hypertension is a risk factor for several types of heart disease: review of prospective studies," *Hypertension: from basic research to clinical practice*, pp. 419-426, 2017.

[2] W. H. O. (WHO). "Cardiovascular Diseases (CVDs). https://www.who.int/news-room/fact-sheets/detail/cardiovascular-diseases-(cvds)."", 2023.

[3] P. Libby, "The changing landscape of atherosclerosis," *Nature,* vol. 592, no. 7855, pp. 524-533, Apr 22, 2021.

[4] L. Y. Ma, W. W. Chen, R. L. Gao, L. S. Liu, M. L. Zhu, Y. J. Wang, Z. S. Wu, H. J. Li, D. F. Gu, Y. J. Yang, Z. Zheng, and S. S. Hu, "China cardiovascular diseases report 2018: an updated summary," *Journal Of Geriatric Cardiology,* vol. 17, no. 1, pp. 1-8, 2020.

[5] D. Zhao, J. Liu, M. Wang, X. Zhang, and M. Zhou, "Epidemiology of cardiovascular disease in China: current features and implications," *Nat Rev Cardiol,* vol. 16, no. 4, pp. 203-212, Apr, 2019.

[6] J. A. Ambrose, and A. S. Bhullar, "Inflammation and Thrombosis in Coronary Atherosclerosis: Pathophysiologic Mechanisms and Clinical Correlations," *EMJ,* vol. 4, no. 1, pp. 71-78, 2019.

[7] A. Gistera, and G. K. Hansson, "The immunology of atherosclerosis," *Nat Rev Nephrol,* vol. 13, no. 6, pp. 368-380, Jun, 2017.

[8] R. Virmani, F. D. Kolodgie, A. P. Burke, A. Farb, and S. M. Schwartz, "Lessons from sudden coronary death: a comprehensive morphological classification scheme for atherosclerotic lesions," *Arterioscler Thromb Vasc Biol,* vol. 20, no. 5, pp. 1262-75, May, 2000.

[9] J. R. Nelson, O. Wani, H. T. May, and M. Budoff, "Potential benefits of eicosapentaenoic acid on atherosclerotic plaques," *Vascul Pharmacol,* vol. 91, pp. 1-9, Apr, 2017.

[10] F. Otsuka, M. C. Kramer, P. Woudstra, K. Yahagi, E. Ladich, A. V. Finn, R. J. de Winter, F. D. Kolodgie, T. N. Wight, H. R. Davis, M. Joner, and R. Virmani, "Natural progression of atherosclerosis from pathologic intimal thickening to late fibroatheroma in human coronary arteries: A pathology study," *Atherosclerosis,* vol. 241, no. 2, pp. 772-82, Aug, 2015.

[11] G. Danaei, M. M. Finucane, J. K. Lin, G. M. Singh, C. J. Paciorek, M. J. Cowan, F. Farzadfar, G. A. Stevens, S. S. Lim, L. M. Riley, M. Ezzati, Z. Abdeen, C. Agyemang, M. Al Nsour, M. M.

Ali, R. Ambady, B. V. Babu, C. M. Barbagallo, A. Barcelo, S. M. Barreto, H. Barros, L. E. Bautista, P. Bjerregaard, C. Bjorkelund, S. Bo, M. Bobak, E. Bonora, M. A. Botana, P. Bovet, J. Breckenkamp, M. M. Breteler, G. Broda, I. J. Brown, M. Bursztyn, A. C. de Leon, E. Casiglia, K. Castetbon, S. Chatterji, Z. M. Chen, C. J. Chen, L. Chua, R. Cifkova, L. J. Cobiac, R. S. Cooper, R. S. Dankner, G. H. Dong, P. Elliott, C. Erem, A. Esteghamati, J. G. Fan, C. Ferreccio, J. O. Firmo, N. S. Fornes, F. D. Fuchs, L. Getz, S. Giampaoli, L. F. Gomez, S. Graff-Iversen, R. G. Carvajal, M. C. Gulliford, P. C. Gupta, O. Gureje, T. W. Hansen, J. He, J. Heinrich, A. Hennis, V. M. Herrera, S. C. Ho, M. M. Ibrahim, N. Ikeda, T. H. Jafar, M. R. Joffres, J. B. Jonas, R. M. Kamadjeu, I. Karalis, M. J. Kastarinen, J. Katz, P. Kelly, O. Khalilzadeh, Y. H. Khang, S. Kiechl, K. W. Kim, J. Kobayashi, R. Kubinova, Y. S. Kusuma, T. H. Lam, C. M. M. Lawes, C. Le, J. Lee, X. Lin, H. H. Lin, C. C. Lin, X. Q. Liu, R. Lorbeer, S. Ma, G. S. Ma, D. J. Magliano, M. Makdisse, G. Mancia, J. C. N. Mbanya, J. Miettola, H. V. Minh, J. J. Miranda, M. K. Mohamed, V. Mohan, A. H. Mokdad, D. D. Morales, K. Morgan, L. M. Muiesan, S. Muntoni, I. Nabipour, V. Nangia, H. Neuhauser, T. Ninomiya, O. Olivieri, A. E. Onal, A. Onat, M. Orostegui, D. B. Panagiotakos, F. Panza, M. S. Pednekar, C. Perez, R. Perez-Fernandez, R. Pichardo, H. P. Phua, P. Plans, N. Poulter, O. T. Raitakari, S. Rampal, L. Rampal, J. Redon, L. Revilla, R. B. Roaeid, R. Rojas-Martinez, S. Y. Sanisoglu, S. Sans, H. Schelleman, I. J. C. Schneider, D. A. S. Silva, E. Silva, L. A. Simons, M. Smith, S. Soebardi, V. Solfrizzi, A. D. Stein, G. S. Stergiou, J. Stessman, M. Suka, K. Tambs, F. Tesfaye, M. Thorogood, R. S. Tilvis, P. Trenkwalder, J. O. Tuomilehto, C. Tzourio, S. Vander Hoorn, M. P. Vanderpump, M. Verschuren, J. Vioque, S. Waspadji, L. Wilhelmsen, J. Willeit, M. Woodward, A. J. Xavier, L. Xu, G. H. Yang, L. C. Yeh, J. S. Yoon, Q. S. You, M. Zhou, and G. B. M. R. F. C, "National, regional, and global trends in systolic blood pressure since 1980: systematic analysis of health examination surveys and epidemiological studies with 786 country-years and 5.4 million participants," *Lancet,* vol. 377, no. 9765, pp. 568-577, Feb 12, 2011.

[12] P. K. Shah, "Role of inflammation and metalloproteinases in plaque disruption and thrombosis," *Vasc Med,* vol. 3, no. 3, pp. 199-206, 1998.

[13] M. Naghavi, P. Libby, E. Falk, S. W. Casscells, S. Litovsky, J. Rumberger, J. J. Badimon, C. Stefanadis, P. Moreno, G. Pasterkamp, Z. Fayad, P. H. Stone, S. Waxman, P. Raggi, M. Madjid, A. Zarrabi, A. Burke, C. Yuan, P. J. Fitzgerald, D. S. Siscovick, C. L. de Korte, M. Aikawa, K. E. Juhani Airaksinen, G. Assmann, C. R. Becker, J. H. Chesebro, A. Farb, Z. S. Galis, C. Jackson, I. K. Jang, W. Koenig, R. A. Lodder, K. March, J. Demirovic, M. Navab, S. G. Priori, M. D. Rekhter, R. Bahr, S. M. Grundy, R. Mehran, A. Colombo, E. Boerwinkle, C. Ballantyne, W. Insull, Jr., R. S. Schwartz, R. Vogel, P. W. Serruys, G. K. Hansson, D. P. Faxon, S. Kaul, H. Drexler, P. Greenland, J. E. Muller, R. Virmani, P. M. Ridker, D. P. Zipes, P. K. Shah, and J. T. Willerson, "From vulnerable plaque to vulnerable patient: a call for new definitions and risk assessment strategies: Part I," *Circulation,* vol. 108, no. 14, pp. 1664-72, Oct 7, 2003.

[14] Z. X. Huang, W. Dong, H. L. Duan, and J. Q. Liu, "A Regularized Deep Learning Approach for

Clinical Risk Prediction of Acute Coronary Syndrome Using Electronic Health Records," *IEEE Transactions on Biomedical Engineering,* vol. 65, no. 5, pp. 956-968, May, 2018.

[15] K. Pohle, S. Achenbach, B. MacNeill, D. Ropers, M. Ferencik, F. Moselewski, U. Hoffmann, T. J. Brady, I. K. Jang, and W. G. Daniel, "Characterization of non-calcified coronary atherosclerotic plaque by multi-detector row CT: Comparison to IVUS," *Atherosclerosis,* vol. 190, no. 1, pp. 174-180, Jan, 2007.

[16] W. C. Scarfe, A. G. Farman, and P. Sukovic, "Clinical applications of cone-beam computed tomography in dental practice," *Journal Of the Canadian Dental Association,* vol. 72, no. 1, pp. 75-80, Feb, 2006.

[17] G. P. Reddy, D. M. Chernoff, J. R. Adams, and C. B. Higgins, "Coronary artery stenoses: assessment with contrast-enhanced electron-beam CT and axial reconstructions," *Radiology,* vol. 208, no. 1, pp. 167-72, Jul, 1998.

[18] D. Baumgart, A. Schmermund, G. Goerge, M. Haude, J. Ge, M. Adamzik, C. Sehnert, K. Altmaier, D. Groenemeyer, and R. Seibel, "Comparison of electron beam computed tomography with intracoronary ultrasound and coronary angiography for detection of coronary atherosclerosis," *Journal of the american college of cardiology,* vol. 57, no. 14, pp. E1466-E1466, 2011.

[19] E. G. Dan, C. Y. Leung, T. Hiro, B. Maheswaran, and J. M. Tobis, "In vitro atherosclerotic plaque and calcium quantitation by intravascular ultrasound and electron-beam computed tomography," *American Heart Journal,* vol. 131, no. 5, pp. 899-906, 1996.

[20] J. Rodenwaldt, "Multislice computed tomography of the coronary arteries," *European Radiology,* vol. 13, no. 4, pp. 748-757, Apr, 2003.

[21] M. Bando, H. Yamada, K. Kusunose, D. Fukuda, R. Amano, R. Tamai, Y. Torii, Y. Hirata, S. Nishio, J. Satomi, S. Nagahiro, and M. Sata, "Noninvasive Quantitative Tissue Characterization of Carotid Plaques Using Color-Coded Mapping Based on Ultrasound Integrated Backscatter," *Jacc-Cardiovascular Imaging,* vol. 9, no. 5, pp. 625-627, May, 2016.

[22] E. B. Mathiesen, K. H. Bonaa, and O. Joakimsen, "Low levels of high-density lipoprotein cholesterol are associated with echolucent carotid artery plaques - The Tromso study," *Stroke,* vol. 32, no. 9, pp. 1960-1965, Sep, 2001.

[23] F. Molinari, G. Zeng, and J. S. Suri, "A state of the art review on intima-media thickness (IMT) measurement and wall segmentation techniques for carotid ultrasound," *Computer Methods And Programs In Biomedicine,* vol. 100, no. 3, pp. 201-221, Dec, 2010.

[24] I. Kupciunas, and A. Kopustinskas, "Ultrasonic Non-invasive Investigation of Arterial Elasticity." pp. 274-277.

[25] M. Couade, “The advent of ultrafast ultrasound in vascular imaging: a review,” *Journal of Vascular Diagnostics and Interventions*, 2016.

[26] K. AlMuhanna, M. M. Hossain, L. Zhao, J. Fischell, G. Kowalewski, M. Dux, S. Sikdar, and B. K. Lal, “Carotid plaque morphometric assessment with three-dimensional ultrasound imaging,” *Journal of Vascular Surgery,* vol. 61, no. 3, pp. 690-697, 2015.

[27] A. M. Johri, J. E. Herr, T. Y. Li, O. Yau, and V. Nambi, “Novel ultrasound methods to investigate carotid artery plaque vulnerability,” *Journal of the American Society of Echocardiography,* vol. 30, no. 2, pp. 139-148, 2017.

[28] M. Tertti, H. Paajanen, U. M. Kujala, A. Alanen, T. T. Salmi, and M. Kormano, “Disc degeneration in young gymnasts. A magnetic resonance imaging study,” *Am J Sports Med,* vol. 18, no. 2, pp. 206-8, Mar-Apr, 1990.

[29] L. W. Turnbull, “Magnetic-Resonance Angiography - Principles And Clinical-Applications,” *British Journal Of Hospital Medicine,* vol. 51, no. 4, pp. 154-&, Feb 16, 1994.

[30] H. Kobayashi, R. Nakayama, A. Hizukuri, M. Ishida, K. Kitagawa, and H. Sakuma, “Improving Image Resolution of Whole-Heart Coronary MRA Using Convolutional Neural Network,” *J Digit Imaging,* vol. 33, no. 2, pp. 497-503, Apr, 2020.

[31] K. D. Hagspiel, L. Flors, M. Hanley, and P. T. Norton, “Computed tomography angiography and magnetic resonance angiography imaging of the mesenteric vasculature,” *Tech Vasc Interv Radiol,* vol. 18, no. 1, pp. 2-13, Mar, 2015.

[32] M. P. Hartung, T. M. Grist, and C. J. Francois, “Magnetic resonance angiography: current status and future directions,” *Journal Of Cardiovascular Magnetic Resonance,* vol. 13, Mar 9, 2011.

[33] W. J. Rogers, J. W. Prichard, Y. L. Hu, P. R. Olson, D. H. Benckart, C. M. Kramer, D. A. Vido, and N. Reichek, “Characterization of signal properties in atherosclerotic plaque components by intravascular MRI,” *Arteriosclerosis Thrombosis And Vascular Biology,* vol. 20, no. 7, pp. 1824-1830, Jul, 2000.

[34] G. L. ten Kate, E. J. G. Sijbrands, R. Valkema, F. J. ten Cate, S. B. Feinstein, A. F. W. van der Steen, M. J. A. P. Daemen, and A. F. L. Schinkel, “Molecular imaging of inflammation and intraplaque vasa vasorum: A step forward to identification of vulnerable plaques?,” *Journal Of Nuclear Cardiology,* vol. 17, no. 5, pp. 897-912, Oct, 2010.

[35] E. Plenge, D. H. J. Poot, M. Bernsen, G. Kotek, G. Houston, P. Wielopolski, L. van der Weerd, W. J. Niessen, and E. Meijering, "Super-resolution methods in MRI: Can they improve the trade-off between resolution, signal-to-noise ratio, and acquisition time?," *Magnetic Resonance In Medicine,* vol. 68, no. 6, pp. 1983-1993, Nov, 2012.

[36] M. Weinreich, Y. Litwok, L. W. Mui, and J. F. Lau, "Advanced vascular imaging," *Vasc Med,* vol. 22, no. 1, pp. 73-76, Feb, 2017.

[37] M. F. Eleid, M. S. Tweet, P. M. Young, E. Williamson, S. N. Hayes, and R. Gulati, "Spontaneous coronary artery dissection: challenges of coronary computed tomography angiography," *European Heart Journal-Acute Cardiovascular Care,* vol. 7, no. 7, pp. 609-613, Oct, 2018.

[38] S. Cimen, A. Gooya, M. Grass, and A. F. Frangi, "Reconstruction of coronary arteries from X-ray angiography: A review," *Medical Image Analysis,* vol. 32, pp. 46-68, Aug, 2016.

[39] L. E. Mantella, K. Liblik, and A. M. Johri, "Vascular imaging of atherosclerosis: Strengths and weaknesses," *Atherosclerosis,* vol. 319, pp. 42-50, Feb, 2021.

[40] S. E. Nissen, "Limitations of Computed Tomography Coronary Angiography," *Journal Of the American College Of Cardiology,* vol. 52, no. 25, pp. 2145-2147, Dec 16, 2008.

[41] C. L. De Korte, and A. F. Van Der Steen, "Intravascular ultrasound elastography: an overview," *Ultrasonics,* vol. 40, no. 1-8, pp. 859-865, 2002.

[42] B. F. Waller, C. A. Pinkerton, and J. Slack, "Intravascular ultrasound: a histological study of vessels during life. The new'gold standard'for vascular imaging," *Circulation,* vol. 85, no. 6, pp. 2305-2310, 1992.

[43] J. M. de la Torre Hernandez, J. A. Baz Alonso, J. A. Gómez Hospital, F. Alfonso Manterola, T. Garcia Camarero, F. Gimeno de Carlos, G. Roura Ferrer, A. Sanchez Recalde, Í. L. Martínez-Luengas, and J. Gomez Lara, "Clinical impact of intravascular ultrasound guidance in drug-eluting stent implantation for unprotected left main coronary disease: pooled analysis at the patient-level of 4 registries," *JACC: Cardiovascular Interventions,* vol. 7, no. 3, pp. 244-254, 2014.

[44] P. Lermusiaux, R. Martinez, A. Donadey, F. Bleuet, and L. Castellani, "Intravascular ultrasound: limitation and prospects," *Journal des maladies vasculaires,* vol. 25, no. 4, pp. 229-236, 2000.

[45] A. F. Fercher, W. Drexler, C. K. Hitzenberger, and T. Lasser, "Optical coherence tomography-principles and applications," *Reports on progress in physics,* vol. 66, no. 2, pp. 239, 2003.

[46] H. M. Rahim, E. Shlofmitz, A. Gore, E. Hakemi, G. S. Mintz, A. Maehara, A. Jeremias, O. Ben-Yehuda, G. W. Stone, and R. A. Shlofmitz, "Ivus-versus oct-guided coronary stent implantation: a comparison of intravascular imaging for stent optimization," *Current Cardiovascular Imaging Reports,* vol. 11, pp. 1-15, 2018.

[47] M. E. Brezinski, G. J. Tearney, B. E. Bouma, J. A. Izatt, M. R. Hee, E. A. Swanson, J. F. Southern, and J. G. Fujimoto, "Optical coherence tomography for optical biopsy: properties and demonstration of vascular pathology," *Circulation,* vol. 93, no. 6, pp. 1206-1213, 1996.

[48] N. A. Patel, D. L. Stamper, and M. E. Brezinski, "Review of the ability of optical coherence tomography to characterize plaque, including a comparison with intravascular ultrasound," *Cardiovascular And Interventional Radiology,* vol. 28, no. 1, pp. 1-9, Jan-Feb, 2005.

[49] C. Peng, H. Y. Wu, S. Kim, X. M. Dai, and X. N. Jiang, "Recent Advances in Transducers for Intravascular Ultrasound (IVUS) Imaging," *Sensors,* vol. 21, no. 10, May, 2021.

[50] Y. Seki, Y. Sakaguchi, and A. Iguchi, "A State-of-the-Art Intravascular Ultrasound Diagnostic System," *Intravascular Ultrasound*, pp. 97-109: Elsevier, 2020.

[51] M. C. McDaniel, P. Eshtehardi, F. J. Sawaya, J. S. Douglas, and H. Samady, "Contemporary Clinical Applications of Coronary Intravascular Ultrasound," *Jacc-Cardiovascular Interventions,* vol. 4, no. 11, pp. 1155-1167, Nov, 2011.

[52] J.-H. Sung, and J.-H. Chang, "Mechanically rotating intravascular ultrasound (IVUS) transducer: A review," *Sensors,* vol. 21, no. 11, pp. 3907, 2021.

[53] T.-G. Kwon, Y. J. Cho, and J.-H. Bae, "Physical principles and equipment: IVUS," *Coronary Imaging and Physiology*, pp. 3-7, 2018.

[54] S. Bangalore, and D. L. Bhatt, "Coronary Intravascular Ultrasound," *Circulation,* vol. 127, no. 25, pp. E868-E874, Jun 25, 2013.

[55] F. S. Foster, L. K. Ryan, and D. H. Turnbull, "Characterization of lead zirconate titanate ceramics for use in miniature high-frequency (20-80 MHz) transducers," *IEEE transactions on ultrasonics, ferroelectrics, and frequency control,* vol. 38, no. 5, pp. 446-453, 1991.

[56] A. Ng, and J. Swanevelder, "Resolution in ultrasound imaging," *Continuing Education in Anaesthesia Critical Care & Pain,* vol. 11, no. 5, pp. 186-192, 2011.

[57] F. S. Foster, C. J. Pavlin, K. A. Harasiewicz, D. A. Christopher, and D. H. Turnbull, "Advances in ultrasound biomicroscopy," *Ultrasound in medicine & biology,* vol. 26, no. 1, pp. 1-27, 2000.

[58] A. Agarwal, F. K. Schneider, Y. M. Yoo, and Y. Kim, “Image quality evaluation with a new phase rotation beamformer,” *IEEE transactions on ultrasonics, ferroelectrics, and frequency control,* vol. 55, no. 9, pp. 1947-1955, 2008.

[59] W. Qiu, Y. Yu, F. K. Tsang, H. Zheng, and L. Sun, “A novel modulated excitation imaging system for microultrasound,” *IEEE transactions on biomedical engineering,* vol. 60, no. 7, pp. 1884-1890, 2013.

[60] T. Misaridis, and J. A. Jensen, “Use of modulated excitation signals in medical ultrasound. Part I: Basic concepts and expected benefits,” *IEEE transactions on ultrasonics, ferroelectrics, and frequency control,* vol. 52, no. 2, pp. 177-191, 2005.

[61] M. O'Donnell, “Coded excitation system for improving the penetration of real-time phased-array imaging systems,” *IEEE transactions on ultrasonics, ferroelectrics, and frequency control,* vol. 39, no. 3, pp. 341-351, 1992.

[62] N. Wang, C. Yang, J. Xu, W. Shi, W. Huang, Y. Cui, and X. Jian, “An improved chirp coded excitation based on compression pulse weighting method in endoscopic ultrasound imaging,” *IEEE transactions on ultrasonics, ferroelectrics, and frequency control,* vol. 68, no. 3, pp. 446-452, 2020.

[63] H. M. Garcìa-Garcìa, B. D. Gogas, P. W. Serruys, and N. Bruining, “IVUS-based imaging modalities for tissue characterization: similarities and differences,” *The international journal of cardiovascular imaging,* vol. 27, pp. 215-224, 2011.

[64] J. Gao, Y.-Y. Wang, and Y. Liu, “Application of virtual histological intravascular ultrasound in plaque composition assessment of saphenous vein graft diseases,” *Chinese Medical Journal,* vol. 132, no. 08, pp. 957-962, 2019.

[65] A. Nair, B. D. Kuban, E. M. Tuzcu, P. Schoenhagen, S. E. Nissen, and D. G. Vince, “Coronary plaque classification with intravascular ultrasound radiofrequency data analysis,” *Circulation,* vol. 106, no. 17, pp. 2200-2206, 2002.

[66] S. Sathyanarayana, S. Carlier, W. Li, and L. Thomas, “Characterisation of atherosclerotic plaque by spectral similarity of radiofrequency intravascular ultrasound signals,” *EuroIntervention,* vol. 5, no. 1, pp. 133-139, 2009.

[67] M. Okubo, M. Kawasaki, Y. Ishihara, U. Takeyama, T. Kubota, T. Yamaki, S. Ojio, K. Nishigaki, G. Takemura, and M. Saio, “Development of integrated backscatter intravascular ultrasound for tissue characterization of coronary plaques,” *Ultrasound in medicine & biology,* vol. 34, no. 4, pp. 655-663, 2008.

[68] N. Bruining, S. Verheye, M. Knaapen, P. Somers, J. R. Roelandt, E. Regar, I. Heller, S. de Winter, J. Ligthart, and G. Van Langenhove, “Three‐dimensional and quantitative analysis of atherosclerotic plaque composition by automated differential echogenicity,” *Catheterization and Cardiovascular Interventions,* vol. 70, no. 7, pp. 968-978, 2007.

[69] J. Yuan, S. Rhee, and X. N. Jiang, "60 MHz PMN-PT based 1-3 composite transducer for IVUS imaging." pp. 682-685.

[70] X. Li, T. Ma, J. Tian, P. Han, Q. Zhou, and K. K. Shung, “Micromachined PIN-PMN-PT crystal composite transducer for high-frequency intravascular ultrasound (IVUS) imaging,” *IEEE transactions on ultrasonics, ferroelectrics, and frequency control,* vol. 61, no. 7, pp. 1171-1178, 2014.

[71] X. Li, W. Wu, Y. Chung, W. Y. Shih, W.-H. Shih, Q. Zhou, and K. K. Shung, “80-MHz intravascular ultrasound transducer using PMN-PT free-standing film,” *IEEE transactions on ultrasonics, ferroelectrics, and frequency control,* vol. 58, no. 11, pp. 2281-2288, 2011.

[72] T. Ma, M. Yu, J. Li, C. E. Munding, Z. Chen, C. Fei, K. K. Shung, and Q. Zhou, “Multi-frequency intravascular ultrasound (IVUS) imaging,” *IEEE transactions on ultrasonics, ferroelectrics, and frequency control,* vol. 62, no. 1, pp. 97-107, Jan, 2015.

[73] C. E. Munding, E. Cherin, I. Jourard, J. J. Weyers, D. E. Goertz, B. K. Courtney, and F. S. Foster, “Development of a 3 French Dual-Frequency Intravascular Ultrasound Catheter,” *Ultrasound Med Biol,* vol. 44, no. 1, pp. 251-266, Jan, 2018.

[74] C. E. Munding, E. Cherin, N. Alves, D. E. Goertz, B. K. Courtney, and F. S. Foster, “30/80 Mhz Bidirectional Dual -Frequency Ivus Feasibility Evaluated In Vivo And for Stent Imaging,” *Ultrasound In Medicine And Biology,* vol. 46, no. 8, pp. 2104-2112, Aug, 2020.

[75] M. Su, Z. Zhang, J. Hong, Y. Huang, P. Mu, Y. Yu, R. Liu, S. Liang, H. Zheng, and W. Qiu, “Cable shared dual-frequency catheter for intravascular ultrasound,” *IEEE transactions on ultrasonics, ferroelectrics, and frequency control,* vol. 66, no. 5, pp. 849-856, Feb 11, 2019.

[76] M. C. Hemmsen, J. H. Rasmussen, and J. A. Jensen, “Tissue harmonic synthetic aperture ultrasound imaging,” *J Acoust Soc Am,* vol. 136, no. 4, pp. 2050-6, Oct, 2014.

[77] A. Anvari, F. Forsberg, and A. E. Samir, “A Primer on the Physical Principles of Tissue Harmonic Imaging,” *Radiographics,* vol. 35, no. 7, pp. 1955-64, Nov-Dec, 2015.

[78] J. Ma, K. H. Martin, P. A. Dayton, and X. Jiang, “A preliminary engineering design of intravascular dual-frequency transducers for contrast-enhanced acoustic angiography and

molecular imaging," *IEEE transactions on ultrasonics, ferroelectrics, and frequency control,* vol. 61, no. 5, pp. 870-880, 2014.

[79] J. Lee, E. J. Shin, C. Lee, and J. H. Chang, "Development of Dual-Frequency Oblong-Shaped-Focused Transducers for Intravascular Ultrasound Tissue Harmonic Imaging," *IEEE transactions on ultrasonics ferroelectrics and frequency control,* vol. 65, no. 9, pp. 1571-1582, Sep, 2018.

[80] J. Lee, J. Y. Moon, and J. H. Chang, "A 35 MHz/105 MHz Dual-Element Focused Transducer for Intravascular Ultrasound Tissue Imaging Using the Third Harmonic," *Sensors,* vol. 18, no. 7, Jul, 2018.

[81] J. Lee, and J. H. Chang, "Dual-Element Intravascular Ultrasound Transducer for Tissue Harmonic Imaging and Frequency Compounding: Development and Imaging Performance Assessment," *IEEE Transactions on Biomedical Engineering,* vol. 66, no. 11, pp. 3146-3155, Nov, 2019.

[82] Y. Chen, W. Qiu, K. H. Lam, B. Liu, X. Jiang, H. Zheng, H. Luo, H. Chan, and J. Dai, "Focused intravascular ultrasonic probe using dimpled transducer elements," *Ultrasonics,* vol. 56, pp. 227-231, 2015.

[83] S. Yoon, J. Williams, B. J. Kang, C. Yoon, N. Cabrera-Munoz, J. S. Jeong, S. G. Lee, K. K. Shung, and H. H. Kim, "Angled-focused 45 MHz PMN-PT single element transducer for intravascular ultrasound imaging," *Sensors and Actuators A: Physical,* vol. 228, pp. 16-22, 2015.

[84] X. Jian, Z. Han, P. Liu, J. Xu, Z. Li, P. Li, W. Shao, and Y. Cui, "A high frequency geometric focusing transducer based on 1-3 piezocomposite for intravascular ultrasound imaging," *BioMed research international,* vol. 2017, 2017.

[85] J. Lee, J. Jang, and J. H. Chang, "Oblong-shaped-focused transducers for intravascular ultrasound imaging," *IEEE Transactions on Biomedical Engineering,* vol. 64, no. 3, pp. 671-680, 2016.

[86] C. Fei, Y. Yang, F. Guo, P. Lin, Q. Chen, Q. Zhou, and L. Sun, "PMN-PT single crystal ultrasonic transducer with half-concave geometric design for IVUS imaging," *IEEE Transactions on Biomedical Engineering,* vol. 65, no. 9, pp. 2087-2092, 2017.

[87] M. J. Suter, S. K. Nadkarni, G. Weisz, A. Tanaka, F. A. Jaffer, B. E. Bouma, and G. J. Tearney, "Intravascular optical imaging technology for investigating the coronary artery," *JACC Cardiovasc Imaging,* vol. 4, no. 9, pp. 1022-39, Sep, 2011.

[88] X. A. Li, J. C. Yin, C. H. Hu, Q. F. Zhou, K. K. Shung, and Z. P. Chen, "High-resolution coregistered intravascular imaging with integrated ultrasound and optical coherence tomography probe," *Applied Physics Letters,* vol. 97, no. 13, Sep 27, 2010.

[89] J. Li, X. Li, D. Mohar, A. Raney, J. Jing, J. Zhang, A. Johnston, S. Liang, T. Ma, K. K. Shung, S. Mahon, M. Brenner, J. Narula, Q. Zhou, P. M. Patel, and Z. Chen, "Integrated IVUS-OCT for real-time imaging of coronary atherosclerosis," *JACC Cardiovasc Imaging,* vol. 7, no. 1, pp. 101-3, Jan, 2014.

[90] J. W. Li, T. Ma, D. Mohar, E. Steward, M. Y. Yu, Z. L. Piao, Y. M. He, K. K. Shung, Q. F. Zhou, P. M. Patel, and Z. P. Chen, "Ultrafast optical-ultrasonic system and miniaturized catheter for imaging and characterizing atherosclerotic plaques in vivo," *Scientific Reports,* vol. 5, Dec 18, 2015.

[91] B. Wang, J. L. Su, J. Amirian, S. H. Litovsky, R. Smalling, and S. Emelianov, "Detection of lipid in atherosclerotic vessels using ultrasound-guided spectroscopic intravascular photoacoustic imaging," *Optics Express,* vol. 18, no. 5, pp. 4889-4897, Mar 1, 2010.

[92] Y. Matsuzawa, S. Sugiyama, E. Akiyama, S. Umemura, K. Kimura, and H. Ogawa, "Incremental Significance Of Endothelial Function Assessed by Reactive Hyperemia Peripheral Arterial Tonometry for Predicting Cardiovascular Events In Stable Patients with Coronary Artery Disease," *Journal Of the American College Of Cardiology,* vol. 59, no. 13, pp. E1493-E1493, Mar 27, 2012.

[93] J. Hong, M. Su, Y. Yu, Z. Zhang, R. Liu, Y. Haung, P. Mu, H. Zheng, and W. Qiu, "A Dual-Mode Imaging Catheter for Intravascular Ultrasound Application," *IEEE Transactions on Medical Imaging,* vol. 38, no. 3, pp. 657-663, Mar, 2019.

[94] F. S. Foster, C. J. Pavlin, K. A. Harasiewicz, D. A. Christopher, and D. H. Turnbull, "Advances in ultrasound biomicroscopy," *Ultrasound In Medicine And Biology,* vol. 26, no. 1, pp. 1-27, Jan, 2000.

[95] J. Lee, J. Jang, and J. H. Chang, "Oblong-Shaped-Focused Transducers for Intravascular Ultrasound Imaging," *IEEE Transactions on Biomedical Engineering,* vol. 64, no. 3, pp. 671-680, Mar, 2017.

[96] J. Chen, J. Xiao, D. Lisevych, A. Shakouri, and Z. Fan, "Deep-subwavelength control of acoustic waves in an ultra-compact metasurface lens," *Nature Communications,* vol. 9, Nov 22, 2018.

[97] Y. X. Shen, Y. G. Peng, F. Y. Cai, K. Huang, D. G. Zhao, C. W. Qiu, H. R. Zheng, and X. F. Zhu,

"Ultrasonic super-oscillation wave-packets with an acoustic meta-lens," *Nature Communications,* vol. 10, Jul 30, 2019.

[98] X. X. Xia, Y. C. Li, F. Y. Cai, H. Zhou, T. Ma, and H. R. Zheng, "Ultrasonic tunable focusing by a stretchable phase-reversal Fresnel zone plate," *Applied Physics Letters,* vol. 117, no. 2, Jul 13, 2020.

[99] D. Tarrazo-Serrano, S. Perez-Lopez, P. Candelas, A. Uris, and C. Rubio, "Acoustic Focusing Enhancement In Fresnel Zone Plate Lenses," *Scientific Reports,* vol. 9, May 8, 2019.

[100] D. C. Calvo, A. L. Thangawng, M. Nicholas, and C. N. Layman, "Thin Fresnel zone plate lenses for focusing underwater sound," *Applied Physics Letters,* vol. 107, no. 1, Jul 6, 2015.

[101] J. T. Welter, S. Sathish, J. M. Dierken, P. G. Brodrick, M. R. Cherry, and J. D. Heebl, "Broadband aperiodic air coupled ultrasonic lens," *Applied Physics Letters,* vol. 100, no. 21, pp. 214102, 2012.

[102] M. Molerón, M. Serra-Garcia, and C. Daraio, "Acoustic Fresnel lenses with extraordinary transmission," *Applied Physics Letters,* vol. 105, no. 11, pp. 114109, 2014.

[103] R. Lirette, J. Mobley, and L. Zhang, "Ultrasonic extraction and manipulation of droplets from a liquid-liquid interface with near-field acoustic tweezers," *Physical Review Applied,* vol. 12, no. 6, pp. 061001, 2019.

[104] B. Hadimioglu, E. Rawson, R. Lujan, M. Lim, J. Zesch, B. Khuri-Yakub, and C. Quate, "High-efficiency Fresnel acoustic lenses." pp. 579-582.

[105] W. B. Qiu, X. Y. Wang, Y. Chen, Q. Fu, M. Su, L. N. Zhang, J. J. Xia, J. Y. Dai, Y. N. Zhang, and H. R. Zheng, "Modulated Excitation Imaging System for Intravascular Ultrasound," *IEEE Transactions on Biomedical Engineering,* vol. 64, no. 8, pp. 1935-1942, Aug, 2017.

[106] C. Costopoulos, A. J. Brown, Z. Teng, S. P. Hoole, N. E. West, H. Samady, and M. R. Bennett, "Intravascular ultrasound and optical coherence tomography imaging of coronary atherosclerosis," *The International Journal of Cardiovascular Imaging,* vol. 32, pp. 189-200, 2016.

[107] N. W. Shammas, Q. Radaideh, W. J. Shammas, G. E. Daher, R. J. Rachwan, and Y. Radaideh, "The role of precise imaging with intravascular ultrasound in coronary and peripheral interventions," *Vasc Health Risk Manag,* vol. 15, pp. 283-290, 2019.

[108] C. di Mario, K. C. Koskinas, and L. Raber, "Clinical Benefit of IVUS Guidance for Coronary

Stenting The ULTIMATE Step Toward Definitive Evidence?," *Journal Of the American College Of Cardiology,* vol. 72, no. 24, pp. 3138-3141, Dec 18, 2018.

[109] J. W. Choe, Ö. Oralkan, and P. T. Khuri-Yakub, "Design optimization for a 2-D sparse transducer array for 3-D ultrasound imaging." pp. 1928-1931.

[110] S. Blaak, Z. Yu, G. Meijer, C. Prins, C. Lancee, J. Bosch, and N. de Jong, "Design of a micro-beamformer for a 2D piezoelectric ultrasound transducer." pp. 1338-1341.

[111] X. Huang, M. A. L. Bell, and K. Ding, "Deep learning for ultrasound beamforming in flexible array transducer," *IEEE transactions on medical imaging,* vol. 40, no. 11, pp. 3178-3189, 2021.

[112] S. Yang, J. Li, Y. Liu, M. Wang, L. Qiao, X. Gao, Y. Chang, H. Du, Z. Xu, and S. Zhang, "Textured ferroelectric ceramics with high electromechanical coupling factors over a broad temperature range," *Nature Communications,* vol. 12, no. 1, pp. 1414, 2021.

[113] A. I. S. 176-, "IEEE standard on piezoelectricity."

[114] J. M. Cannata, T. A. Ritter, W.-H. Chen, R. H. Silverman, and K. K. Shung, "Design of efficient, broadband single-element (20-80 MHz) ultrasonic transducers for medical imaging applications," *IEEE transactions on ultrasonics, ferroelectrics, and frequency control,* vol. 50, no. 11, pp. 1548-1557, 2003.

[115] A. Safari, and E. K. Akdogan, *Piezoelectric and acoustic materials for transducer applications*: Springer Science & Business Media, 2008.

[116] Q. Zhou, K. H. Lam, H. Zheng, W. Qiu, and K. K. Shung, "Piezoelectric single crystal ultrasonic transducers for biomedical applications," *Progress in materials science,* vol. 66, pp. 87-111, 2014.

[117] F. Li, D. Lin, Z. Chen, Z. Cheng, J. Wang, C. Li, Z. Xu, Q. Huang, X. Liao, and L.-Q. Chen, "Ultrahigh piezoelectricity in ferroelectric ceramics by design," *Nature materials,* vol. 17, no. 4, pp. 349-354, 2018.

[118] S. Z. Liang, M. Su, B. Q. Liu, R. Liu, H. R. Zheng, W. B. Qiu, and Z. Q. Zhang, "Evaluation of Blood Induced Influence for High-Definition Intravascular Ultrasound (HD-IVUS)," *IEEE transactions on ultrasonics ferroelectrics and frequency control,* vol. 69, no. 1, pp. 98-105, Jan, 2022.

[119] V. T. Rathod, "A review of electric impedance matching techniques for piezoelectric sensors, actuators and transducers," *Electronics,* vol. 8, no. 2, pp. 169, 2019.

[120] F. Deleaval, A. Bouvier, G. Finet, G. Cloutier, S. K. Yazdani, S. Le Floc'h, P. Clarysse, R. I. Pettigrew, and J. Ohayon, "The Intravascular Ultrasound Elasticity-Palpography Technique Revisited: A Reliable Tool for the In Vivo Detection of Vulnerable Coronary Atherosclerotic Plaques (vol 39, pg 1469, 2013)," *Ultrasound In Medicine And Biology,* vol. 40, no. 5, pp. 1034-1034, May, 2014.

[121] T.-J. Teo, "Intravascular ultrasound (IVUS)—Technologies and applications." pp. 760-769.

[122] H.-B. Park, Y.-H. Cho, and D.-K. Cho, "Ivus artifacts and image control," *Coronary Imaging and Physiology*, pp. 9-17, 2018.

[123] C.-P. Lin, J. Honye, C.-J. Chang, and C.-T. Kuo, "Clinical application of intravascular ultrasound in coronary artery disease: an update," *Acta Cardiol. Sin,* vol. 27, pp. 1-13, 2011.

[124] S. Hou, Y. Li, C. Zou, Y. Li, H. Tang, Z. Liu, S. Chen, and J. Peng, "A Novel Distal Micromotor-Based Side-Looking Intravascular Ultrasound Transducer," *IEEE transactions on ultrasonics, ferroelectrics, and frequency control,* vol. 69, no. 1, pp. 283-290, 2021.

[125] Y. Kawase, Y. Suzuki, F. Ikeno, R. Yoneyama, K. Hoshino, H. Q. Ly, G. T. Lau, M. Hayase, A. C. Yeung, and R. J. Hajjar, "Comparison of nonuniform rotational distortion between mechanical IVUS and OCT using a phantom model," *Ultrasound in medicine & biology,* vol. 33, no. 1, pp. 67-73, 2007.

[126] B. J. Kimura, V. Bhargava, W. Palinski, R. J. Russo, and A. N. DeMaria, "Distortion of intravascular ultrasound images because of nonuniform angular velocity of mechanical-type transducers," *American heart journal,* vol. 132, no. 2, pp. 328-336, 1996.

[127] P. P. Kearney, M. P. Ramo, T. Spencer, T. Shaw, I. R. Starkey, N. McDicken, and G. R. Sutherland, "A study of the quantitative and qualitative impact of catheter shaft angulation in a mechanical intravascular ultrasound system," *Ultrasound in medicine & biology,* vol. 23, no. 1, pp. 87-93, 1997.

[128] C. Gatta, O. Pujol, O. R. Leor, J. M. Ferre, and P. Radeva, "Fast rigid registration of vascular structures in IVUS sequences," *IEEE Transactions on Information Technology in Biomedicine,* vol. 13, no. 6, pp. 1006-1011, 2009.

[129] S. Sathyanarayana, "Nonuniform rotational distortion (NURD) reduction," Google Patents, 2006.

[130] N. Uribe-Patarroyo, and B. E. Bouma, "Rotational distortion correction in endoscopic optical coherence tomography based on speckle decorrelation," *Optics letters,* vol. 40, no. 23, pp.

5518-5521, 2015.

[131] O. O. Ahsen, H.-C. Lee, M. G. Giacomelli, Z. Wang, K. Liang, T.-H. Tsai, B. Potsaid, H. Mashimo, and J. G. Fujimoto, "Correction of rotational distortion for catheter-based en face OCT and OCT angiography," *Optics letters,* vol. 39, no. 20, pp. 5973-5976, 2014.

[132] M. S. M. Salimuzzaman, A. M. A. Matani, O. O. O. Oshiro, K. C. K. Chihara, and M. A. M. Asao, "Blood vessel visualization using a micromotor type intravascular ultrasound endoscope," *Japanese journal of applied physics,* vol. 36, no. 5S, pp. 3250, 1997.

[133] T. Wang, C. Lancée, R. Beurskens, J. Meijer, B. Knapen, A. F. van der Steen, and G. van Soest, "Development of a high-speed synchronous micro motor and its application in intravascular imaging," *Sensors and Actuators A: Physical,* vol. 218, pp. 60-68, 2014.

[134] J. Peng, L. Ma, X. Li, H. Tang, Y. Li, and S. Chen, "A novel synchronous micro motor for intravascular ultrasound imaging," *IEEE Transactions on Biomedical Engineering,* vol. 66, no. 3, pp. 802-809, 2018.

[135] B. Wang, Y. Wang, L. He, T. Cao, Z. Wen, X. Li, and D. Wu, "Intravascular Ultrasound (IVUS) Imaging Using a Distal Rotary Ultrasonic Micro-motor." pp. 1-3.

[136] P. Herz, Y. Chen, A. Aguirre, K. Schneider, P. Hsiung, J. Fujimoto, K. Madden, J. Schmitt, J. Goodnow, and C. Petersen, "Micromotor endoscope catheter for in vivo, ultrahigh-resolution optical coherence tomography," *Optics letters,* vol. 29, no. 19, pp. 2261-2263, 2004.

[137] W. Qiu, Y. Chen, C. M. Wong, B. Liu, J. Dai, and H. Zheng, "A novel dual-frequency imaging method for intravascular ultrasound applications," *Ultrasonics,* vol. 57, pp. 31-5, Mar, 2015.

[138] S. Yoon, M. G. Kim, J. A. Williams, C. Yoon, B. J. Kang, N. Cabrera-Munoz, K. K. Shung, and H. H. Kim, "Dual-element needle transducer for intravascular ultrasound imaging," *Journal of medical imaging,* vol. 2, no. 2, pp. 027001-027001, 2015.

[139] C.-C. Huang, "High-frequency attenuation and backscatter measurements of rat blood between 30 and 60 MHz," *Physics in Medicine & Biology,* vol. 55, no. 19, pp. 5801, 2010.

[140] K. K. Shung, *Diagnostic ultrasound: Imaging and blood flow measurements*: CRC press, 2015.